Winds in Active Galactic Nucleii

Mark D. O'Reilly

A Thesis Submitted for the Degree of
Ph.D. in Astronomy
University of Leicester

27th October 1995

ProQuest LLC
789 East Eisenhower Parkway
P.O. Box 1346
Ann Arbor, MI 48106-1346

Acknowledgements

I would like to thank my postgraduate supervisor, Dr. Derek Raine, for all his help during my research. I would also like to thank the staff and students of the Astronomy Group at Leicester University. Finally, my thanks go to Sue, without whose support I would never have completed this thesis.

The research that lead to this thesis was supported by an S.E.R.C. Research Studentship.

Abstract

This thesis is concerned with a number of problems relating to mass outflow in active galactic nucleii. A number of authors have discussed radiation pressure driven winds, and some have discussed the spectral evolution in such a wind, but under restricted conditions, e.g. the radiation spectrum is thermal at high frequencies. A number of authors have discussed the Comptonization of an arbitrary input spectrum in a stationary medium. In Chapter 2, I consider the evolution of an arbitrary input spectrum by a supercritical outflow. I consider outflows that contain a number of $e^{\pm}$ pairs, these flows are supercritical for modest mass outflows. I find that the input spectrum is not significantly distorted, but that the high frequency cut off moves to a lower frequency. There is a major flaw in the model: most of the radiation energy is carried by photons of energy larger than 0.5 MeV; however, the Kompaneets equation, which is central to the model, is not valid for photons of this energy. There is also an indication that pair production is an important process in the inner regions of the system, a process which has been ignored.

The second problem is concerned with the broad line region. The 'standard model' requires a two-phase equilibrium between a hot intercloud medium and cool clouds. This is incompatible with the radiative heating implied by observed spectra. In Chapter 3, I introduce generallised two body heating into the intercloud wind. I find that both the dynamics and thermal equilibria of the system are compatible with the observed velocities of broad line clouds confined by an outflowing medium at 10^9 K.

Many BLR theories require the presence of a wind, probably created in the nuclear region. Variability observations suggest that the X-ray spectrum is also created in this region, this spectrum is often described as a universal power law. It is unreasonable to assume that this ubiquitous slope can be produced by arbitrary tuning of the input parameters. In Chapter 4, I describe a model where the wind dynamics and spectral slope are related: the disk atmosphere is heated by UV radiation and by injected $e^{\pm}$ pairs, causing it to form a wind. The mass loss limits the optical depth of the atmosphere and hence the evolution of the X-ray spectrum, so that the system is tuned by the dynamics to produce the canonical power law. Unfortunately, some of the approximations used in the model produce a set of equations that severely limit the range of physical parameter space that may be sensibly investigated, one or more of these approximations must be relaxed for the model to be of greater use.

Chapter 1

Introduction

In this thesis I am concerned with a number of problems relating to mass outflows in active galactic nuclei.

In recent years, much work has concentrated on the production of radiatively driven winds in active galaxies. Arguments have been given in several cases (Drew and Boksenberg, 1984, Krolik *et al.*, 1984, Perry and Dyson, 1985) that active galaxies contain winds with high mass fluxes. A number of authors have discussed the generation of such winds by radiation pressure (e.g. Meier, 1982a, b and c). Some have discussed the processing of the input radiation spectrum by such a wind (e.g. Becker and Begelman, 1986a), albeit for a limited range of initial conditions, though a number of authors have investigated Comptonisation of an arbitrary input spectrum in a stationary medium (Katz, 1976, Ross, 1979, Sunyaev and Titarchuk, 1980, Guilbert, 1981). In addition, many authors have discussed the affects of the presence of electron-positron pairs in a stationary medium, e.g. the $e^{\pm}$-cauldron (Bonometto and Rees, 1971, Guilbert *et al.*, 1983).

The particular problems addressed here have a rather different motivation. In Chapter 2, I am concerned with the spectral distortion that might be introduced by Compton interactions in a wind. This differs from previous work in that the radiation is not assumed to originate solely from the outflowing material, but is injected by some unspecified process at small radii (in contrast to Becker and Begelman (1986a)). This would be relevant to, for example, an electron-positron cauldron model for the source spectrum produced at small radii (Guilbert *et al.*, 1983). Such models, treated with dynamical consistency, would be expected to lead to large mass outflows in the absence of a confining structure since the energy densities in the large

optical depth material of the source are necessarily large compared with the gravitational potential energy density. Another example is a synchrotron origin for the radiation in an electron-positron plasma. Such a plasma avoids the problem of Faraday rotation that would be associated with a cool proton component. These models are only self-consistent if the spectrum is not distorted in the outflow. Alternatively, a different parameter range may be appropriate in the model to match the observed spectra.

I shall consider outflows which contain a significant component of electron-positron pairs. These flows will be supercritical for modest mass outflow rates. I find that, for hard X-ray spectra with photon number index less than 1 and cut off at high energy, the initial spectrum is not distorted by Comptonisation in the moving atmosphere, except that the cut-off moves to lower frequency. Thus, an overproduction of γ- ray photons in the bare source need not be a problem for models of the nuclear energy generation.

The second problem concerns outflow in the broad line region. In the standard model (Krolik, McKee and Tarter, 1981) the BLR clouds result from a two phase equilibrium confined by the pressure of the hot phase. There are several well known problems (Frank, King and Raine, 1992). The radiation spectrum from the central source does not give rise to a two phase equilibrium at the pressure required for equilibrium with the BLR clouds ($nT \sim 10^{14}$) assuming the clouds are at distances from the source given by the ionisation parameter deduced from line ratios. The BLR clouds are supersonic at the Compton temperature of the radiation and hence unstable to outflow through the flanks. Now, it is possible that we do not see the same radiation spectrum as the clouds if the cloud distribution is non-spherical. It is also clear that the distances deduced from the ionisation parameters are too large in comparison with the size of the BLR region obtained from variability arguments. (Essentially time lags between the observed continuum and line variations.) But changes to the standard model along these lines cannot overcome all of the objections listed here. The simplest change would be an extra component of heating in the BLR such that the two phase equilibrim is restored and the equilibrium temperature of the hot phase is raised so that the X-ray absorption is negligible and the cloud motion is subsonic (Mathews and Ferland, 1987). It is easy to add ad hoc heating terms to achieve this. The problem is that the inter-cloud medium is not then gravitationally bound.

In Chapter 3, I go one step further. I add a general two-body heating term such as might be expected from cosmic rays. I show that a consistent dynamical picture can be achieved of a hot outflowing wind in two phase equilibrium with cool clouds. The line ratios from these

clouds, despite the extra heating, are not significantly different from the standard model (i.e. the extra heating has only a marginal effect on the cloud temperature.)

Many theories of the BLR (e.g. Dyson and Perry, 1987, Smith and Raine, 1988, Cassidy and Raine, 1993) have as an essential ingredient a wind. This outflow is assumed to arise in the nuclear region. Also arising in this region is the X-ray spectrum. This spectrum is often described as a universal power law with slope 0.7 for radio loud sources (Turner and Pounds, 1989); for radio quiet sources a slope nearer 0.9 is a better description (Shastri *et al.*, 1993). While there is a non-negligible spread in the spectral shape, it is clear that something like this power law is a reasonable first approximation to a universal spectrum. It is unreasonable to ascribe this spectrum to a picture that requires arbitrary tuning of parameters to produce the required slope.

In Chapter 4, I investigate a model in which these two aspects of active nuclei are related. The tuning of the spectrum is supposed to be derived from the dynamics. I make a first attempt to describe a new picture for the nuclear engine which gives the radiation spectrum and is dynamically consistent. I envisage a disk which consists of an optically thick cool 'filling' between a top and bottom layer of hot atmosphere. The cool layer radiates UV into the atmosphere where it is Compton scattered to give the X-ray spectrum. Thus accretion energy is extracted from the atmosphere by Compton scattering of injected photons rather than by its own radiation. (This is in contrast to Hardt and Maraschi, 1993.) I do not consider here the mechanism by which energy is deposited in the atmosphere except that it is supposed to lead to an electron-positron component. The source is therefore Eddington limited even at rather modest luminosity and mass is expected to be lost from the disk surface. The idea is that mass loss should limit the optical depth in the atmosphere and hence the Comptonisation of the spectrum, i.e. the system is automatically tuned by the dynamics to yield the observed ubiquitous power law in X-rays. The results, for a highly simplified representation of the physics (essentially a spatially averaged column instead of a disc atmosphere), suggest it might be possible to obtain the observed spectrum and mass outflow in this way but it is not a source of (chaotic) oscillitory behaviour.

Chapter 2

Spectral Evolution in a Supercritical $e^{\pm}$-Pair Wind

2.1 Introduction

In a supercritical plasma outflow radiation may be trapped by electron scattering. If the repeated Compton shifts in frequency are significant such a system might be expected to impress characteristic spectral features on the radiation spectrum. Arguments have been advanced in several cases (Drew and Boksenberg, 1984, Krolik *et al.*, 1985, Perry and Dyson, 1985) that active galaxies contain winds with high mass fluxes. If such winds contain electron-positron pairs (Lightman 1982) then even modest mass outflow rates will correspond to supercriticality. The generation of these winds by radiation pressure has been discussed by a number of authors (e.g. Meier, 1982a, b and c) with a view to determining a relation between mass flux and observed luminosity at infinity. Becker and Begelman (1986a) drew attention to the need to consider self-consistent spectra in supercritical winds but only for a restricted range of initial conditions such that the radiation spectrum is thermal at high frequencies. Many authors have, of course, discussed Comptonization of an arbitrary input spectrum in the case that the radiation has no dynamical role in the wind region (e.g. Katz, 1976, Ross, 1979, Sunyaev and Titarchuk, 1980, Guilbert, 1981) This leaves open the question whether a supercritical wind necessarily impresses spectral features on an arbitrary input spectrum. I have in mind here particularly the possibility that a supercritical outflow be compatible with the observation of a 'canonical' X-ray spectrum generated deep in the potential well of a supermassive black hole. Thus, in this chapter, I look at the Comptonization in a radiation pressure driven spherical wind of

a power law spectrum $F_\nu \propto \nu^{-0.7}$. I take this to be representative of a power law spectrum harder than $F_\nu \propto \nu^{-1}$ and thus includes, qualitatively, the possibility that the true primary AGN spectrum is $\nu^{-0.9}$. The limits on the γ-ray background (Bassani, *et al.*, 1985) require that the spectrum be cut off at some high $\nu = \nu_{max}$. In contrast to Becker and Begelman, this input cut-off is taken to be related to the primary radiation mechanism generating the canonical power law and not to the electron temperature in the wind.

As a result of my numerical computations I find that the effect of the wind is to move the cut-off at ν_{max} to a lower frequency without significantly perturbing the power-law slope below the cut-off. Thus my main result is that a standard synchrotron or Compton origin for the canonical spectrum is compatible with the existence of a supercritical wind. Indeed, in the presence of such a wind, the electron-positron cauldron model (Bonometto and Rees, 1971, Guilbert *el.*, 1983) can be viable for a range of compactness parameters (those for which the unbroken power law spectrum extends to γ-ray energies) without violating the γ-ray background constraints (because Comptonisation moves the break in the spectrum to hard X-rays). Of course, such models may also be viable for other reasons (Done and Fabian, 1989); the point I am making here is that if an active nucleus contains a supercritical mass outflow the allowed range of compactness parameters is effectively unconstrained by the γ-ray background.

I remark that the observation of short term variability in X-rays provides a restriction on the possible mass outflow rates. If timescales of $\sim 10^5$ s are indicative of a radius of $\sim 10^{15}$ cm for the X-ray region, then a mass outflow rate of $\sim 1 M_\odot$ yr^{-1} is indicated. If the outflow contains a large fraction of electron-positron pairs this mass flow rate is highly supercritical.

In the following sections I set up the equations of motion for the radiation transfer in a given outflow and the equations of motion of the matter in a given radiation field following Becker and Begelman (1986a). These equations are manipulated to separate the dynamics from the spectral evolution. I set up a finite difference scheme in section 2.4 which solves the integral equation for the spectral evolution iteratively. This gives the spectrum of the radiation field as a function of the Compton parameter y (section 2.2) which enables me to solve for the dynamics and hence determine the mass outflow rate. Finally, I calculate the observed spectra from these results using the method of Becker and Begelman.

I also apply my results to a conical outflow where the observed radiation would be that emitted from the side of the cone. This introduces a curvature into the X-ray spectrum. Thus I argue that the X-ray emission in sources which do not show evidence of superluminal motion could

result from Comptonization in an optically thick, radiation pressure driven, mildly relativistic jet. (The highly relativistic jets appropriate to the superluminal sources cannot be driven by radiation pressure so the self-consistency between the spectrum and the dynamics addressed here is not relevant.)

2.2 Radiative Transfer in a Wind

My discussion follows that of Becker and Begelman (1986a). From Blandford and Payne (1981) we can write down the modified Kompaneets equation for Compton scattering in an optically thick moving fluid under the diffusion approximation in a co-moving frame:

$$u\nabla\bar{n} = \frac{1}{3\sigma_T}\nabla.\left(\frac{1}{n_e}\nabla\bar{n}\right) + \frac{1}{3}\nabla.(u\hat{r})\nu\frac{\partial\bar{n}}{\partial\nu} + \frac{n_e\sigma_T h}{m_e c^2}\frac{1}{\nu^2}\frac{\partial}{\partial\nu}\left[\nu^4\left(\bar{n} + \frac{kT_e}{h}\frac{\partial\bar{n}}{\partial\nu}\right)\right]. \qquad (2.1)$$

The first, second and third terms on the right hand side of equation (2.1) represent the spatial diffusion of photons, adiabatic cooling and interactions due to Compton processes, respectively. The velocity of the fluid is $u(r)$, measured in units of the speed of light, c; $n_e(r)$ and $T_e(r)$ are the electron density and temperature respectively. The photon occupation number (the density of photons in phase space) $\bar{n}(\nu, r)$ is related to the total photon density n_r by

$$n_r = \frac{8\pi}{c^3}\int_0^\infty \nu^2\bar{n}(\nu, r)d\nu. \qquad (2.2)$$

I am interested here in situations where the radiation is trapped in the flow: the balance of energy between photons and electrons is determined entirely by adiabatic cooling and inelastic Compton scattering. Also the outward flow velocity of the photons is the same as the flow velocity of the electrons, so spatial diffusion of photons, in the co-moving frame, is negligible and the first term on the right hand side of (2.1) can be neglected, yielding, assuming spherical symmetry

$$u\frac{\partial\bar{n}}{\partial r} = \frac{1}{3r^2}\frac{d}{dr}(r^2u)\nu\frac{\partial\bar{n}}{\partial\nu} + \frac{n_e\sigma_T h}{m_e c^2}\frac{1}{\nu^2}\frac{\partial}{\partial\nu}\left[\nu^4\left(\bar{n} + \frac{kT_e}{h}\frac{\partial\bar{n}}{\partial\nu}\right)\right]. \qquad (2.3)$$

This is a first order partial differential equation for $\bar{n}(\nu, r)$, but involves the unknown functions describing the dynamics, $u(r)$, $n_e(r)$ and $T_e(r)$. However, by suitable changes of variable, equation (2.3) can be written in a form such that this information is not required to find a solution. I follow Becker and Begelman (1986a) by defining

$$\chi(\nu, r) = \frac{h\nu}{kT_e(r)}, \qquad (2.4)$$

$$y(r) = \int_{r_i}^{r}\frac{n_e\sigma_T kT_e}{m_e c^2}\frac{dr}{u} = \int_0^{N_{es}}\frac{kTe}{m_e c^2}dN_{es}, \qquad (2.5)$$

where N_{es} is the average number of scattering per photon between radii r_i and r. Equation (2.4) defines a dimensionless frequency χ and equation (2.5) defines the frequency independent Compton y parameter, written in a form more useful to moving fluids. Generally, significant changes in the spectral shape are expected as y exceeds unity (Rybicki and Lightman 1979).

Upon making these changes of variable, I obtain a dimensionless equation representing the radiation transfer in the trapped region of the flow:

$$\frac{\partial \bar{n}}{\partial y} = -\chi \frac{\partial \bar{n}}{\partial \chi} \frac{d}{dy} \ln \left(n_e^{\frac{1}{3}} T_e^{-1} \right) + \frac{1}{\chi^2} \frac{\partial}{\partial \chi} \left[\chi^4 \left(\bar{n} + \frac{\partial \bar{n}}{\partial \chi} \right) \right]. \tag{2.6}$$

I now define a temperature function $f(y)$ such that

$$f(y) = \frac{T_e}{T_{e_i}} \left(\frac{n_e}{n_{e_i}} \right)^{-\frac{1}{3}}, \tag{2.7}$$

where the subscript i denotes quantities measured at some initial radius, r_i, from which the calculation is started. (I do not consider the production mechanism within this radius.) The function $f(y)$ is a measure of the deviation of the electron temperature from photon dominated adiabatic behaviour. Setting

$$F(y) = \frac{d}{dy} \ln f(y), \tag{2.8}$$

the radiative transfer equation (2.6) can be written as

$$\frac{\partial \bar{n}}{\partial y} = \chi \frac{\partial \bar{n}}{\partial \chi} F(y) + \frac{1}{\chi^2} \frac{\partial}{\partial \chi} \left[\chi^4 \left(\bar{n} + \frac{\partial \bar{n}}{\partial \chi} \right) \right]. \tag{2.9}$$

Now, the function $f(y)$ is determined by the transfer of energy between the radiation field and the plasma. Consider the photon energy density

$$U_r = \frac{8\pi (kT_e)^4}{(ch)^3} \int_0^\infty \chi^3 \bar{n}(\chi, y) d\chi. \tag{2.10}$$

By operating on equation (2.6) by $\int_0^\infty \chi^3 d\chi$ and integrating by parts twice, I obtain a differential equation governing the photon energy density

$$\frac{dU_r}{dy} = \frac{4}{3} U_r \frac{d}{dy} \ln n_e + 4 \left(1 - \frac{T_C}{T_e} \right) U_r, \tag{2.11}$$

where T_c is the Compton temperature (the temperature of a thermal distribution of electrons at which there is no net energy exchange between the electrons and the ambient radiation field by Compton scattering):

$$\frac{T_C}{T_e} = \frac{1}{4} \frac{\int_0^\infty \chi^4 \bar{n}(\chi, y) d\chi}{\int_0^\infty \chi^3 \bar{n}(\chi, y) d\chi}. \tag{2.12}$$

Integration of equation (2.11) gives

$$\frac{U_r}{U_{r_i}}\left(\frac{n_e}{n_{e_i}}\right)^{-\frac{4}{3}} = \exp\left[\int_0^y 4\left(1-\frac{T_C}{T_e}\right)dy\right] = D(y). \tag{2.13}$$

On inspection of equation (2.11) I write down a differential equation for the electron energy density: replacing the photon adiabatic index $\left(\frac{4}{3}\right)$ with the electron adiabatic index $\left(\frac{5}{3}\right)$ and changing the sign of the last term, since energy lost by the photons due to Compton processes is gained by the electrons. Note that there is a factor of two difference between the term in each equation that represents the Compton processes: this is because the total gas energy density is twice the electron energy density:

$$\frac{dU_e}{dy} = \frac{5}{3}U_r\frac{d}{dy}\ln n_e - 2\left(1-\frac{T_C}{T_e}\right)U_r. \tag{2.14}$$

Dividing by $U_{e_i} = 3n_{e_i}kT_{e_i}/2$ and using equations (2.7) and (2.13) gives

$$\frac{df}{dy} - \frac{1}{3}f(y)\frac{d}{dy}\ln n_e = -\frac{1}{2}\frac{U_{r_i}}{U_{e_i}}\frac{dD}{dy} = (1-R)\frac{dD}{dy}, \tag{2.15}$$

where

$$R = 1 + \frac{1}{2}\left(\frac{U_{r_i}}{U_{e_i}}\right). \tag{2.16}$$

If $U_{r_i}/U_{e_i} \gg 1$ then equation (2.14) indicates that the electron temperature is driven rapidly towards the Compton temperature and that while this occurs, the density of the electrons remains essentially unchanged. So the second term in equation (2.15) can be ignored. Integrating equation (2.15) thus gives

$$f(y) = 1 - \frac{1}{2}\left(\frac{U_{r_i}}{U_{e_i}}\right)[D(y)-1] = R + (1-R)D(y). \tag{2.17}$$

Note that by combining equations (2.7), (2.10) and (2.13), $D(y)$ can be written:

$$D(y) = f^4(y)\frac{\int_0^\infty \chi^3\bar{n}(\chi,y)d\chi}{\int_0^\infty \chi^3\bar{n}(\chi,0)d\chi}, \tag{2.18}$$

giving the temperature function

$$f(y) = \frac{R}{1-(1-R)f^3(y)\frac{\int_0^\infty \chi^3\bar{n}(\chi,y)d\chi}{\int_0^\infty \chi^3\bar{n}(\chi,0)d\chi}}. \tag{2.19}$$

From equation (2.15)

$$\frac{df}{dy} = (1-R)\frac{dD}{dy}, \tag{2.20}$$

and from equation (2.13) I write

$$\frac{1}{D}\frac{dD}{dy} = 4\left(1 - \frac{T_c}{T_e}\right). \tag{2.21}$$

Using equations (2.8) and (2.17) gives us

$$\frac{1}{f}\frac{df}{dy} = F(y) = 4\left(1 - \frac{T_c}{T_e}\right)\left(1 - \frac{R}{f}\right), \tag{2.22}$$

which finally becomes

$$F(y) = \frac{\left(4\int_0^\infty \chi^3 \bar{n}(\chi, y)d\chi - \int_0^\infty \chi^4 \bar{n}(\chi, y)d\chi\right)(1-R)\,f^3}{\int_0^\infty \chi^3 \bar{n}(\chi, 0)d\chi}. \tag{2.23}$$

The spectra of the radiation is given by the solution of the radiative transfer equation (2.9) with $F(y)$ given by (2.23) and the relation between the temperature $T_e(y)$ and density $n_e(y)$ as given by equations (2.7) and (2.19). The dynamics of the wind will determine how the y-parameter depends on radius. The problem of the radiative transfer and the dynamics can thereby be separated.

2.3 The Wind Dynamics

To obtain the temperature, density and velocity in the wind as functions of radius I use the method of Becker and Begelman (1986b), but with a modification that simulates the effect of including electron-positron pairs in the gas.

First, I follow Becker and Begelman (1986b) by defining a number of dimensionless variables: $x = r/r_g$,the radius in units of the Schwarzschild radius of the central black hole; a dimensionless temperature $T = P_r/Q$ where $Q = \rho c^2$, the radiation pressure divided by the rest mass energy density of the gas; and the spatial component of the four-velocity of the gas, as measured by a stationary observer at infinity, $\tilde{u} = (1/c)dr/d\tau$ (τ is the proper time in the Schwarzschild metric). In the following, the subscript 'i' refers to quantities measured at the initial radius and the subscript 'c' refers to quantities measured at the critical point where the velocity equals the adiabatic sound speed.

Becker and Begelman (1986b) use equations derived by Michel (1972) and revisited by Begelman (1978) that describe the steady state, radiation dominated, spherical flow of an ideal fluid in the Schwarzschild metric,

$$Q\tilde{u}x^2 = \frac{\dot{M}c}{4\pi r_g^2}, \tag{2.24}$$

$$\left(\frac{P_r+\mu}{Q}\right)\left(1-\frac{1}{x}+\tilde{u}^2\right)=B_1. \tag{2.25}$$

Equation (2.24) comes from the conservation of mass in spherically symmetric flow and is equivalent to the more usual form, $\dot{M}=4\pi r^2\tilde{u}c\rho$. Equation (2.25) is Bernoulli's equation and comes from *(conservation of momentum)* $\div$ *(conservation of mass)*; here μ is the total energy density. The radiation is trapped within the flow so the photon pressure decreases adiabatically as

$$P_r \propto \rho^{\frac{4}{3}}, \tag{2.26}$$

for which

$$P_r+\varepsilon=4P_r, \tag{2.27}$$

were ε is the internal energy. Now $\mu=Q+\varepsilon$ so

$$P_r+\mu=Q+4P_r=Q(1+4T), \tag{2.28}$$

and so equation (2.25) becomes Becker and Begelman (1986b) equation (2.2)

$$(1+4T)^2\left(1-\frac{1}{x}+\tilde{u}^2\right)=B_1 \tag{2.29}$$

Integration of equations (2.24) and (2.29) and eliminating dQ gives the wind equation

$$\frac{d\tilde{u}}{\tilde{u}}\left(V^2-\frac{\tilde{u}^2}{1-\frac{1}{x}+\tilde{u}^2}\right)+\frac{dx}{x}\left(V^2-\frac{1}{2x\left(1-\frac{1}{x}+\tilde{u}^2\right)}\right)=0, \tag{2.30}$$

where

$$V^2=\frac{4T}{3(1+4T)}. \tag{2.31}$$

There is a critical point in equation (2.30) when both bracketed terms vanish simultaneously, which occurs when

$$\tilde{u_c}^2=\frac{1}{4x_c}, \tag{2.32}$$

$$V^2=\frac{\tilde{u_c}^2}{1-3\tilde{u_c}^2}. \tag{2.33}$$

The dimensionless flow velocity measured by a stationary observer is

$$u=\frac{\tilde{u}^2}{\left(1-\frac{1}{x}+\tilde{u}^2\right)^{\frac{1}{2}}}; \tag{2.34}$$

at the critical point x_c this becomes

$$u_c=\frac{\tilde{u}_c}{(1-3\tilde{u}^2)^{\frac{1}{2}}}=V, \tag{2.35}$$

and so V is clearly the adiabatic sound speed at x_c. Combining equations (2.31), (2.32) and (2.33) gives

$$T_c = \frac{3}{16\left(x_c - \frac{3}{2}\right)}. \tag{2.36}$$

The constant on the right hand side of equation (2.29) can be found using equations (2.32) and (2.36):

$$B_1 = \frac{\left(x_c - \frac{3}{4}\right)^3}{x_c\left(x_c - \frac{3}{2}\right)^2}. \tag{2.37}$$

Now $T_c = P_r/\rho c^2$, so from equation (2.26)

$$\frac{T}{T_c} = \left(\frac{\rho}{\rho_c}\right)^{\frac{1}{3}}, \tag{2.38}$$

also, equation (2.24) may be written

$$Q\tilde{u}^2x^2 = Q_c\tilde{u}_c^2x_c^2 = \frac{\dot{M}c}{4\pi r_g^2} = \text{constant} \tag{2.39}$$

and using equation (2.28)

$$\frac{\rho}{\rho_c} = \frac{x_c^{\frac{3}{2}}}{2\tilde{u}x^2}. \tag{2.40}$$

Using equations (2.37) in (2.29) and combining (2.36), (2.38) and (2.39) I arrive at the following two equations

$$(1+4T)^2\left(1 - \frac{1}{x} + \tilde{u}^2\right) = \frac{\left(x_c - \frac{3}{4}\right)^3}{x_c\left(x_c - \frac{3}{2}\right)^2}, \tag{2.41}$$

$$T = \frac{3}{16\left(x_c - \frac{3}{2}\right)}\frac{x_c^{\frac{1}{2}}}{(2\tilde{u}x^2)^{\frac{1}{3}}}. \tag{2.42}$$

Equations (2.41) and (2.42) are solved as follows: I choose a suitable electron temperature, T_{e_i}, at the injection radius and also a suitable value for U_{r_i}/U_{e_i} (which is a parameter for the spectral evolution calculation). Now $T = P_r/\rho c^2$ and the gas pressure $P_g = \rho k T_e/\langle m\rangle$; also $P_r = \frac{1}{3}U_r$ and $P_g = \frac{4}{3}U_e$. The initial value of T is then

$$T_i = \frac{kT_{e_i}}{4\langle m\rangle c^2}\frac{U_{r_i}}{U_{e_i}}. \tag{2.43}$$

For a given T_i, x_c decreases as x_i increases, until the two are coincident at $x_i = x_c = x_{max}$. Using equation (2.42) along with $\tilde{u}_i = \tilde{u}_c$ in equation (2.32)

$$x_{max} = \frac{3}{2}\left(1 + \frac{1}{8T_i}\right). \tag{2.44}$$

If x_i decreases for a given T_i, more energy is required to propel a given mass out to infinity, causing a smaller terminal velocity, which leads to a smaller $\tilde{u}_c$ and therefore to a larger sonic radius. As x_i decreases, $x_c \to \infty$, so for $x_c < x_{min}$ the flow never passes through a critical point. To estimate x_{min} note that if $x_c \gg 1$, from equation (2.37) $B_1(x_c) \simeq 1$, while from equation (2.32) $\tilde{u}_c$ and hence $\tilde{u}_i$ is negligibly small, so equation (2.41) becomes

$$(1+4T_i)\left(1-\frac{1}{x_{min}}\right) \simeq 1, \tag{2.45}$$

or

$$x_{min} \simeq \left(1-(1+4T_i)^{-2}\right)^{-1}. \tag{2.46}$$

Equations (2.41) and (2.42) are solved for $\tilde{u}_i$ and x_c given the initial conditions T_{e_i}, U_{r_i}/U_{e_i} at x_i. This is done by rearranging equation (2.42) to get $\tilde{u}_i$ in terms of T_i, x_i and x_c, and substituting the result into equation (2.41), from which x_c is found by numerical solution using the HYBRD non-linear equation solving method (Garbow *et al.*, 1980). The initial value $\tilde{u}_i$ is then evaluated using equation (2.42).

I now have x_c and can solve the equations for $T(x)$ and $\tilde{u}(x)$. This time I substitute (2.42) into (2.41) giving an equation in terms of $\tilde{u}$, x and x_c, which is solved numerically as before; T is evaluated by substituting the results back into equation (2.42).

The electron density $n_e(x)$ is evaluated by considering the mass outflow rate, which must be constant in a steady flow:

$$\dot{M} = 4\pi r_g^2 m_p c n_e \tilde{u} x^2. \tag{2.47}$$

It is convenient to define the Eddington limited mass outflow rate $\dot{M}_E \equiv L_E/c^2$:

$$\dot{M}_E = \frac{4\pi G M m_p}{\sigma_T c}. \tag{2.48}$$

Rearranging equations (2.47) and (2.48) yields

$$n_e = \frac{c^2}{4\sigma_T G M}\left(\frac{\dot{M}}{\dot{M}_E}\right)\frac{1}{\tilde{u}x^2}, \tag{2.49}$$

or

$$n_e = 2.54\times 10^{10}\left(\frac{\dot{M}}{\dot{M}_E}\right)\frac{1}{\tilde{u}x^2} m_8^{-1}. \tag{2.50}$$

Next, I evaluate the Compton y parameter as a function of x, from equations (2.5) this is

$$y(x) = \int_{x_i}^{x} \frac{n_e \sigma_T k T_e}{m_e c^2}\frac{r_g dx}{\tilde{u}} \tag{2.51}$$

which may be written

$$y(x) = \frac{n_{e_i}\sigma_T k T_{e_i} x_i r_g}{m_e c^2 \tilde{u}_i} \int_1^{\frac{x}{x_i}} \frac{n_e}{n_{e_i}} \frac{T_e}{T_{e_i}} \left(\frac{\tilde{u}}{\tilde{u}_i}\right)^{-1} d\frac{x}{x_i}. \tag{2.52}$$

Using the temperature function $f(y)$ defined by equation (2.7)

$$y(x) = \Lambda \int_1^{\frac{x}{x_i}} f(y) \left(\frac{n_e}{n_{e_i}}\right)^{\frac{4}{3}} \left(\frac{\tilde{u}}{\tilde{u}_i}\right)^{-1} d\frac{x}{x_i}, \tag{2.53}$$

where

$$\Lambda = \frac{n_{e_i}\sigma_T k T_{e_i} x_i r_g}{m_e c^2 \tilde{u}_i} = \frac{1}{2\tilde{u}_i^2 x_i} \left(\frac{\dot{M}}{\dot{M}_E}\right) \frac{k T_{e_i}}{m_e c^2}. \tag{2.54}$$

from equation (2.49). Following equation (2.39)

$$\frac{n_e}{n_{e_i}} = \left(\frac{x}{x_i}\right)^{-2} \left(\frac{\tilde{u}}{\tilde{u}_i}\right)^{-1}, \tag{2.55}$$

and so

$$\int_o^{y(x)} \frac{dt}{f(t)} = \Lambda \int_1^{\frac{x}{x_i}} \left(\frac{\tilde{u}}{\tilde{u}_i}\right)^{-\frac{7}{3}} \left(\frac{x}{x_i}\right)^{-\frac{8}{3}} d\left(\frac{x}{x_i}\right). \tag{2.56}$$

Hence, the electron temperature can be found from the definition of $f(y)$:

$$T_e(x) = T_{e_i} f\left(y(x)\right) \left(\frac{n_e(x)}{n_{e_i}}\right)^{\frac{1}{3}}. \tag{2.57}$$

In this discussion I have assumed that the optical depth below the critical radius is sufficiently large that the flow velocity exceeds the diffusion velocity of the photons. Thus the critical radius must be significantly smaller than the trapping radius r_t (the radius below which the photons are trapped in the flow). Given that r_t is defined by

$$\tau_{es}(r_t) u(r_t) = 1, \tag{2.58}$$

where τ_{es} is the optical depth to Compton scattering, and also considering equations (2.47) and (2.48), this condition becomes

$$r_c \ll r_t \equiv \frac{r_g}{2} \frac{\dot{M}}{\dot{M}_E}. \tag{2.59}$$

Therefore allowed values of $\left(\dot{M}/\dot{M}_E\right)$ in equations (2.49) and (2.50) are governed by x_c calculated previously; conversely, for a given mass outflow rate there is a maximum x_c such that these calculations are valid. It is clear that $\left(\dot{M}/\dot{M}_E\right)$ is required to be very large but it is unlikely that the majority of AGN have such supercritical outflows. This constraint can be relaxed if the wind contains a significant number of electron-positron pairs.

I assume that the pair density is specified at the injection radius; I do not consider the mechanism by which they are produced, this mechanism could be via mechanical processes, alfvenic dissipation or relativistic electrons from the synchrotron emitting region. For simplicity, I neglect pair annihilation. This is reasonable as far as the dynamics are concerned if the energy in the pairs is comparable with that in the gamma radiation since, in the region near r_i where most of the dynamical evolution occurs, the pair density will be in equilibrium. Once the radiation is no longer trapped the pair annihilation will be small. This assumption is verified by the results in section 2.7. Neglecting pair annihilation is therefore valid as a first approximation. However, any spectral features due to pair annihilation are being ignored.

There are two ways in which the inclusion of pairs effects the model. First, there is an effective decrease in $\dot{M}_E$. For a gas with z pairs per proton, $\dot{M}_E$ is decreased by a factor $(1+z)$:

$$\dot{M}_E = \frac{4\pi GM}{\sigma_T c}\frac{m_p}{1+z}. \tag{2.60}$$

Thus for a given $\dot{M}$, $\left(\dot{M}/\dot{M}_E\right)$ will be larger by a factor $(1+z)$, easing the condition given by equation (2.59). This is because the energy transfer from the radiation to the matter is proportional to the density of electrons, but the inertia of the wind is proportional to the protons, therefore when there are more electrons per proton, the radiation transfer required to accelerate the proton by a given amount is less, and so the effective Eddigton limit in the wind is decreased by a factor $(1+z)$. Therefore the quantity n_e, as calculated using equation (2.50), will be smaller by this same factor.

The second effect can be seen by examining equation (2.43). The mean particle mass $\langle m\rangle$ is $m_p/2$ for a hydrogen plasma, but for a gas with z pairs per proton this becomes:

$$\langle m\rangle = \frac{m_p + m_e(1+2z)}{2(1+z)} \simeq \frac{m_p}{2(1+z)}. \tag{2.61}$$

This has the effect of increasing T_i, which will shorten the acceleration scale length.

2.4 Numerical Method

From the work of Becker and Begelman (1986a), there are the three equations (2.9), (2.19), and (2.23) that describe the spectral evolution of the radiation as a function of the Compton y parameter. To solve these equations I make two further changes of variable:

$$N(\chi, y) = \bar{n}(\chi, y) f^3(y)\chi^2, \tag{2.62}$$

$$x = \ln \chi. \tag{2.63}$$

First consider the reason for the change defined by equation (2.62): $Nd\chi$ is proportional to the number of photons per electron with energy $h\nu/kT_e$ between and $\chi + d\chi$, and is therefore a useful way of representing the spectrum. The total photon number density becomes

$$n_r = 8\pi \left(\frac{kT_e}{ch}\right)^3 \left(\frac{n_e}{n_{e_i}}\right) \int_0^\infty N(\chi, y) d\chi, \tag{2.64}$$

and $\int_o^\infty N d\chi$ is constant in a trapped flow. It also becomes easier to evaluate $f(y)$; from equation (2.20) I obtain

$$f(y) = \frac{R}{1 - (1-R)\frac{\int_0^\infty \chi N(\chi,y) d\chi}{\int_0^\infty \chi N(\chi,0) d\chi}}, \tag{2.65}$$

noting that $f(0) = 1$.

Without the second change of variable, defined by equation (2.63), a numerical method of solution would require non-uniform grid, with a higher gridpoint density at the smaller values of χ. This substitution allows a uniform grid for all x, though in practise more information is required at the larger values of x, so the gridpoint density can be low for large, negative x.

After making the two substitutions defined above, equations (2.9), (2.19) and (2.23) become

$$\frac{\partial N}{\partial y} = \frac{\partial^2 N}{\partial x^2} + (e^x - 1 + F(y)) \frac{\partial N}{\partial x} + (2e^x - 2 + F(y))\, N, \tag{2.66}$$

$$f(y) = \frac{R}{1 - (1-R)\frac{\int_{-\infty}^\infty e^{2x} N(x,y) dx}{\int_{-\infty}^\infty e^{2x} N(x,0) dx}}. \tag{2.67}$$

$$F(y) = \frac{\left(4\int_{-\infty}^\infty e^{2x} N(x,y) dx - \int_{-\infty}^\infty e^{3x} N(x,y) dx\right)(1-R)}{\int_{-\infty}^\infty e^{3x} N(x,0) dx}, \tag{2.68}$$

While the integrals in the equations above have an infinite range, in practice $N(x,y) \to 0$ as $x \to \infty$ and $e^{ax} N(x,y) dx \to 0$ as $x \to -\infty$, so finite bounds may be used for the numerical method.

Having chosen an input spectrum $N(x,0)$, the coupled equations (2.66) and (2.68) are used to evolve the spectrum numerically in the direction of increasing y, such that at any point y a self consistent solution $N(x,y)$ and $F(y)$ has been calculated before evolving to a larger value of y.

2.4.1 The Basic Scheme

Assume that $N(x,y)$ is known at some $y = y_j$ for all $x_a < x < x_b$. I represent $N(x,y)$ as the values $N_{i,j}$ at discrete points x_1, x_2, ..., x_i, ..., x_n; y_1, y_2, ..., y_j, ..., i.e. $N(x,y)$ is represented as $N_{i,j}\ \forall\ i$. I know the value of $F(y_j) = F_j$. To evaluate $N_{i,j+1}\ \forall\ i$ and F_{j+1} at $y_{j+1} = y_j + \Delta y$, I carry out the following steps:

(1) Calculate a first guess for $N_{i,j+1}\ \forall\ i$, which I call ${}_1N_{i,j+1}\ \forall\ i$, where $l = 0$, using the value F_j and a discretised version of equation (2.66):

$$\frac{\partial N}{\partial y} = \frac{{}_0N_{i,j+1} - N_{i,j}}{\Delta y} = \left(\frac{\partial^2 N}{\partial x^2}\right)_{i,j} + (e^{x_i} - 1 + F_j)\left(\frac{\partial N}{\partial x}\right)_{i,j} + (2e^{x_i} - 2 + F_j)\,N_{i,j} \tag{2.69}$$

(2) Calculate a first guess for $F(y_{j+1}) = {}_0F_{j+1}$ using the values ${}_0N_{i,j+1}$ calculated in step (1) and equation (2.68).

(3) Using the values ${}_lN_{i,j+1}$ and F_{j+1} calculate the next guess for $N_{i,j+1}$ using the discretised version of equation (2.66):

$$\frac{{}_{l+1}N_{i,j+1} - N_{i,j}}{\Delta y} = {}_l\left(\frac{\partial^2 N}{\partial x^2}\right)_{i,j} + (e^{x_i} - 1 + F_j)\,{}_l\left(\frac{\partial N}{\partial x}\right)_{i,j} + (2e^{x_i} - 2 + F_j)\,{}_lN_{i,j} \tag{2.70}$$

(4) Calculate the next guess for $F(y_{j+1}) = {}_lF_{j+1}$ using the values ${}_{l+1}N_{i,j+1}$ calculated in step (3) and equation (2.68).

(5) If the following accuracy check is false increment l by one and repeat steps (3), (4) and (5):

$$\frac{{}_{l+1}F_{j+1} - {}_lF_{j+1}}{{}_lF_{j+1}} < \varepsilon \ll 1 \tag{2.71}$$

When the solution $N_{i,j+1}\ \forall\ i$ is such that equation (2.71) is true, then I have self consistent solutions $N(x,y_{j+1})$ and $F(y_{j+1})$. Now $f(y_{j+1})$ can be evaluated using equation (2.67), so that the relationship between $T_{e_i}(y)$ and $n_{e_i}(y)$ can be established.

2.4.2 Evaluating the Derivatives

A second order difference scheme is used to evaluate the x derivatives of $N(x,y)$ at the grid point (i,j). For a uniform grid, $\Delta x = x_{i+1} - x_i$ and is constant for all i, and

$$\left(\frac{\partial^2 N}{\partial x^2}\right)_{i,j} = \frac{N_{i+1,j} - 2N_{i,j} + N_{i-1,j}}{(\Delta x)^2}, \tag{2.72}$$

$$\left(\frac{\partial N}{\partial x}\right)_{i,j} = \frac{N_{i+1,j} - N_{i-1,j}}{2\Delta x}. \tag{2.73}$$

For a non-uniform grid, the difference scheme is more complex and is written

$$\left(\frac{\partial^2 N}{\partial x^2}\right)_{i,j} = 2\frac{N_{i+1,j}(x_i - x_{i-1}) - N_{i,j}(x_{i+1} - x_{i-1}) + N_{i-1,j}(x_{i+1} - x_i)}{(x_{i+1} - x_i)(x_{i+1} - x_{i-1})(x_i - x_{i-1})}, \tag{2.74}$$

$$\left(\frac{\partial N}{\partial x}\right)_{i,j} = \frac{N_{i+1,j}(x_i - x_{i-1})^2 - N_{i,j}[(x_i - x_{i-1})^2 - (x_{i+1} - x_i)^2] - N_{i-1,j}(x_{i+1} - x_i)^2}{(x_{i+1} - x_i)(x_{i+1} - x_{i-1})(x_i - x_{i-1})}. \tag{2.75}$$

Generally a first order scheme is used to evaluate the y derivative of $N(x, y)$ at the grid point $(i, j+1)$. This scheme has already been shown in equations (2.69) and (2.70):

$$\left(\frac{\partial N}{\partial y}\right)_{i,j+1} = \frac{N_{i,j+1} - N_{i,j}}{\Delta y}. \tag{2.76}$$

However, because a second order scheme has been used to evaluate the first order x derivative of N at (i, j), using equation (2.76) can result in equations (2.69) and (2.70) becoming unconditionally unstable if $\frac{\partial N}{\partial x} \ll 1$. Hence, where there is a positive gradient in the x direction a second order scheme is used instead:

$$\left(\frac{\partial N}{\partial y}\right)_{i,j+1} = \frac{N_{i,j+1} - \langle N_{i,j}\rangle}{\Delta y}, \tag{2.77}$$

here $\langle N_{i,j}\rangle$ is the average of $N_{i-1,j}$ and $N_{i,j}$, weighted according to the differences $(x_{i+1} - x_i)$ and $(x_i - x_{i-1})$:

$$\langle N_{i,j}\rangle = \frac{N_{i+1,j}(x_i - x_{i-1}) - N_{i-1,j}(x_{i+1} - x_i)}{x_{i+1} - x_{i-1}}. \tag{2.78}$$

2.4.3 Boundary Conditions

Becker and Begelman (1986a) chose initial spectra that were all of the form $\bar{n}(\chi, 0) = \chi^{-\alpha}e^{-\chi}$, it is relatively easy to derive analytical approximations to the solutions to use as boundary conditions. Their initial spectra can all be written as a power law, $\chi^{-\alpha+3}$, modified by a Wien spectrum, $\chi^{-3}e^{-\chi}$, i.e. the characteristic temperature of the photons in the Wien spectrum was the same as the electron temperature since $\chi = h\nu/kT_e$. At large χ these spectra tend towards pure Wien spectra, which makes the analytical solution much easier than for a spectrum without this property. However, for an arbitrary initial spectrum an analytical approach does not work. I chose the following numerical approaches.

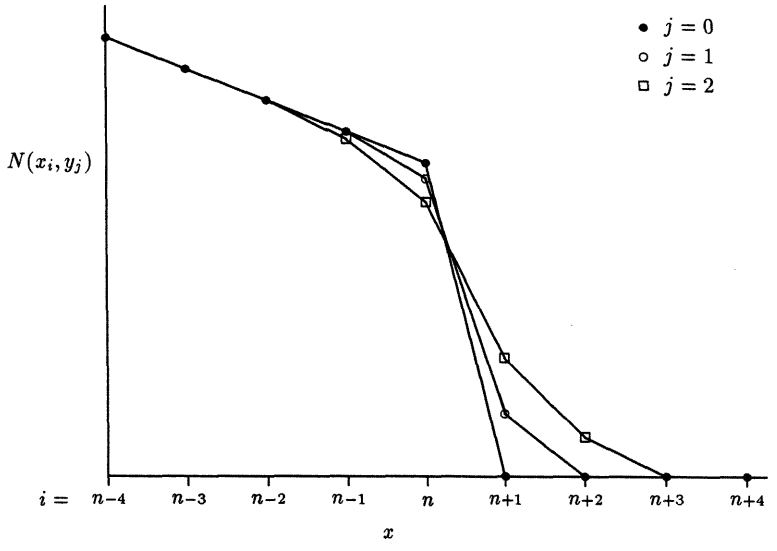

Figure 2.1: An illustration of the behaviour at $N(x,y)$ at the upper boundary, showing the first two steps in the y-direction: $j = 0$ gives the initial spectrum, when $y = 0$, with a cutoff above x_n; $j = 1$ and $j = 2$ show the initial evolution of the cutoff to $y = \Delta y$ and $y = 2\Delta y$, respectively.

As x increases, for any reasonable spectrum $N \to 0$, so the grid is extended to above the point where $N(x,y) = 0$, and the photons are simply allowed to diffuse upwards in x, with additional grid points being added as necessary, see figure 2.1.

There are two potential problems with this approach. First as y increases the number of grid points increases as the photons diffuse upwards in x. This is not as bad as it may seem because the rate of addition of grid points decreases as y increases, and eventually stops as the spectrum at large x tends towards a Wien spectrum.

The second problem is that the density of grid points at larger x must increase to prevent the numerical solution becoming unstable, and because of this a correspondingly larger grid point density in the y direction is required, since numerical stability requires $\Delta y \sim (\Delta x)^2$. This results in the calculation slowing down by a cubic factor, and eventually, if the highest value for x is large enough, it is no longer practical to continue.

For the lower boundary, one of two methods is used. If the initial spectrum is such that the gradient $\frac{\partial}{\partial x}(\ln N) < 1$ for gridpoints near the lower x boundary, and $N(x_1, y) > 0$ (for example

a power law spectrum $F_\nu \propto \nu^{-\alpha}$ with the energy index $\alpha < 1$), then the lower boundary at x_1 is simply extrapolated from the values of N at x_2, x_3 and x_4. This is satisfactory if $x_1 \ll x_n$, i.e. the frequency of the photons at the lower boundary is much less than than the frequency region of interest. For this kind of initial spectrum a non-uniform grid is used: a much lower grid point density is needed for low values of x than for the region of interest. The grid has to be extended to x values much lower than the region of interest to maintain accuracy while evaluating the integrals in equations (2.68) and (2.67).

However, for other initial spectra such as steep power laws (energy index $\alpha > 1$) or black body spectra, this extrapolation is invalid: for black body spectra, $N(x, y) \to 0$ as x decreases, and for steep power laws there must be a low frequency cutoff because most of the energy in the spectrum resides in the lowest frequency photons. In these cases a diffusive boundary identical to the large x boundary is used: points with $N = 0$ are added at the bottom end of the grid as the photons diffuse downwards. For this second kind of initial spectrum, more detail is required for low values of x to maintain the stability of the solution at the lower boundary, and so a uniform grid is used.

Neither of the methods outlined above is really ideal, but it is possible to produce results for a useful range of y, for some initial spectra, by simply throwing a lot of computer power at the problem!

2.5 Spectral Results

I have computed spectral evolution for the following cases:

A $N(\chi, 0) = \chi^{-1.7}$ for $\chi < 10$, $(U_r/U_e)_i = 100$.

B $N(\chi, 0) = \chi^{-1.7}$ for $\chi < 10$, $(U_r/U_e)_i = 1000$.

C $N(\chi, 0) = \chi^{-1} e^{-\chi}$ for $\chi < 90$, $(U_r/U_e)_i = 100$.

Cases A and B correspond to a flux power law $F_\nu \propto \nu^{-0.7}$ with a high energy cutoff at 1 MeV when the initial temperature $T_{e_i} = 10^9$ K (or 10 MeV for $T_{e_i} = 10^{10}$ K). Case C has an optically thin bremsstrahlung initial spectrum, as used by Becker and Begelman (1886a): $\bar{n}(\chi, 0) = \chi^{-3} e^{-\chi}$ with a high energy cutoff at approximately 10 MeV.

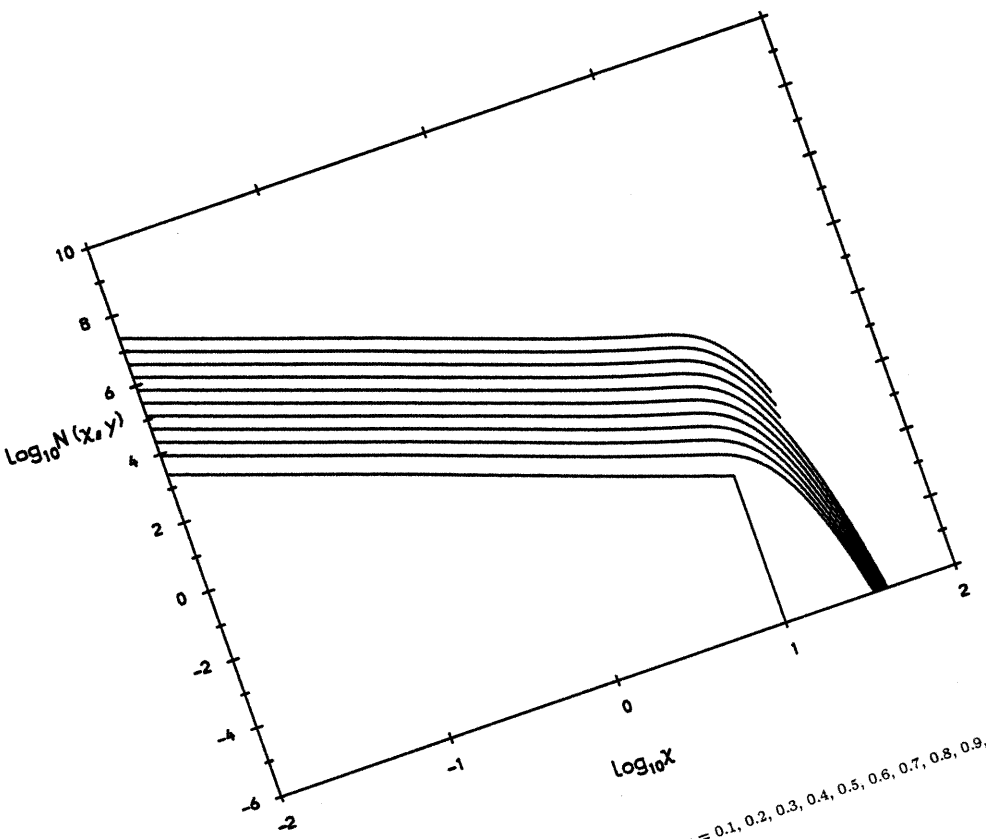

Figure 2.2: Case A results for $y = 0$ (lower lefthand line), through $y = 0.1, 0.2, 0.3, 0.4, 0.5, 0.6, 0.7, 0.8, 0.9$, to $y =$ 1.0 (upper righthand line)

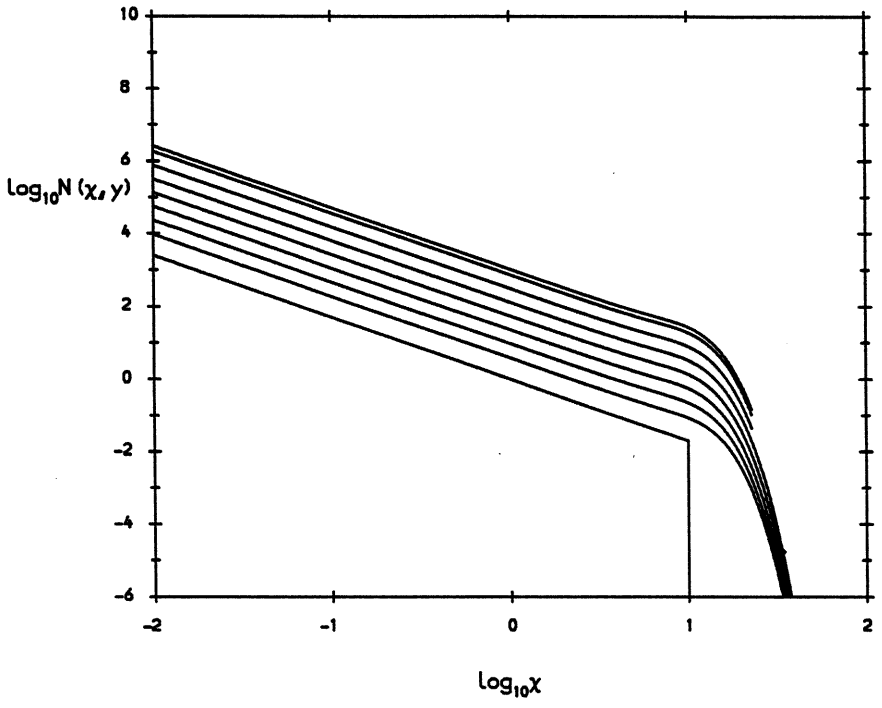

Figure 2.3: Case B results for $y = 0$ (lower lefthand line), through $y = 0.1$, 0.2, 0.3, 0.4, 0.5, 0.6, 0.7, to $y = 0.74$ (upper righthand line)

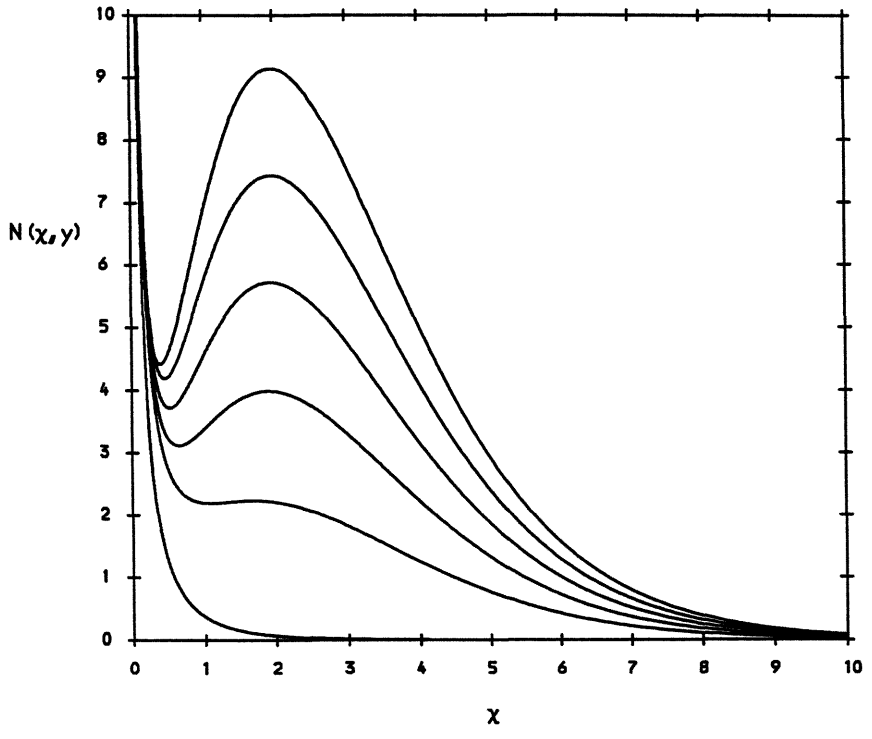

Figure 2.4: Case C results for $y = 0$ (lower line), through $y = 2$, 4, 6, 8 to $y = 10$ (upper line)

The spectral evolution was computed to $y = 1.04$ for case A, and to $y = 0.74$ for case B. The evolution was not continued any further because the calculations become more computationally expensive: as the photons diffuse to higher frequencies, the grid points become so dense that to continue is no longer practical. To evolve to these values of y required approximately 1000 hours of CPU time on a VAX 8650; each further 0.01 step in y would have required more than 10 hours. However, later calculations that determine the properties of the wind and the emergent spectra show that it was not necessary to carry on computing the evolution of the spectrum any further. The results obtained for cases A and B are shown in figures (2.2) and (2.3).

The spectral evolution in case C was computed to $y = 10$, to compare my numerical method with the one used by Becker and Begelman (1986a). The results from these calculation are shown in figure (2.4) which gives $N(\chi, y)$ for various y.

The spectral evolution calculated for case C matches that produced by Becker and Begelman (1986a) which gives credence to the results for cases A and B.

I also attempted to compute the spectral evolution for the following initial spectra:

- A power law as in cases A and B combined with a black body at a temperature of 10^5 K, with equal energy in each component:

$$N(\chi, 0) = \chi^{-1.7} + A\frac{\chi^2 e^{-\chi T_{e_i}/T_{BB}}}{1 - e^{-\chi T_{e_i}/T_{BB}}} \tag{2.79}$$

  A was chosen such that the energy in each component was the same. The power law has a high energy cutoff at 1 Mev and $(U_r/U_e)_i = 100$.

- $N(\chi,0) = \chi^{-2.5}$ for $-10 < \chi < 10$, $(U_r/U_e)_i = 100$. This corresponds to a flux power law $F_\nu \propto \nu^{-1.5}$ with a low energy cutoff around 1 eV and a high energy cutoff at 1 MeV when $T_{e_i} = 10^9$ K.

These computations failed for the following reasons:

(a) The spectrum is too steep so that the change in N between grid points in x is large compared with N itself. This leads to instability.

(b) The method does not work for positive gradients $dN/d\chi$ unless the spectrum is Wien-like.

(c) There are discontinuties in $\frac{\partial N}{\partial \chi}$ which cannot be handled by this method.

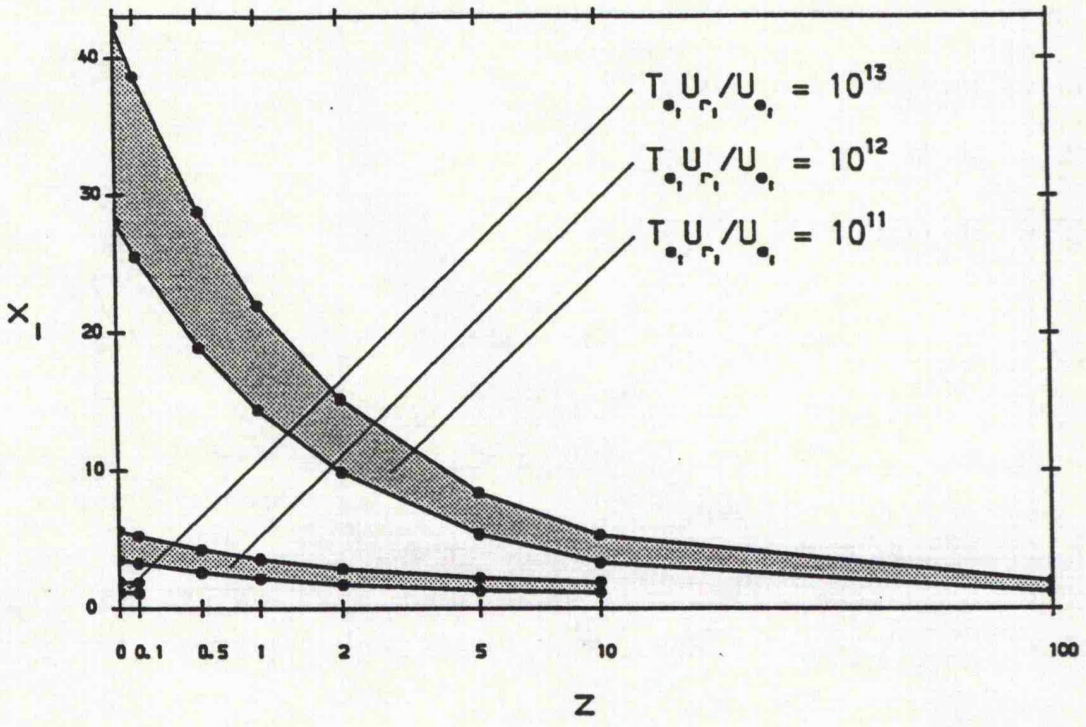

Figure 2.5: The allowed range of x_i vs. z for $T_{e_i} U_{r_i} / U_{e_i} = 10^{11}$, 10^{12} and 10^{13}.

2.6 Dynamics Results

In order to obtain the physical characteristics of the wind I use the method described in section 2.3. In all cases I assume that the mass of the central black hole is $10^8 M_\odot$. I first specify the initial temperature T_{e_i}, the initial ratio of radiation energy density to matter energy density U_{r_i}/U_{e_i} and the ratio of pairs to protons z. I choose initial temperatures of 10^9 K and 10^{10} K, so that the gas would be hot enough for electron-positron pairs to exist. U_{r_i}/U_{e_i} is a parameter to the spectral evolution computations. I choose a number of values for z as shown by tables 2.1 (for the cases A and B spectra) and 2.2 (for case B).

I then calculate the initial dimensionless temperature T_i, defined by equation (2.43), and hence x_{min} and x_{max} from equations (2.46) and (2.44), which define the range of values that I can choose for the initial radius x_i. The shaded regions in figure 2.5 show the allowed range of x_i plotted against z for various values of $T_{e_i} U_{r_i} / U_{e_i}$. For each z I choose one value of x_i that was approximately in the middle of of this range.

I then calculate the critical point radius x_c and the initial four-velocity $\tilde{u}_i$ of the wind, from

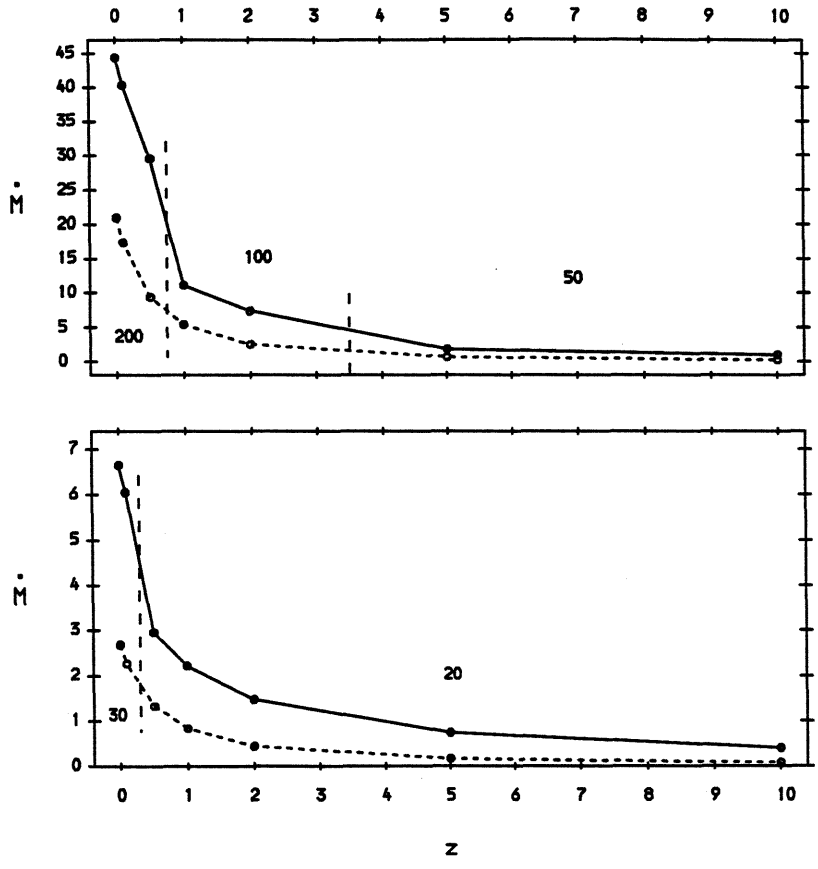

Figure 2.6: $\dot{M}$ against z for cases A and C, the numbers separated by vertical dashed lines refer to $\dot{M}/\dot{M}_E$.

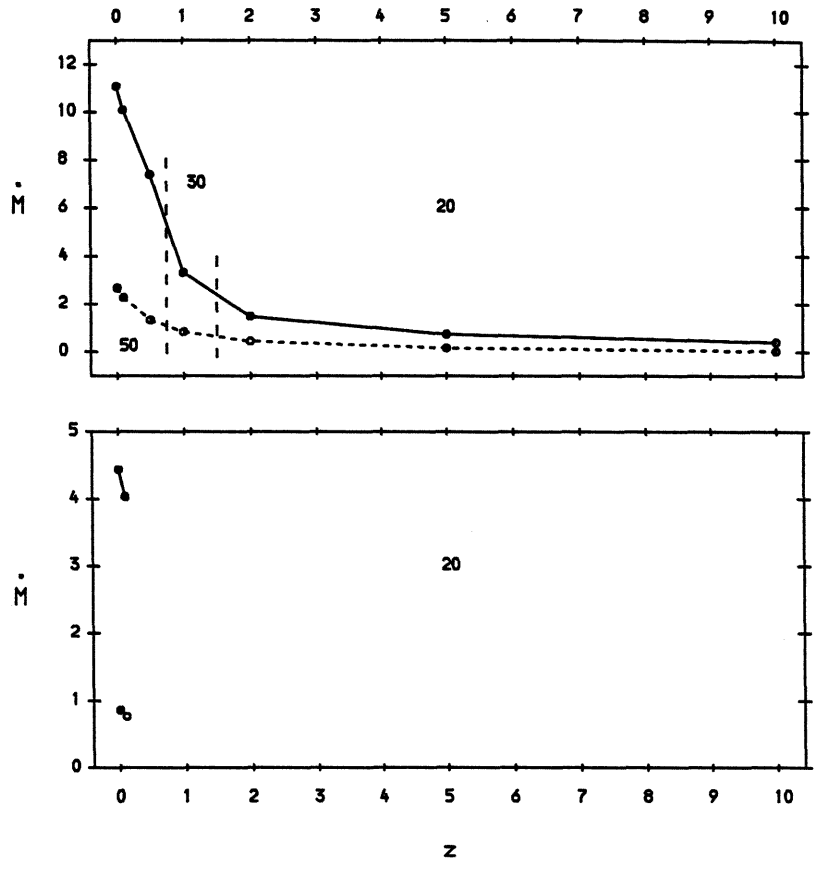

Figure 2.7: $\dot{M}$ against z for case B, the numbers separated by vertical dashed lines refer to $\dot{M}/\dot{M}_E$.

Table 2.1: Parameters for Cases A and C

$U_{r_i}/U_{e_i} = 100$

T_{e_i} (K)	z	x_i	$\frac{\dot{M}}{M_E}$	x_c	$\dot{M}$ ($M_\odot$ yr^{-1})	$\tilde{u}_i$	n_{e_i} (cm^{-3})
10^9	0	35.	200	47.27	44.39	0.0648*	6.42×10^{11}
	0.1	32.	200	43.05	40.36	0.0679*	6.65×10^{11}
	0.5	24.	200	31.78	29.59	0.0791*	7.44×10^{10}
	1	18.	100	22.45	11.10	0.0888*	4.42×10^{10}
	2	12.	100	17.09	7.399	0.103	5.74×10^{10}
	5	6.3	50	9.48	1.850	0.128	4.17×10^{10}
	10	4.2	50	5.69	1.009	0.168	3.90×10^{10}
	100	1.6	50	1.98	0.1099	0.226	2.18×10^{10}
10^{10}	0	4.5	30	6.05	6.659	0.166	2.28×10^{11}
	0.1	4.2	30	5.63	6.053	0.170	2.31×10^{11}
	0.5	3.4	20	4.51	2.959	0.185	1.58×10^{11}
	1	2.8	20	3.77	2.220	0.192	1.69×10^{11}
	2	2.3	20	3.00	1.480	0.209	1.53×10^{11}
	5	1.7	20	2.25	0.7399	0.199	1.47×10^{11}
	10	1.5	20	1.91	0.4036	0.205	1.00×10^{11}

* The initial four-velocity $\tilde{u}_i$ exceeds the escape velocity.

Table 2.2: Parameters for Case B

$U_{r_i}/U_{e_i} = 1000$

T_{e_i} (K)	z	x_i	$\frac{\dot{M}}{\dot{M}_E}$	x_c	$\dot{M}$ ($M_\odot$ yr^{-1})	$\tilde{u}_i$	n_{e_i} (cm^{-3})
10^9	0	4.5	50	6.05	11.09	0.166	3.79×10^{11}
	0.1	4.2	50	5.63	10.09	0.170	3.85×10^{11}
	0.5	3.4	50	4.52	7.399	0.185	3.96×10^{11}
	1	2.8	30	3.77	3.329	0.192	2.54×10^{11}
	2	2.3	20	3.00	1.480	0.209	1.53×10^{11}
	5	1.7	20	2.25	0.7399	0.199	1.47×10^{11}
	10	1.5	20	1.91	0.4036	0.205	1.00×10^{11}
10^{10}	0	1.5	20	1.94	4.439	0.195	1.16×10^{12}
	0.1	1.5	20	1.90	4.036	0.206	9.96×10^{11}

equations (2.41) and (2.42). I define a value for $\left(\dot{M}/\dot{M}_E\right)$ that is as small as possible such that $\left(\dot{M}/\dot{M}_E\right) \gg \frac{1}{2}x_c$, the condition shown in equation (2.59). I then obtain the mass outflow rate $\dot{M}$ using equation (2.60), and hence the initial particle density n_{e_i} using equation (2.47). Figures 2.6 and 2.7 show the values chosen for $\left(\dot{M}/\dot{M}_E\right)$ with the corresponding $\dot{M}$. The dashed line shows $\dot{M} = \frac{1}{2}x_c\dot{M}_E$, which is the lowest limit for $\dot{M}$ such that the trapping radius $x_t > x_c$.

Using the initial conditions and the temperature function $f(y)$ evaluated during the spectral evolution computations I then compute $\tilde{u}(x)$, $y(x)$, $T_e(x)$ and $n_e(x)$ which are required to obtain the emergent spectrum.

The dynamic results are illustrated graphically in figures 2.8 to 2.13 which show $\tilde{u}(x)$, $y(x)$, $T_e(x)$ and $n_e(x)$.

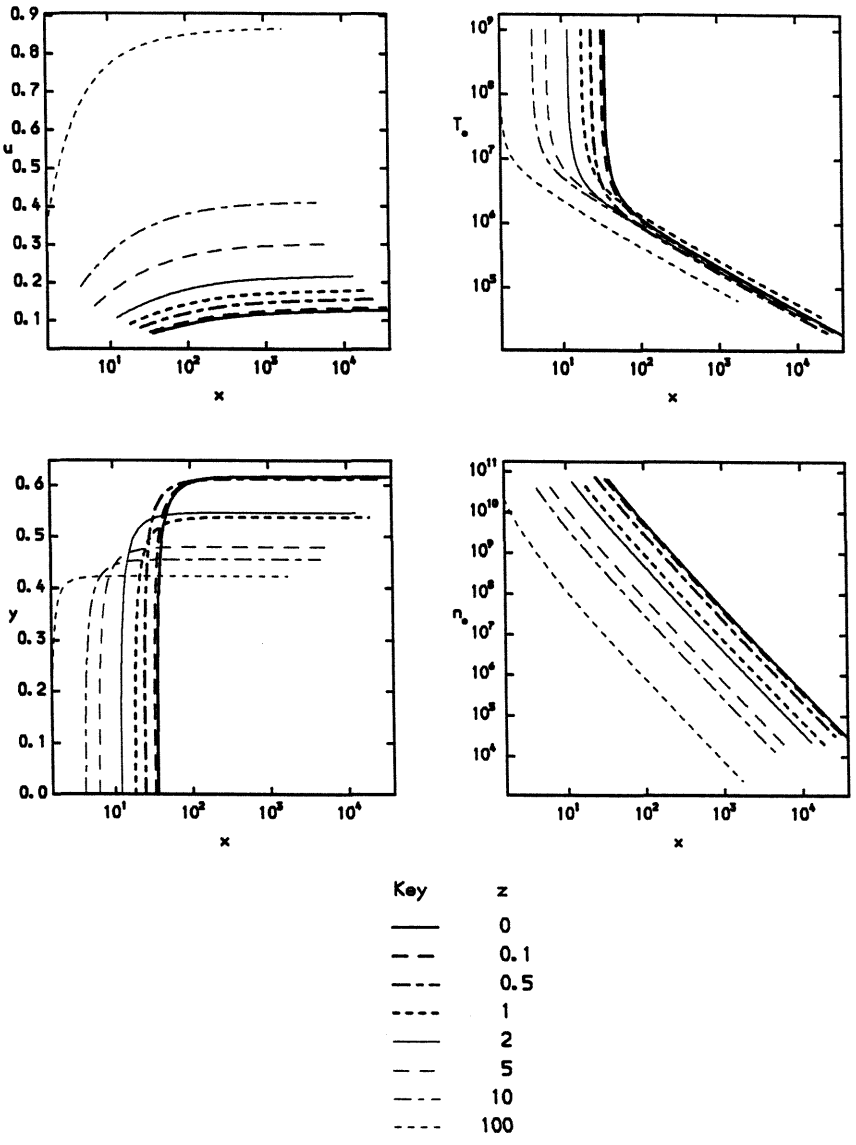

Figure 2.8: Case A dynamics showing $u(x)$, $y(x)$, $T_e(x)$ and $n_e(x)$, for $T_{e_i} = 10^9$ and z as shown.

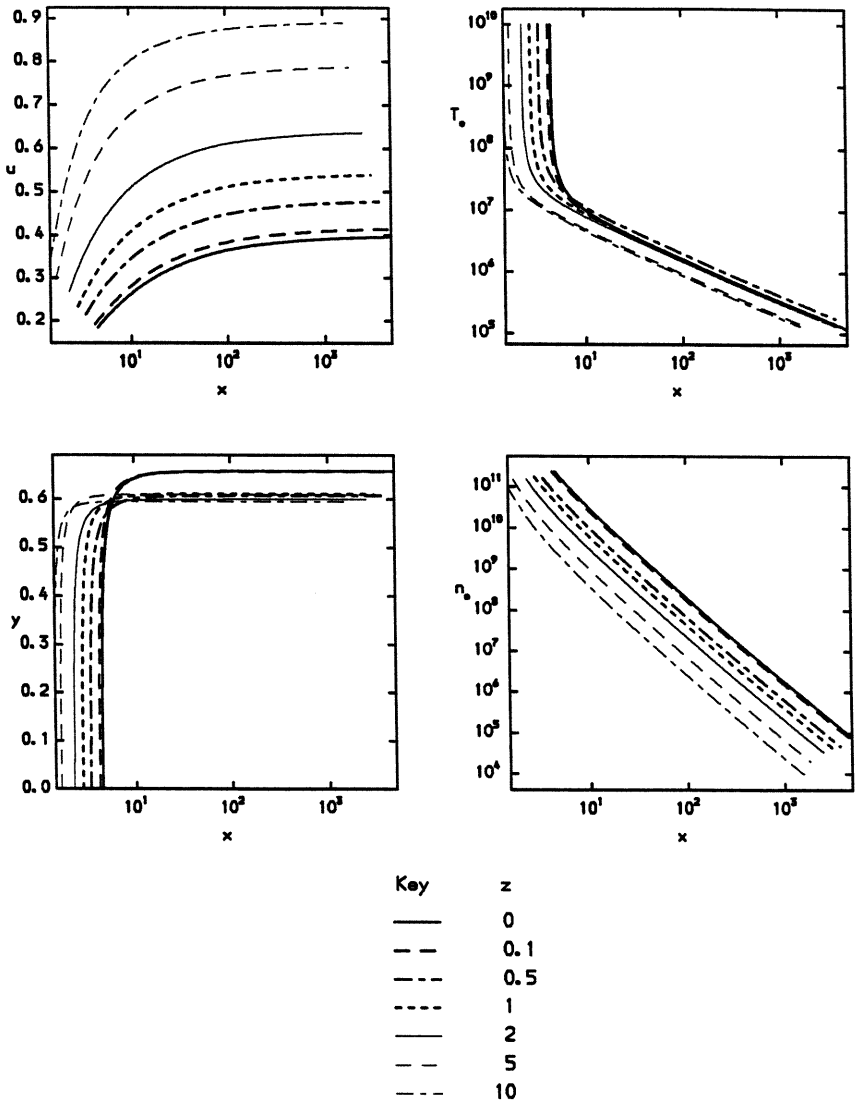

Figure 2.9: Case A dynamics showing $u(x)$, $y(x)$, $T_e(x)$ and $n_e(x)$, for $T_{e_i} = 10^{10}$ and z as shown.

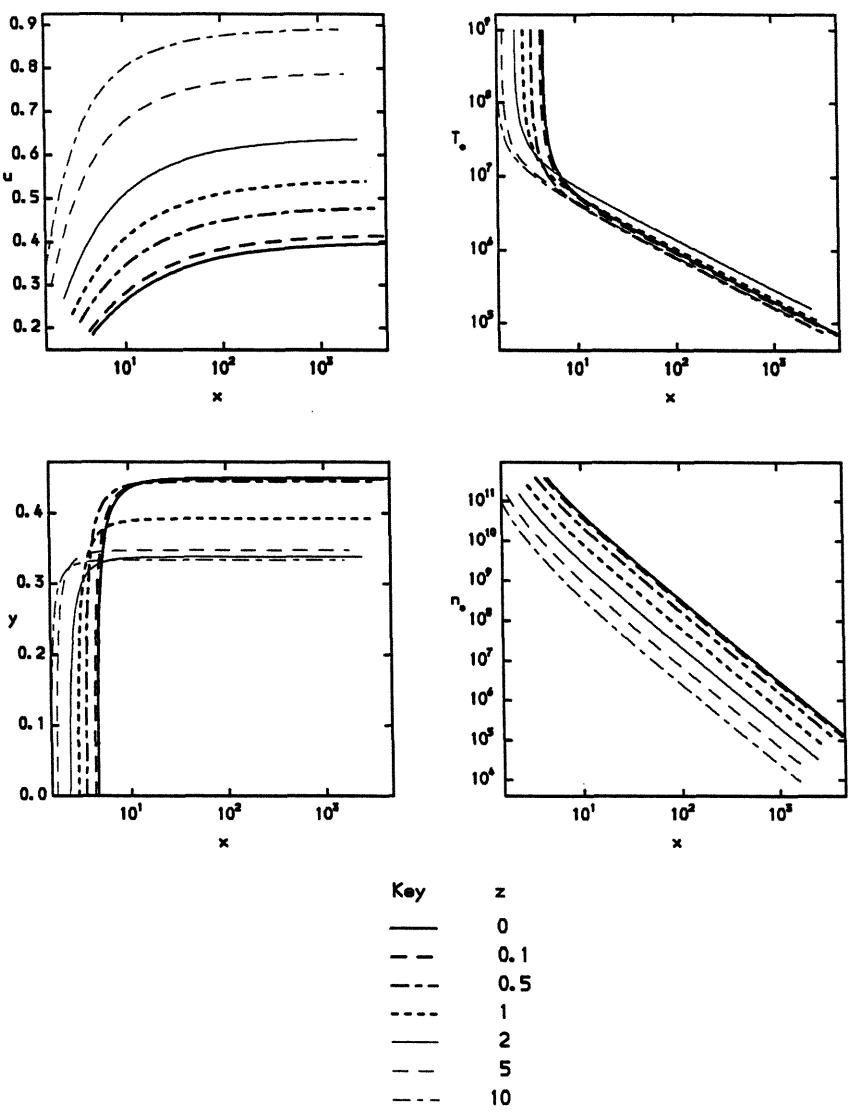

Figure 2.10: Case B dynamics showing $u(x)$, $y(x)$, $T_e(x)$ and $n_e(x)$, for $T_{e_i} = 10^9$ and z as shown.

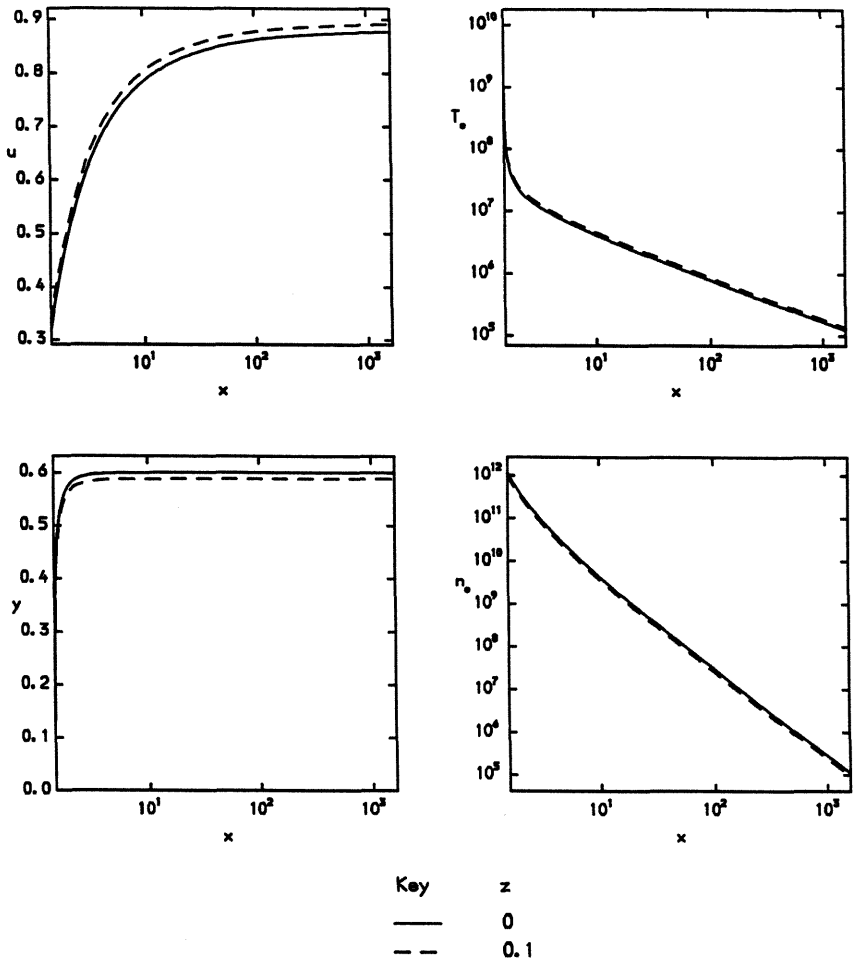

Figure 2.11: Case B dynamics showing $u(x)$, $y(x)$, $T_e(x)$ and $n_e(x)$, for $T_{e_i} = 10^{10}$ and z as shown.

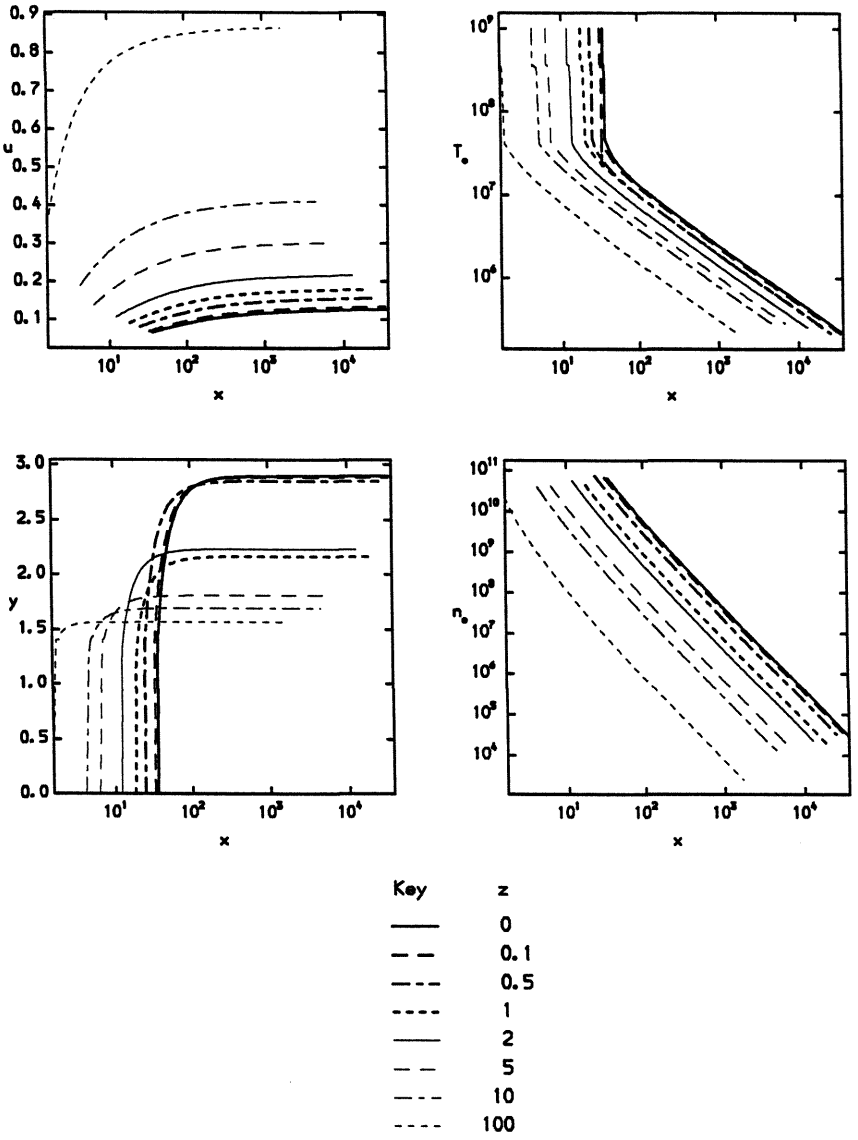

Figure 2.12: Case C dynamics showing $u(x)$, $y(x)$, $T_e(x)$ and $n_e(x)$, for $T_{e_i} = 10^9$ and z as shown.

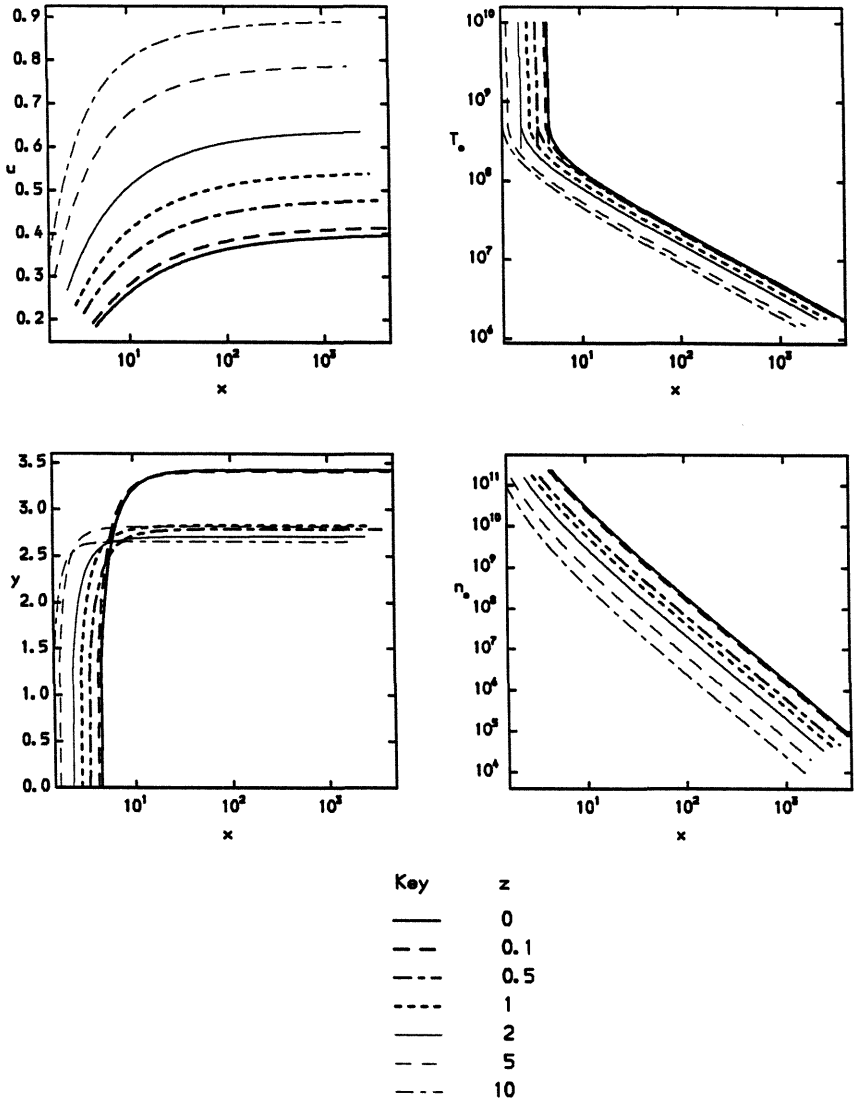

Figure 2.13: Case C dynamics showing $u(x)$, $y(x)$, $T_e(x)$ and $n_e(x)$, for $T_{e_i} = 10^{10}$ and z as shown.

2.7 Observable Spectra

The emergent spectrum can be described by the specific luminosity measured by an observer at infinity. This is given by Becker and Begelman (1986b) equation (4.6)

$$L_\nu(\nu) = \frac{32h\pi^2 r_p^2}{c^2}\left(\frac{1-u_\infty}{1+u_\infty}\right)\nu^3\bar{n}\left[\tilde{\chi}\left(\frac{1-u_\infty}{1+u_\infty}\right)^{\frac{1}{2}}, r_p\right], \tag{2.80}$$

where $\tilde{\chi} \equiv h\nu/kT_e(r_\beta)$; r_p is the photospheric radius, r_β is the Comptonization radius (beyond which Compton scattering has little effect on the spectrum) and u_∞ is the dimensionless flow velocity measured by a observer at infinity, who is stationary with respect to the metric,

$$u_\infty = \frac{\tilde{u}}{(1+\tilde{u}^2)^{1/2}}. \tag{2.81}$$

Becker and Begelman (1986a) describe how the spectrum evolves from r_β to r_p, which they call the diffusive regime. The spectral evolution in this region is minimal, so I make the simple approximation that the spectrum does not evolve beyond r_β, i.e. $\bar{n}(\chi, r_p) = \bar{n}(\chi, r_\beta)$. The Comptonization radius is where $y(r_\beta) \rightarrow y_\infty$, so I take r_β to be the point at which $y = y_\infty \times 0.99$.

The photospheric radius is evaluated from Becker and Begelman (1986a) equations (5.11) and (5.12)

$$\frac{e^{q_p} - \frac{1}{2}q_p^2 - 1}{e^{q_p} - q_p - 1} = -u_\infty, \tag{2.82}$$

where

$$q_p \equiv -\frac{3r_t}{r_p}. \tag{2.83}$$

Equation (2.82) is solved for q_p using the HYBRD non-linear equation solving method (Garbow *et al.*, 1980). Then equation (2.83) gives r_p in terms of r_t, the trapping radius, where

$$r_t \equiv \frac{r_g}{2}\frac{\dot{M}}{\dot{M}_E}, \tag{2.84}$$

which leaves

$$r_p = -\frac{3r_g}{2q_p}\frac{\dot{M}}{\dot{M}_E}. \tag{2.85}$$

The specific luminosity defined in equation (2.80) is written in terms of $\bar{n}(\chi, r)$ and ν. I have calculated the spectra $N(\chi, y)$, from an arbitrary initial spectrum $N(\chi, 0)$. From equation (2.62) the real spectrum can be written

$$\bar{n}(\chi, r) = \mathcal{A}N(\chi, y(r))\chi^{-2}f^{-3}(y) \tag{2.86}$$

Table 2.3: Results for Case A

$U_{r_i}/U_{e_i} = 100$

T_{e_i} (K)	z	y_∞	u_∞	$T_e(x_\beta)$ (K)	$n_e(x_\beta)$	x_p	$\sigma n_e x_p r_g$
10^9	0	0.616	0.128	9.26×10^5	3.02×10^9	805	
	0.1	0.616	0.134	9.32×10^5	3.13×10^9	768	0.94
	0.5	0.612	0.157	9.55×10^5	3.47×10^9	659	0.71
	1	0.538	0.189	1.72×10^6	1.78×10^9	276	0.57
	2	0.547	0.219	1.65×10^6	2.52×10^9	240	0.33
	5	0.480	0.304	2.82×10^6	1.66×10^9	87.6	0.18
	10	0.456	0.414	3.55×10^6	1.64×10^9	65.7	0.09
	100	0.423	0.869	5.43×10^6	1.39×10^9	33.3	0.01
10^{10}	0	0.657	0.398	6.87×10^6	1.27×10^{10}	40.8	
	0.1	0.656	0.417	6.87×10^6	1.26×10^{10}	39.2	0.99
	0.5	0.607	0.481	1.08×10^7	9.22×10^9	22.9	0.77
	1	0.610	0.543	1.06×10^7	1.03×10^{10}	20.4	0.50
	2	0.599	0.638	1.17×10^7	9.48×10^9	17.6	0.30
	5	0.609	0.791	1.18×10^7	1.20×10^{10}	14.5	0.12
	10	0.594	0.891	1.40×10^7	9.27×10^9	13.0	0.05

Table 2.4: Results for Case B

$U_{r_i}/U_{e_i} = 1000$

T_{e_i} (K)	z	y_∞	u_∞	$T_e(x_\beta)$ (K)	$n_e(x_\beta)$	x_p	$\sigma n_e x_p r_g$
10^9	0	0.450	0.398	3.46×10^6	1.43×10^{10}	68.1	
	0.1	0.449	0.417	3.64×10^6	1.62×10^{10}	65.3	1.16
	0.5	0.445	0.480	3.62×10^6	1.54×10^{10}	57.2	0.59
	1	0.392	0.543	5.82×10^6	1.02×10^{10}	30.7	0.48
	2	0.338	0.638	9.37×10^6	6.23×10^9	17.6	0.30
	5	0.348	0.791	9.30×10^6	7.55×10^9	14.5	0.12
	10	0.334	0.891	1.08×10^7	5.59×10^9	13.0	0.05
10^{10}	0	0.600	0.882	1.28×10^7	1.07×10^{11}	13.1	
	0.1	0.588	0.894	1.42×10^7	9.22×10^{10}	13.0	0.53

where $\mathcal{A}$ is a normalisation calculated as follows: the initial radiation energy density is, from equation (2.10),

$$U_{r_i} = \frac{8\pi(kT_{e_i})^4}{(ch)^3} \int_0^\infty \chi^3 \bar{n}(\chi, 0) d\chi, \tag{2.87}$$

or, since $f(0) = 1$,

$$U_{r_i} = \frac{8\pi(kT_{e_i})^4}{(ch)^3} \int_0^\infty \mathcal{A}\chi N(\chi, 0) d\chi. \tag{2.88}$$

Now, U_{r_i}/U_{e_i} is a parameter to the problem, and U_{e_i} can be written as

$$U_{e_i} = \frac{3}{2} n_{e_i} k T_{e_i}, \tag{2.89}$$

so the normalisation may be written

$$\mathcal{A} = \left(\frac{U_{r_i}}{U_{e_i}}\right) \frac{\frac{3}{2} n_{e_i} k T_{e_i}}{\frac{8\pi(kT_{e_i})^4}{(ch)^3} \int_0^\infty \chi N(\chi, 0) d\chi}. \tag{2.90}$$

Thus the specific luminosity in terms of $N(\chi, y)$ is

$$L_\nu = \frac{32k^3\pi^2}{h^2c^2} r_p^2 \left(\frac{1-u_\infty}{1+u_\infty}\right) \chi(r_\beta) \left(\frac{T_e(r_\beta)}{f(r_\beta)}\right)^3 \mathcal{A} N \left[\tilde{\chi}\left(\frac{1-u_\infty}{1+u_\infty}\right)^{\frac{1}{2}}, y(r_\beta)\right]. \tag{2.91}$$

Values for y_∞, u_∞, $T_e(x_\beta)$ and x_p are obtained from tables 2.3, 2.4 and 2.5. Figures 2.14 to 2.19 show L_ν for the several cases.

Table 2.5: Results for Case C

$U_{r_i}/U_{e_i} = 100$

T_{e_i} (K)	z	y_∞	u_∞	$T_e(x_\beta)$ (K)	$n_e(x_\beta)$	x_p	$\sigma n_e x_p r_g$
10^9	0	2.896	0.128	7.33×10^6	1.11×10^9	805	
	0.1	2.886	0.134	7.35×10^6	1.15×10^9	768	0.94
	0.5	2.850	0.157	7.40×10^6	1.27×10^9	659	0.71
	1	2.162	0.189	9.88×10^6	9.48×10^8	276	0.57
	2	2.230	0.219	9.51×10^6	1.18×10^9	240	0.33
	5	1.807	0.304	1.27×10^7	1.28×10^9	87.6	0.18
	10	1.694	0.414	1.42×10^7	1.43×10^9	65.7	0.09
	100	1.567	0.869	1.80×10^7	1.39×10^9	33.3	0.01
10^{10}	0	3.428	0.398	6.71×10^7	4.50×10^9	40.8	
	0.1	3.441	0.417	6.68×10^7	4.46×10^9	39.2	0.99
	0.5	2.787	0.481	8.33×10^7	3.65×10^9	22.9	0.68
	1	2.826	0.543	8.30×10^7	4.00×10^9	20.4	0.50
	2	2.706	0.638	8.98×10^7	4.13×10^9	17.6	0.30
	5	2.817	0.791	9.28×10^7	4.83×10^9	14.5	0.12
	10	2.656	0.891	1.10×10^8	4.75×10^9	13.0	0.05

Tables 2.6, 2.7 and 2.8 show the distribution of the energy transport between the gas and the radiation: $\dot{E}_{bulk}$ is the energy transported radially by the gas, including thermal and bulk kinetic energy, and is shown at the injection radius and at the photospheric radius; $L(r_i)$ is the radiation luminosity in ergs s^{-1} at the injection radius and L_∞ is the luminosity observed at infinity, evaluated by integrating equation (2.91).

There are several points to note in these results. The final velocity of the outflow is a large fraction of the speed of light (although still non-relativistic). In most cases, the initial velocity of the outflow is less than the escape velocity, and so the wind is driven by the radiative processes. There is very little transfer of energy between the radiation and the matter. This differs from the conclusions reached by Flammang (1982) because the wind is only slightly supercritical (since I have defined a wind where the mass loss $\sim 1M_\odot$ yr^{-1} and where the supercriticality is due to the number of $e^\pm$-pairs present) and also because Flammang deals with an optically thick system in thermal equilibrium.

Tables 2.3, 2.4 and 2.5 also show the ratio of the flow time to the pair annihilation time. I estimate the pair annihilation time as $v_{esc}/\sigma_T n_e$ and the flow time as v_{esc}/r_p, so the ratio of the flow time to the annihilation time is $\sigma_T n_e r_p$. In most cases this is less than unity and so it is consistent to neglect the annihilation of pairs.

Thus I conclude that an optically thick, supercritical, pair wind is compatible with a power law spectral slope with a cut-off, determined by the dynamics of the outflow, in the hard X-ray region.

X-ray variablility over $\sim 10^5$ s has been observed in many sources, which indicates a photospheric radius of $\sim 100r_g$. Tables 2.3, 2.4 and 2.5 shows that one or more of the following is required to meet this constraint: a high initial electron temperature ($T_{e_i} = 10^{10}$ K), a high proportion of electron-positron pairs ($z \geq 5$) or highly radiation dominated flow ($U_{r_i}/U_{e_i} = 1000$). Cross referencing with tables 2.1 and 2.2 shows that the mass outflow rate $\dot{M} < 10M_\odot yr^{-1}$, but the presence of pairs in most cases makes this outflow highly supercritical.

2.8 Problems Associated with the Model

I have calculated the evolution of the spectrum using the Kompaneets equation, which is only valid when the transfer of energy as a result of a collision between a photon and an electron

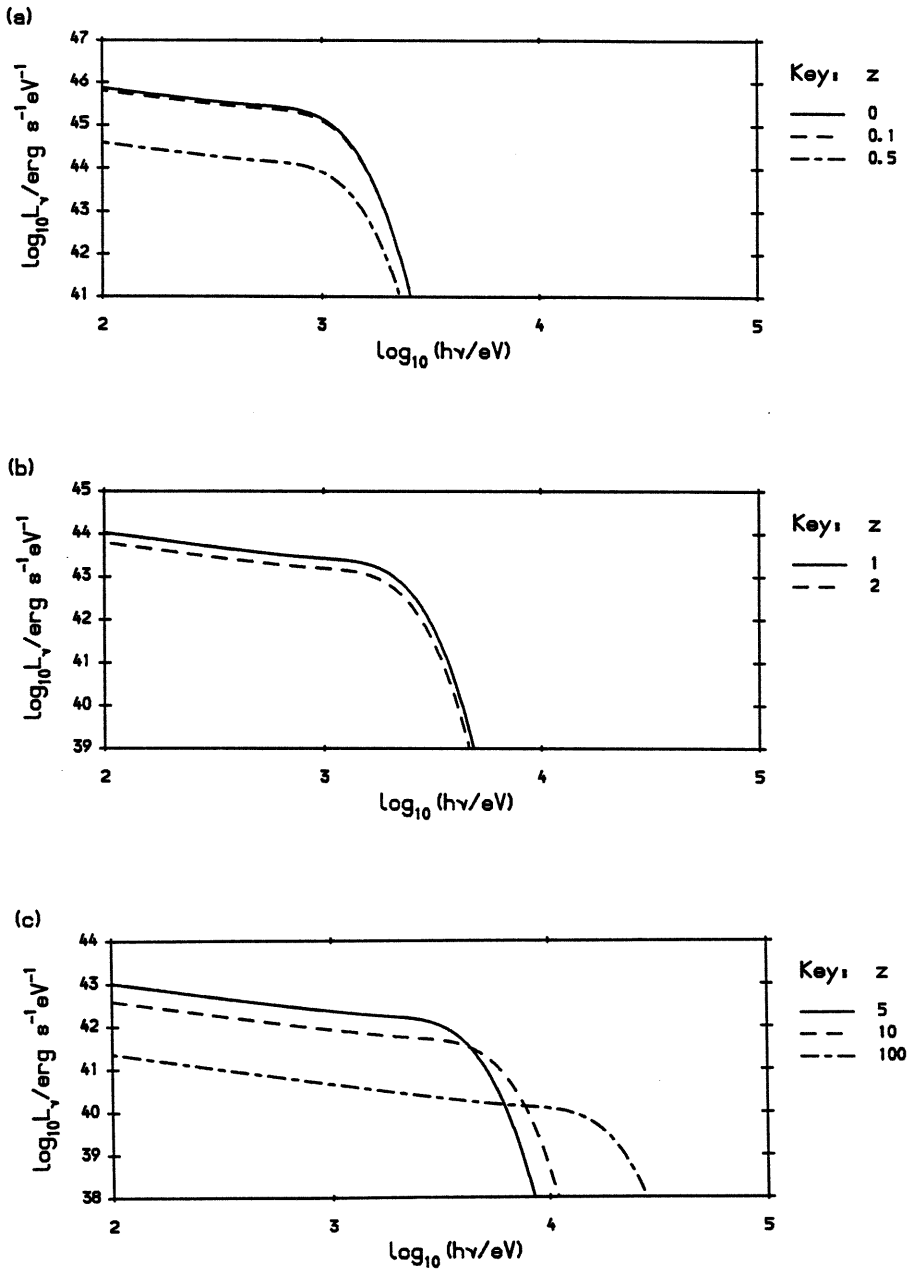

Figure 2.14: Observable spectra for case A, $T_{e_i} = 10^9$, (a) $\dot{M}/\dot{M}_E = 200$, (b) $\dot{M}/\dot{M}_E = 100$, (c) $\dot{M}/\dot{M}_E = 50$.

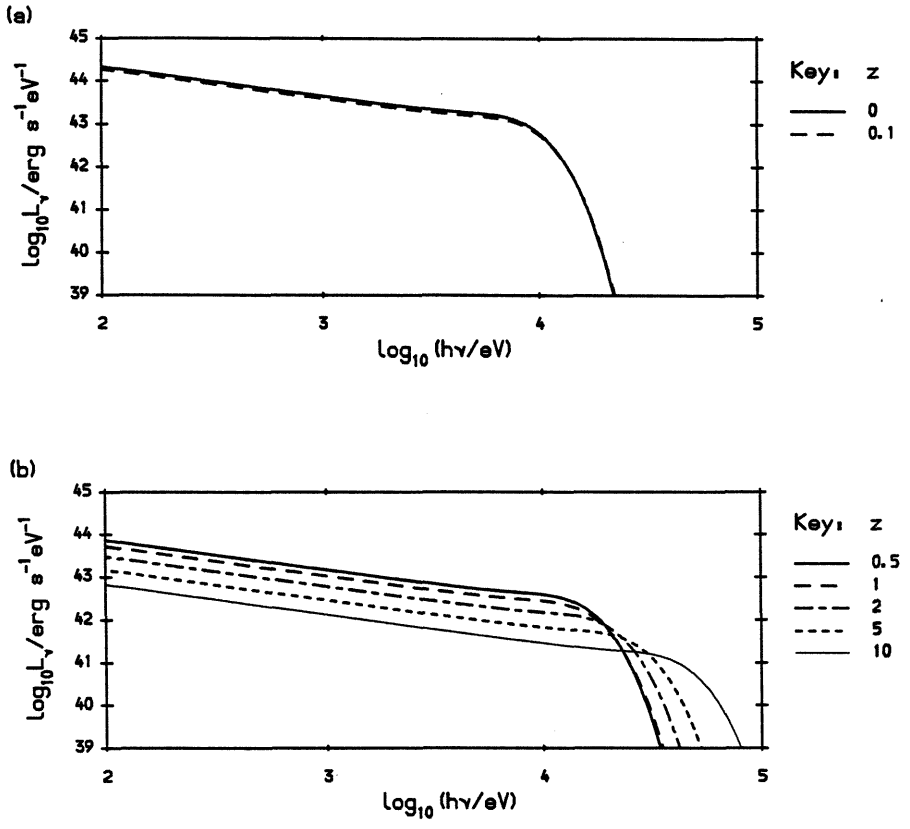

Figure 2.15: Observable spectra for case A, $T_{e_i} = 10^{10}$, (a) $\dot{M}/\dot{M}_E = 30$, (b) $\dot{M}/\dot{M}_E = 20$.

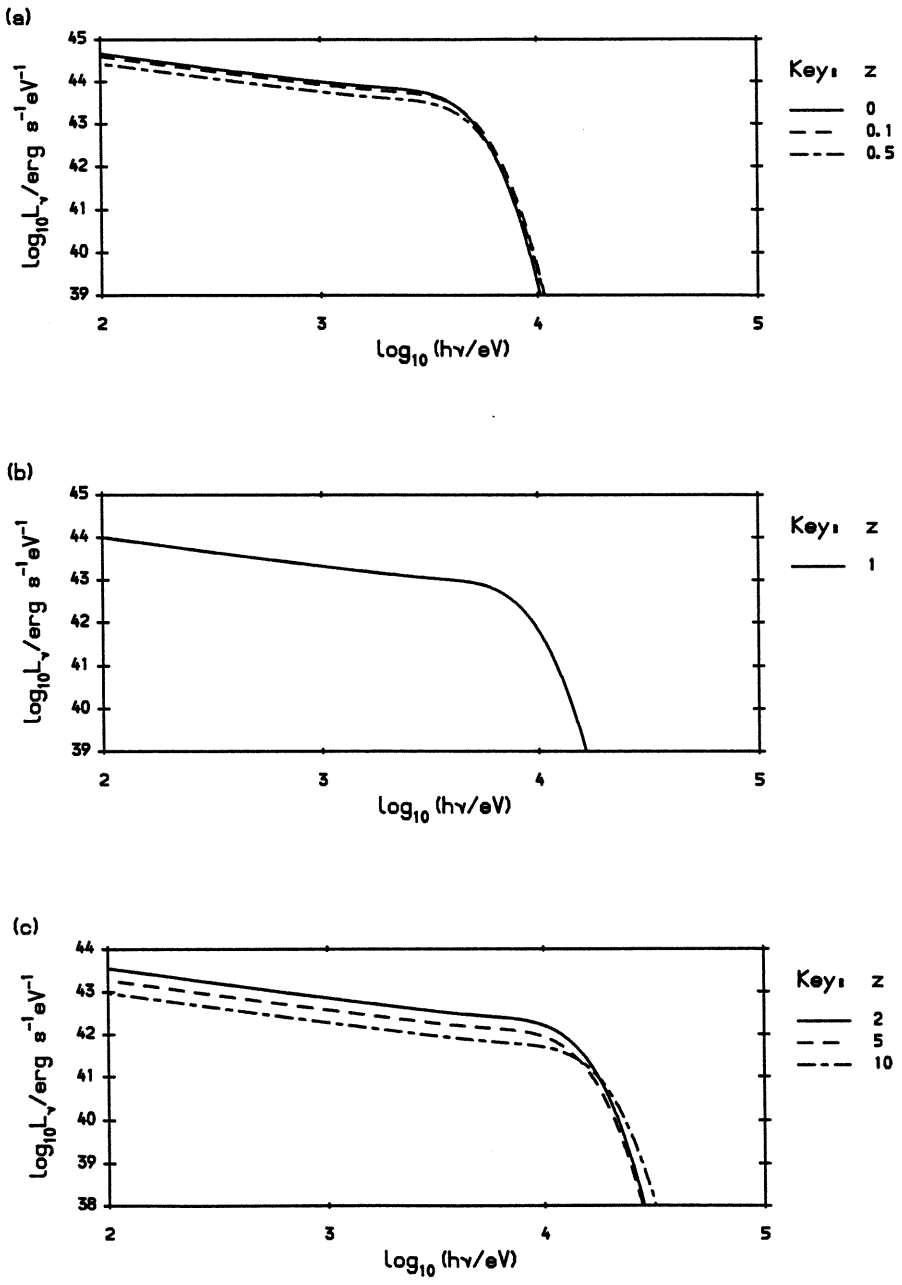

Figure 2.16: Observable spectra for case B, $T_{e_i} = 10^9$, (a) $\dot{M}/\dot{M}_E = 50$, (b) $\dot{M}/\dot{M}_E = 30$, (c) $\dot{M}/\dot{M}_E = 20$.

Table 2.6: Energy transport in Case A, ergs s^{-1}

T_{e_i} (K)	z	$\dot{E}_{bulk}(r_i)$	$L(r_i)$	$\dot{E}_{bulk}(r_p)$	L_∞
10^9	0	3.19×10^{46}	5.52×10^{48}	8.77×10^{45}	5.55×10^{48}
	0.1	2.90×10^{46}	4.78×10^{48}	7.73×10^{45}	4.80×10^{48}
	0.5	2.15×10^{45}	3.01×10^{47}	6.03×10^{45}	2.97×10^{47}
	1	7.79×10^{44}	1.01×10^{47}	2.04×10^{45}	9.93×10^{46}
	2	4.92×10^{44}	5.81×10^{46}	1.31×10^{45}	5.72×10^{46}
	5	1.09×10^{44}	1.16×10^{46}	3.21×10^{44}	1.14×10^{46}
	10	6.30×10^{43}	4.83×10^{45}	1.78×10^{44}	4.72×10^{45}
	100	4.28×10^{42}	3.92×10^{44}	6.41×10^{42}	3.90×10^{44}
10^{10}	0	4.33×10^{45}	3.24×10^{47}	1.07×10^{46}	3.18×10^{47}
	0.1	3.85×10^{45}	2.86×10^{47}	1.02×10^{46}	2.80×10^{47}
	0.5	1.82×10^{45}	1.28×10^{47}	4.69×10^{45}	1.25×10^{47}
	1	1.28×10^{45}	9.31×10^{46}	3.15×10^{45}	9.12×10^{46}
	2	8.13×10^{44}	5.68×10^{46}	1.88×10^{45}	5.58×10^{46}
	5	3.23×10^{44}	2.98×10^{46}	6.51×10^{44}	2.95×10^{46}
	10	1.51×10^{44}	1.58×10^{46}	1.27×10^{44}	1.58×10^{46}

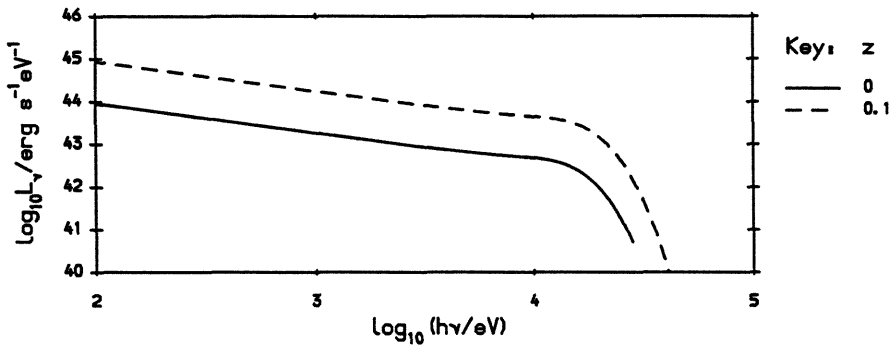

Figure 2.17: Observable spectra for case B, $T_{e_i} = 10^{10}$, $\dot{M}/\dot{M}_E = 30$.

Table 2.7: Energy transport in Case B, ergs s^{-1}

T_{e_i} (K)	z	$\dot{E}_{bulk}(r_i)$	$L(r_i)$	$\dot{E}_{bulk}(r_p)$	L_∞
10^9	0	6.29×10^{45}	5.39×10^{47}	1.89×10^{46}	5.26×10^{47}
	0.1	5.59×10^{45}	4.77×10^{47}	2.29×10^{46}	4.60×10^{47}
	0.5	3.94×10^{45}	3.22×10^{47}	1.19×10^{46}	3.14×10^{47}
	1	1.64×10^{45}	1.40×10^{47}	5.07×10^{45}	1.36×10^{47}
	2	6.76×10^{44}	5.68×10^{46}	1.89×10^{45}	5.56×10^{46}
	5	2.43×10^{44}	2.98×10^{46}	6.50×10^{44}	2.94×10^{46}
	10	1.03×10^{44}	1.58×10^{46}	2.20×10^{44}	1.57×10^{46}
10^{10}	0	1.15×10^{45}	1.83×10^{47}	2.69×10^{46}	1.58×10^{47}
	0.1	1.04×10^{46}	1.57×10^{48}	2.20×10^{46}	1.56×10^{48}

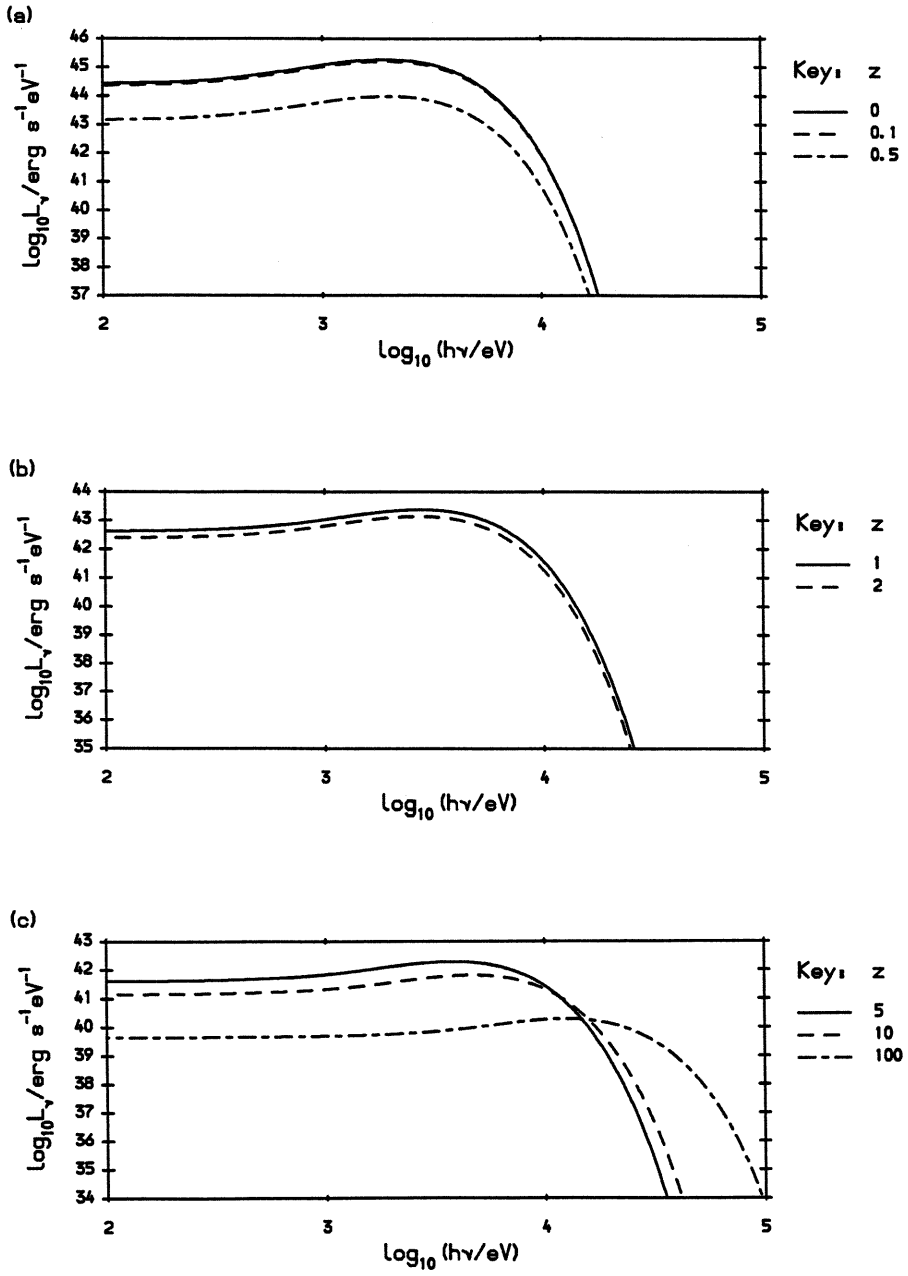

Figure 2.18: Observable spectra for case C, $T_{e_i} = 10^9$, (a) $\dot{M}/\dot{M}_E = 200$, (b) $\dot{M}/\dot{M}_E = 100$, (c) $\dot{M}/\dot{M}_E = 50$.

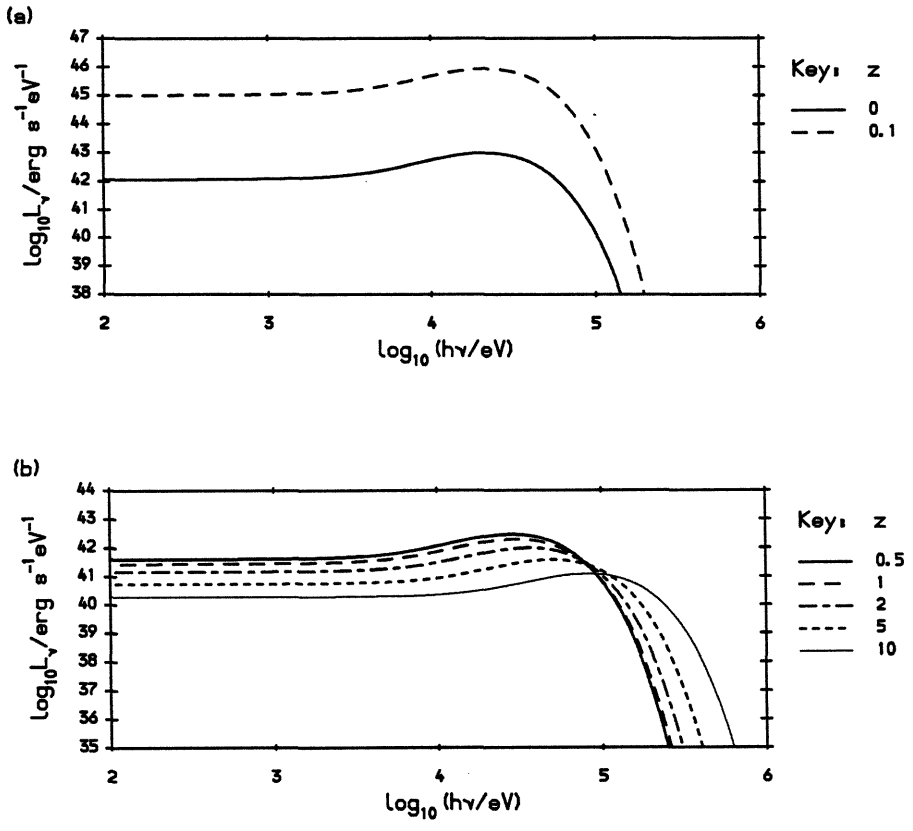

Figure 2.19: Observable spectra for case C, $T_{e_i} = 10^{10}$, (a) $\dot{M}/\dot{M}_E = 30$, (b) $\dot{M}/\dot{M}_E = 20$.

Table 2.8: Energy transport in Case C, ergs s^{-1}

T_{e_i} (K)	z	$\dot{E}_{bulk}(r_i)$	$L(r_i)$	$\dot{E}_{bulk}(r_p)$	L_∞
10^9	0	3.19×10^{46}	5.52×10^{48}	2.30×10^{46}	5.53×10^{48}
	0.1	2.90×10^{46}	4.78×10^{48}	7.73×10^{45}	4.80×10^{48}
	0.5	2.15×10^{45}	3.01×10^{47}	6.04×10^{45}	2.97×10^{47}
	1	7.79×10^{44}	1.01×10^{47}	2.04×10^{45}	9.93×10^{46}
	2	4.92×10^{44}	5.81×10^{46}	1.31×10^{45}	5.72×10^{46}
	5	1.09×10^{44}	1.16×10^{46}	3.21×10^{44}	1.14×10^{46}
	10	6.30×10^{43}	4.83×10^{45}	1.79×10^{44}	4.72×10^{45}
	100	4.28×10^{42}	3.92×10^{44}	6.42×10^{42}	3.90×10^{44}
10^{10}	0	4.33×10^{45}	3.24×10^{47}	1.07×10^{46}	3.19×10^{47}
	0.1	3.85×10^{45}	2.86×10^{47}	1.02×10^{46}	2.80×10^{47}
	0.5	1.82×10^{45}	1.28×10^{47}	4.23×10^{45}	1.26×10^{47}
	1	1.28×10^{45}	9.31×10^{46}	3.15×10^{45}	9.12×10^{46}
	2	8.13×10^{44}	5.68×10^{46}	1.89×10^{45}	5.58×10^{46}
	5	3.23×10^{44}	2.98×10^{46}	6.51×10^{44}	2.95×10^{46}
	10	1.51×10^{44}	1.58×10^{46}	2.20×10^{44}	1.57×10^{46}

is small when compared to the energy of the photon. However, when the photon energy is as high as the electron rest mass energy, this energy transfer is very large, the photon losing a significant part of its energy to the electron and the Kompaneets equation is not valid. I calculated the spectral evolution from initial spectra described by power laws with a cut-off at 1 MeV or higher, the electron rest mass energy is 511 KeV, so the high frequency end of my initial spectra are above the point at which the Kompaneets equation breaks down. This means that the high frequency end of the spectrum is calculated incorrectly. In addition, the dynamical evolution is dependant on the Compton temperature which should be calculated including relativistic effects. The results here cannot be relied upon unless this factor is taken into account

If I assume that the observed spectrum *is* as calculated, then because there are significant numbers of γ-ray photons the compactness parameter must be evaluated to estimate whether pair production is important. The compactness parameter is defined (Guilbert, Fabian and Rees, 1983)

$$l = \frac{\sigma_T L_\gamma}{m_e c^3 R}, \tag{2.92}$$

where L_γ is the γ-ray luminosity and R is the size of the region concerned. The calculated observed spectra can all be approximated by a power law with energy index between 0 and -1, so most of the energy is carried by the highest energy photons and I estimate the γ-ray luminosity to be the specific luminosity measured at the point the spectrum steepens. Note that for some observed spectra the maximum photon energies are less than 511 keV, but the initial spectra all include a significant portion of energy in photons above 511 keV, so I take the specific luminosity at the point where the spectrum steepens to be indicative of γ-ray luminosities at radii smaller than r_p. I evaluate the compactness assuming $R = r_p$ (the photospheric radius) and $R = r_i$ (the injection radius) using the same luminosity in each case. The results are summarised in tables 2.9, 2.10 and 2.11, where for $R = r_p$ the compactness parameter is negligible for $z \geq 0.5$ and for $R = r_i$ the it is negligible for $z \geq 2$. Thus pair production is important when z is small and the corresponding mass outflow rate is very large; as I increase z and decrease the mass outflow rate it is still important to consider pair production at small radii, but not throughout the whole region. In those regions where the compactness is high the effective electron density will be increased, the wind will be more highly supercritical and will tend to accelerate over a shorter distance to a higher velocity. This will feed back into the spectral evolution and the results cannot be relied upon; the effects of pair production must be included in a proper calculation. In addition, as a result of pair production, there will be a loss of γ-ray photons from the spectrum and the spectrum will steepen at a lower energy.

Table 2.9: Estimate of compactness for Case A

$U_{r_i}/U_{e_i} = 100$

T_{e_i} (K)	z	L_γ erg s^{-1}	x_p	l_p	x_i	l_i
10^9	0	2.5×10^{45}	805	2.8	35.	65.
	0.1	2.0×10^{45}	768	2.4	32.	57.
	0.5	1.3×10^{44}	659	0.18	24.	4.9
	1	2.0×10^{43}	276	0.066	18.	1.0
	2	1.3×10^{43}	240	0.049	12.	0.99
	5	1.6×10^{42}	87.6	0.016	6.3	0.23
	10	4.0×10^{41}	65.7	5.5×10^{-3}	4.2	0.087
	100	1.0×10^{40}	33.3	2.7×10^{-4}	1.6	5.7×10^{-3}
10^{10}	0	1.6×10^{43}	40.8	0.36	4.5	3.2
	0.1	1.3×10^{43}	39.2	0.30	4.2	2.8
	0.5	3.2×10^{42}	22.9	0.13	3.4	0.86
	1	2.0×10^{42}	20.4	0.089	2.8	0.65
	2	1.3×10^{42}	17.6	0.067	2.3	0.51
	5	5.0×10^{41}	14.5	0.031	1.7	0.27
	10	2.0×10^{41}	13.0	0.014	1.5	0.12

Table 2.10: Estimate of compactness for Case B

$U_{r_i}/U_{e_i} = 1000$

T_{e_i} (K)	z	L_γ erg s^{-1}	x_p	l_p	x_i	l_i
10^9	0	6.3×10^{43}	68.1	0.84	4.5	13.
	0.1	5.0×10^{43}	65.3	0.70	4.2	11.
	0.5	2.5×10^{43}	57.2	0.40	3.4	6.7
	1	7.9×10^{42}	30.7	0.23	2.8	2.3
	2	2.0×10^{42}	17.6	0.10	2.3	0.79
	5	1.3×10^{42}	14.5	0.082	1.7	0.70
	10	5.0×10^{41}	13.0	0.035	1.5	0.30
10^{10}	0	4.0×10^{43}	13.1	2.8	1.5	24.
	0.1	5.0×10^{42}	13.0	0.35	1.5	3.0

2.9 The Spectrum Emitted from the Side of a Cone

I have calculated the dynamics of a spherically symmetric wind and the emergent spectrum as observed at infinity. Now I consider the case where the wind is funneled into a cone and I evaluate the spectrum that emerges from the side of the cone. I assume that all the wind motion is radial, i.e. the wind material at the edge of the cone does not expand outwards in a non-radial direction, and that the physical state at the edge of the cone, at a distance r from the apex, is the same as the physical state at radius r from the centre of the spherically symmetric outflow. Therefore the dynamical results that I have already calculated still apply.

I assume that radiation is emitted from the side of the cone. The spectrum of the radiation emitted at a point on the cone will depend on the distance from the apex. An observer will see a spectrum made up of all the spectra emitted at different distances from the apex of the cone. Consider an annulus on the surface of the cone at a distance r from the apex. The surface area of that annulus is proportional to r, so the number of photons emitted from that annulus is proportional to r, i.e. the number of photons of frequency ν emitted from the surface of an annulus of width δr at a distance r from the apex is

$$\delta \bar{n}_o(\nu, r) = C \bar{n}_\nu(r) r \delta r, \tag{2.93}$$

where C is some constant that depends, among other things, on the opening angle of the cone.

Table 2.11: Estimate of compactness for Case C

$U_{r_i}/U_{e_i} = 100$

T_{e_i} (K)	z	L_γ erg s^{-1}	x_p	l_p	x_i	l_i
10^9	0	2.0×10^{45}	805	2.3	35.	52.
	0.1	1.6×10^{45}	768	1.9	32.	46.
	0.5	7.9×10^{43}	659	0.11	24.	3.0
	1	2.0×10^{43}	276	0.066	18.	1.0
	2	1.3×10^{43}	240	0.049	12.	0.99
	5	2.0×10^{42}	87.6	0.021	6.3	0.29
	10	5.0×10^{41}	65.7	6.9×10^{-3}	4.2	0.11
	100	2.0×10^{40}	33.3	5.5×10^{-4}	1.6	0.011
10^{10}	0	7.9×10^{45}	40.8	180	4.5	1600.
	0.1	1.0×10^{43}	39.2	0.23	4.2	2.2
	0.5	2.5×10^{42}	22.9	0.099	3.4	0.67
	1	1.6×10^{42}	20.4	0.071	2.8	0.52
	2	1.0×10^{42}	17.6	0.052	2.3	0.40
	5	4.0×10^{41}	14.5	0.025	1.7	0.21
	10	1.0×10^{41}	13.0	7.0×10^{-3}	1.5	0.061

Integrating equation (2.93) between $r = 0$ and $r = r_t$ gives the observed spectrum (since radiation is no longer trapped when $r > r_t$),

$$\bar{n}_o(\nu) = \mathcal{C} \int_0^{r_t} \bar{n}_\nu(r) r dr. \tag{2.94}$$

Figures 2.20 to 2.25 show the spectra produced by integrating (2.94) for various dynamical results.

I note that conical outflow introduces a curvature into the X-ray spectrum, reminiscent of BL Lac spectra. While a direct comparison is not possible, since the BL Lac systems are usually assumed to be relativistic in order to suppress excessive X-rays from Comptonisation of the radio emission, my results suggest that spectral curvature may be a consequence of Compton processing in a conical outflow. However, further investigation is beyond the scope of this thesis.

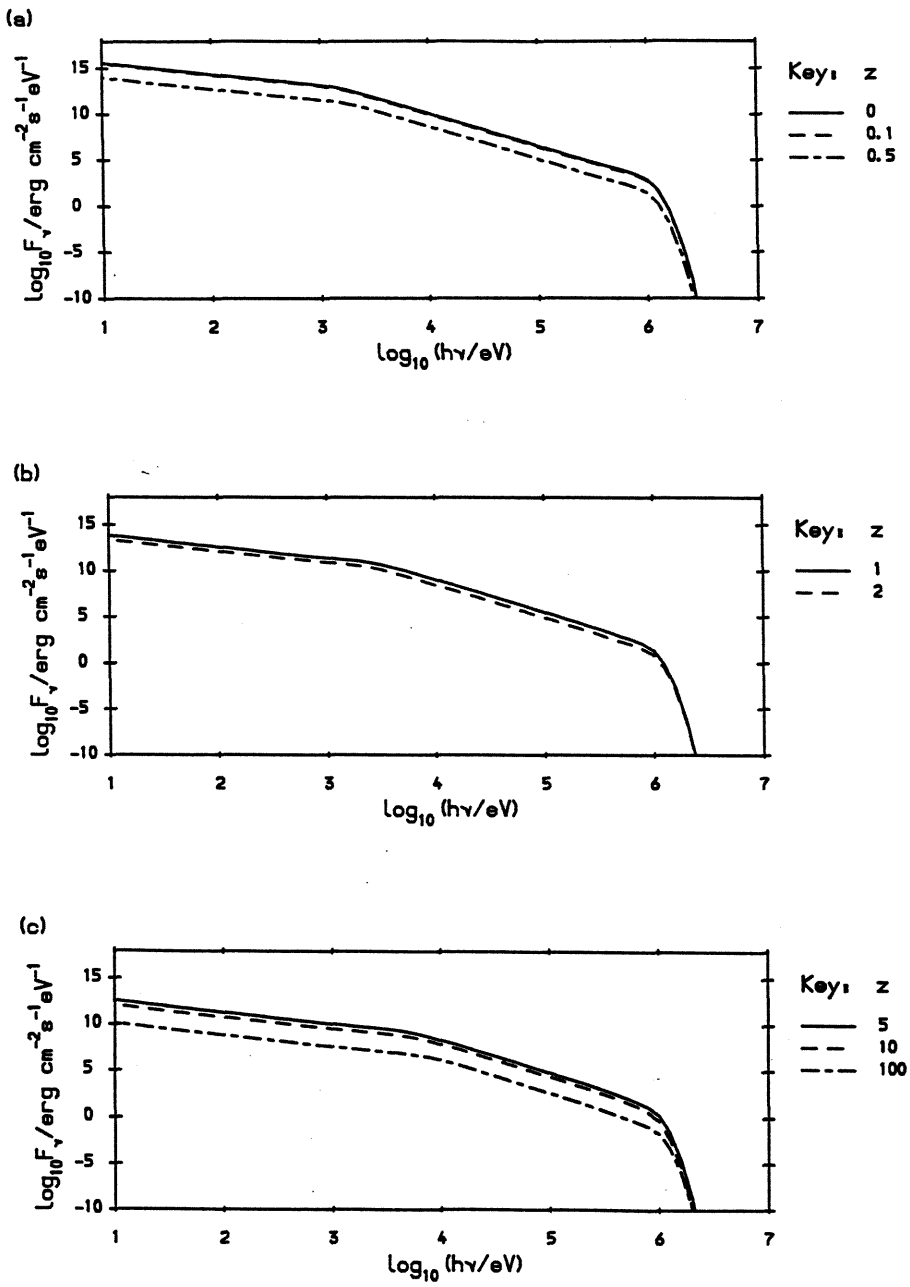

Figure 2.20: Spectra from the side of a cone, case A, $T_{e_i} = 10^9$, (a) $\dot{M}/\dot{M}_E = 200$, (b) $\dot{M}/\dot{M}_E = 100$, (c) $\dot{M}/\dot{M}_E = 50$.

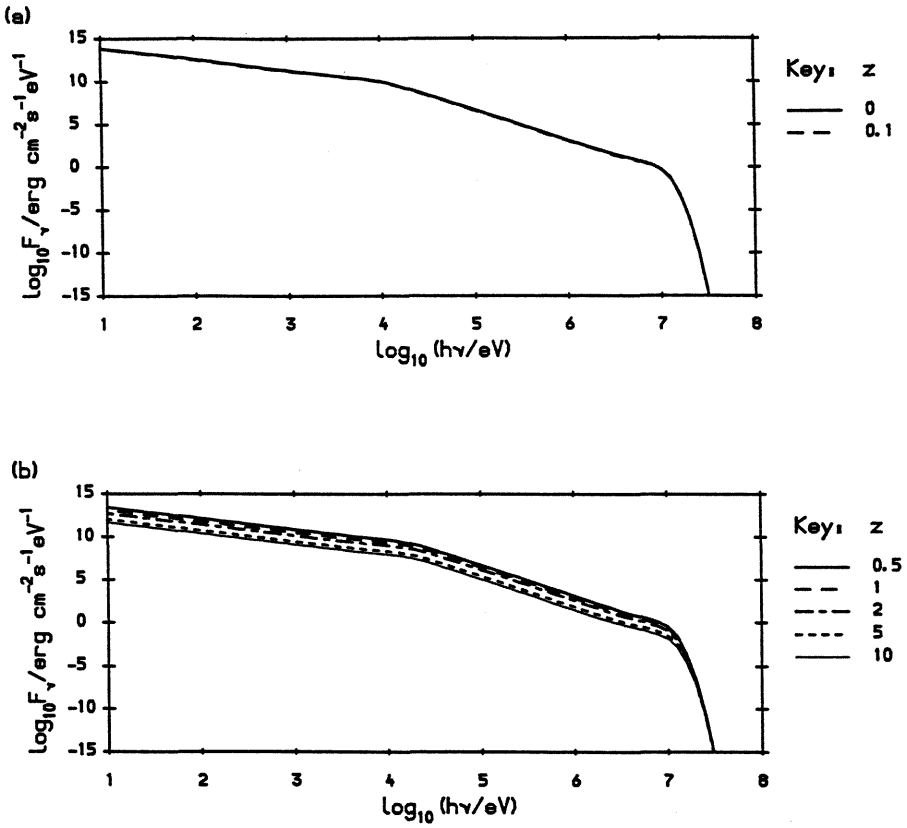

Figure 2.21: Spectra from the side of a cone, case A, $T_{e_i} = 10^{10}$, (a) $\dot{M}/\dot{M}_E = 30$, (b) $\dot{M}/\dot{M}_E = 20$.

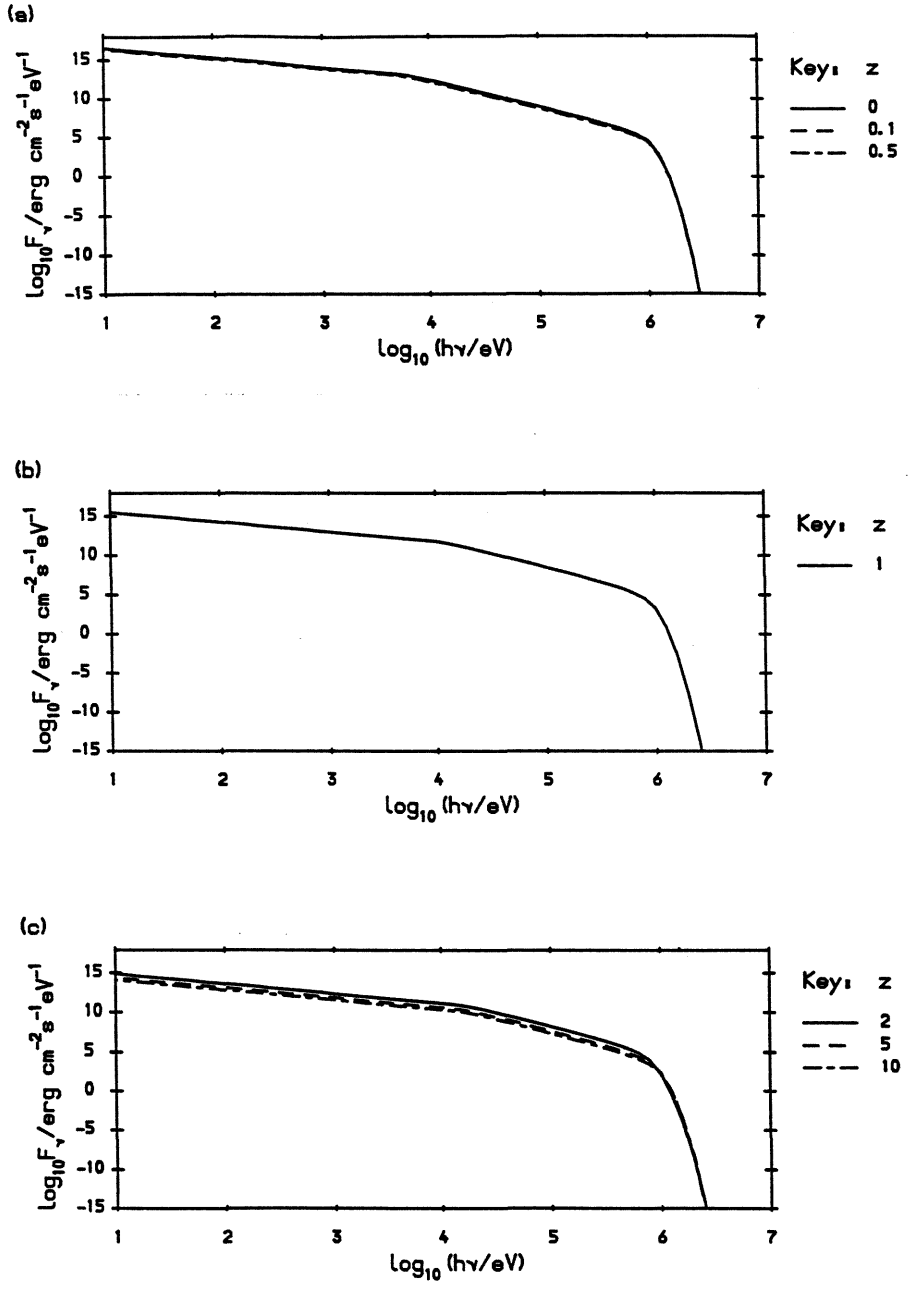

Figure 2.22: Spectra from the side of a cone, case B, $T_{e_i} = 10^9$, (a) $\dot{M}/\dot{M}_E = 50$, (b) $\dot{M}/\dot{M}_E = 30$, (c) $\dot{M}/\dot{M}_E = 20$.

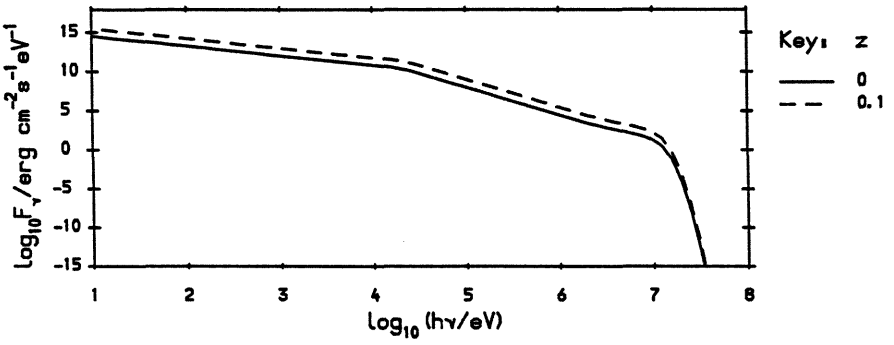

Figure 2.23: Spectra from the side of a cone, case B, $T_{e_i} = 10^{10}$, $\dot{M}/\dot{M}_E = 30$.

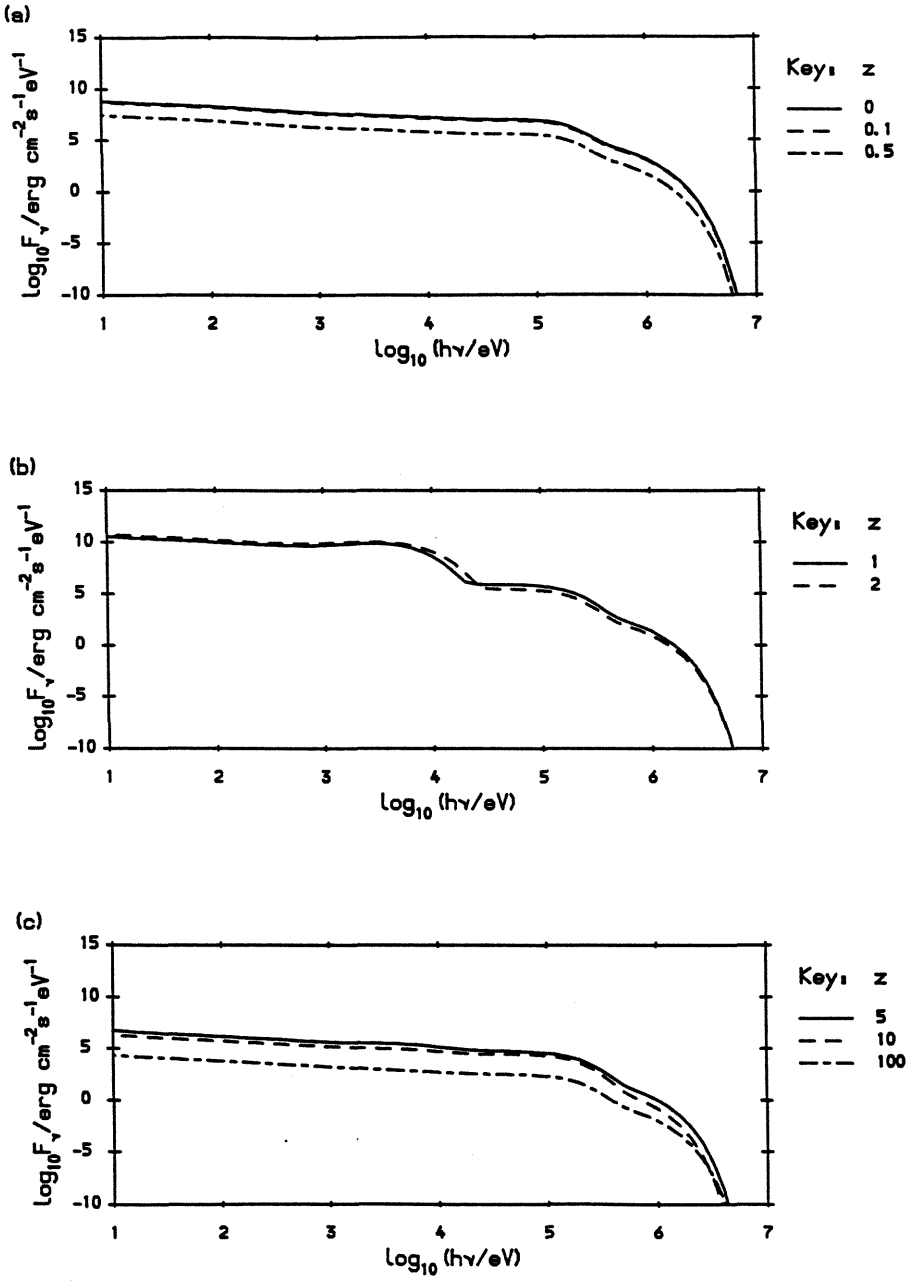

Figure 2.24: Spectra from the side of a cone, case C, $T_{e_i} = 10^9$, (a) $\dot{M}/\dot{M}_E = 200$, (b) $\dot{M}/\dot{M}_E = 100$, (c) $\dot{M}/\dot{M}_E = 50$.

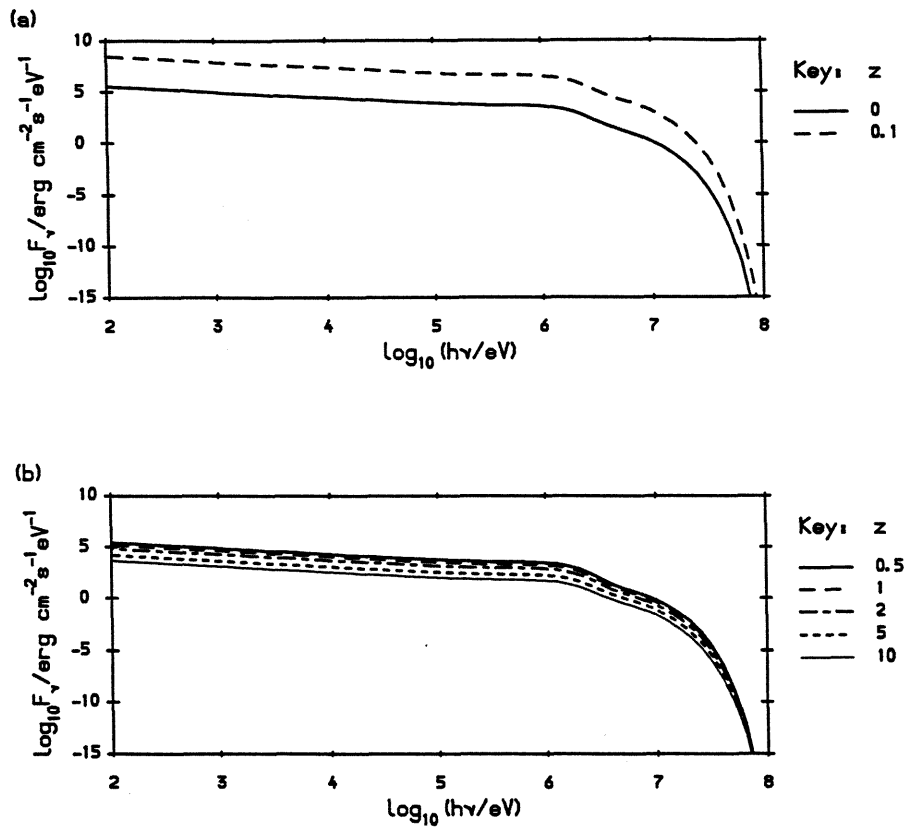

Figure 2.25: Spectra from the side of a cone, case C, $T_{e_i} = 10^{10}$, (a) $\dot{M}/\dot{M}_E = 30$, (b) $\dot{M}/\dot{M}_E = 20$.

Chapter 3

Two Phase Outflow as a Model for the Broad Line Region

3.1 Introduction

The "standard model" of the broad line region in active galaxies consists of clouds confined in pressure equilibrium with a high temperature intercloud medium (Krolik, McKee and Tarter, 1981). However, there are a number of problems with this two phase picture. First, if the coexistence of the two phases results from radiative heating then the input spectrum required is different from that observed (Fabian *et al.*, 1986, Mathews and Ferland, 1987). Second, the observed Doppler broadening of the emission lines indicates that the clouds have velocities that are supersonic at the Compton temperature, T_C. If the intercloud medium does not move with the clouds and if it is radiatively heated to the Compton temperature then the relative motion is supersonic; the clouds are quickly disrupted by Rayleigh-Taylor instabilities and cannot exist for more than a fraction of the crossing time of the broad line region (Dyson and Perry, 1987).

Mathews and Ferland (1987) asked whether this and other problems could be solved by having an intercloud medium heated non-radiatively to a temperature much greater than T_C. Yaqoob (1990) has shown that a two phase system can result if the heating is non-radiative. However, the confinement or dynamics of such a system must be considered, and the cloud motion must be consistent with the observed line profiles.

In this chapter I study the dynamics of the intercloud medium heated by some mechanism

in addition to radiation. There are a number of possibilities for this additional heating: for example, mechanical processes, alfvenic dissipation, "cosmic rays" (perhaps associated with the relativistic electron component of the synchrotron emitting region). I shall not be specific because the aim is simply to discover whether a consistent solution is possible. I shall assume that the energy injection is effectively a two-body process (i.e. proportional to the local matter density) and suffers geometrical dilution with radius. For consistency I shall also assume that there is a momentum component to the injection. The hot intercloud medium is not confined by the gravity of the central black hole, so I will be considering an outflowing wind. The clouds will move with the wind to avoid break up by Rayleigh-Taylor instabilities. If $T < 10^9$ K then the wind must be supersonic to account for the broadest observed line profiles; thus, I shall only consider solutions in which the wind passes through a sonic point.

3.2 The Model

Consider a stationary cloud of fully ionized hydrogen gas centred on a supermassive black hole, of mass $M = m_8 \times 10^8 M_\odot$, in an active galactic nucleus. The cloud is in hydrostatic equilibrium at the Compton temperature of the surrounding radiation field. Assume the cloud is spherically symmetric. At some arbitrary radius, r_{min}, let us "kick" the gas by injecting heat and/or subjecting it to some force. This heat and/or force is due to an unspecified process, but could be the effect of the injection of high energy particles such as electron positron pairs. Continue to heat up and/or apply force on the gas by an appropriate function of radius, r.

As a result of this injection, the material at the edge of the cloud expands and accelerates outwards. Observations imply that in some AGNs there are high temperature winds that have supersonic velocities, so models of interest are where the heating and force are sufficient to drive the wind to supersonic velocities while remaining at high temperatures. Clearly the wind is subsonic at r_{min}, since the velocity is close to zero, so the model wind must contain a transonic point, a radius r_c where the velocity is the same as the local speed of sound.

Assume that Compton processes are the only important mechanisms of energy and momentum exchange between the radiation and the gas; also assume that the material of the outflow is optically thin to Compton processes, so any change in the radiation spectrum as a result of its interaction with the gas can be neglected. Also observations of the variability of AGNs point towards the central optically thick region being quite small, and therefore an extended wind must be optically thin.

3.3 Equations of Motion

To model the system mathematically, consider the three conservation laws of gas dynamics. I consider steady state flows so the time derivatives are equal to zero. Given a gas of density $\rho(r)$ and temperature $T(r)$ moving out from the centre with a velocity $\boldsymbol{v}(r)$, the conservation laws for mass, momentum and energy can be derived.

3.3.1 The Equation for the Conservation of Mass

This is

$$\nabla.(\rho \boldsymbol{v}) = 0 \tag{3.1}$$

or

$$\frac{1}{r^2}\frac{d}{dr}(r^2 \rho v) = 0. \tag{3.2}$$

Equation (3.2) can be integrated to give $r^2 \rho v =$ constant. The outward flux of mass is $\rho \boldsymbol{v}$, so this constant is related to the mass outflow rate

$$\dot{M} = 4\pi r^2 \rho v. \tag{3.3}$$

3.3.2 The Equation for the Conservation of Momentum

This is

$$\rho \boldsymbol{v}.\nabla \boldsymbol{v} = -\nabla P + \boldsymbol{f}. \tag{3.4}$$

This has the form *(mass density)*$\times$*(acceleration)* $=$ *(force density)*. The right hand side includes a term for gradients in the gas pressure, P, which are forces because momentum is transferred; the other term, $\boldsymbol{f}$, represents any external forces applied to the gas, per unit volume. The left hand side represents the steady convection of momentum by velocity gradients. For this model the external forces are due to gravity, radiation pressure and our extra, unspecified force $\dot{\boldsymbol{m}}(r)$:

$$\boldsymbol{f} = -\frac{GM\rho\hat{\boldsymbol{r}}}{r^2} + n_e \sigma_T P_{rad}\hat{\boldsymbol{r}} + \dot{\boldsymbol{m}}(r). \tag{3.5}$$

Here $\dot{\boldsymbol{m}}(r)$ is the force per unit volume applied (or alternatively, the momentum added to the gas per unit time, per unit volume).

Combining (3.4) and (3.5) and remembering spherical symmetry we obtain

$$\rho v \frac{dv}{dr} = -\frac{dP}{dr} - \frac{GM\rho}{r^2} + n_e \sigma_T P_{rad} + \dot{m}(r). \tag{3.6}$$

3.3.3 The Equation for the Conservation of Energy

This is

$$\nabla . \left[v \left(\frac{1}{2}\rho v^2 + U + P \right) \right] = \boldsymbol{f}.\boldsymbol{v} - \nabla . \boldsymbol{F}_{rad} - \nabla . \boldsymbol{q}. \tag{3.7}$$

Here the left hand side is the sum of the energy fluxes in the gas (kinetic energy density $\frac{1}{2}\rho v^2$, internal energy U) and the flux of the work done by the pressure.

The first term on the right hand side, $\boldsymbol{f}.\boldsymbol{v}$, is the work done on the gas by the external forces $\boldsymbol{f}$. Although in equation (3.5) there are terms due to gravity, radiation pressure and momentum injection, here $\boldsymbol{f}.\boldsymbol{v}$ contains only the contribution due to work done against gravity. This is because the work done on the gas by radiation pressure is included in $-\nabla.\boldsymbol{F}_{rad}$, and the momentum injection $\dot{\boldsymbol{m}}$ is going to be considered exactly that: any work done by this extra force can be assumed to be part of the extra energy injection $\dot{\varepsilon}$.

The second term on the right hand side, $-\nabla.\boldsymbol{q}$, is the conductive flux of heat, which can be neglected here.

The third term on the right hand side, $-\nabla.\boldsymbol{F}_{rad}$, is the rate at which energy is transferred between the gas and the radiation field. I consider only inverse Compton cooling and Compton heating.

Given a thermal distribution function for the electrons, I use the kinetic equation for the Compton interaction of thermal electrons with photons in the non relativistic limit, $\frac{h\nu}{m_e c^2} \ll 1$, $\frac{kT}{m_e c^2} \ll 1$, (Kompaneets, 1957)

$$\frac{\partial \bar{n}}{\partial t} = \frac{\sigma_T n_e h}{m_e c} \frac{1}{\nu^2} \frac{\partial}{\partial \nu} \nu^4 \left(\frac{kT}{h} \frac{\partial \bar{n}}{\partial \nu} + \bar{n} + \bar{n}^2 \right), \tag{3.8}$$

where $\bar{n}$ is the photon occupation number (the density of photons in phase space).

The last term in the brackets on the right hand side describes stimulated Compton scattering, which is only important for high photon fluxes at radio frequencies. This term is negligible in comparisom with the other terms and is dropped. The first term in the brackets is the energy exchanged per scattering from the electron to the photon, and the second term is the energy exchange per scattering from the photon to the electron.

The total photon energy density is

$$U_{rad} = \frac{8\pi h}{c^3} \int_0^\infty \nu^3 \bar{n} d\nu, \tag{3.9}$$

so operating on (3.8) by $\int_0^\infty \nu^3 d\nu$ and integrating by parts twice produces

$$\frac{dU_{rad}}{dt} = \frac{4n_e\sigma_T k}{m_e c}(T - T_C)U_{rad}, \tag{3.10}$$

where the Compton temperature

$$T_C = \frac{h}{4k} \frac{\int_0^\infty \nu^4 \bar{n} d\nu}{\int_0^\infty \nu^3 \bar{n} d\nu}. \tag{3.11}$$

Equation (3.10) is a useful expression for the exchange of energy between the radiation spectrum and the gas. It is obvious that

$$\frac{dU_{rad}}{dt} = -\frac{dU}{dt} \tag{3.12}$$

so that the energy gain of a unit volume of gas per unit time due to radiation processes is

$$-\nabla . \boldsymbol{F}_{rad} = \frac{4n_e\sigma_T k}{m_e c}(T_C - T)U_{rad}. \tag{3.13}$$

Now, rewriting equation (3.7) including the work done against gravity:

$$\frac{d}{dr}\left(\frac{1}{2}\rho v^3 + Uv + Pv\right) = -\frac{GM\rho v}{r^2} + \frac{4n_e\sigma_T k}{m_e c}(T_C - T)U_{rad} + \dot{\varepsilon}(r) \tag{3.14}$$

where $\dot{\varepsilon}(r)$ is the extra energy input (energy added per unit volume per unit time).

3.3.4 Equations of State

In addition to the three conservation laws, there is also an equation of state for the gas: the ideal gas law,

$$P = \frac{\rho k T}{\mu m_p}, \tag{3.15}$$

where μ is the mean molecular weight (the mean mass of the particles in units of m_p, the proton mass). The gas is fully ionized hydrogen so $\mu = \frac{1}{2}$ and $P = \frac{2\rho kT}{m_p}$.

The internal energy density of the gas is U. From elementary kinetic theory each degree of freedom for each particle has an energy associated with it of $\frac{1}{2}kT$. Since the particles are monatomic (or rather a single proton or a single electron) each particle has three degrees of freedom and

$$U = \frac{3}{2}\frac{\rho kT}{\mu m_p} = \frac{3\rho kT}{m_p}. \tag{3.16}$$

I shall also write mass density in terms of the electron number density and the radiation pressure in terms of the radiation energy density which can also be written in terms of the source luminosity:

$$\rho = n_e m_p, \tag{3.17}$$

$$P_{rad} = \frac{U_{rad}}{3}, \tag{3.18}$$

$$U_{rad} = \frac{F_{rad}}{c} = \frac{L}{4\pi r^2 c}. \tag{3.19}$$

3.3.5 The Injection terms

Finally, consider an appropriate functional form for the extra terms $\dot{\varepsilon}(r)$ and $\dot{m}(r)$. I have defined the gas to be optically thin to the radiation, so it seems reasonable to impose the condition that the gas is optically thin to whatever injection process(es) produce $\dot{\varepsilon}(r)$ and $\dot{m}(r)$, i.e. so that the gas does not effect the ability of the injection process to heat or apply force on the gas. It seems reasonable to include a factor proportional to the number density of the wind particles, and also include a $\frac{1}{r^2}$ geometric dilution. So I have defined:

$$\dot{m} = f_m n_e \left(\frac{r}{r_g}\right)^{-2} \quad \text{and} \quad \dot{\varepsilon} = f_\varepsilon n_e \left(\frac{r}{r_g}\right)^{-2}, \tag{3.20}$$

where r_g is the gravitational radius of the central black hole, described by the Schwarzschild metric.

There are many ways to modulate this injection, but I have decided to consider the following cases:

(A) No injection ($\dot{\varepsilon}(r) = 0, \dot{m}(r) = 0$, for all r); i.e. a basic radiation pressure driven optically thin wind.

(B) Injection defined by (3.20) above for $r_{min} < r < \infty$.

(C) As case B but the injection is stopped when the wind velocity becomes supersonic, i.e. $\dot{\varepsilon} = 0$ and $\dot{m} = 0$ for all $r > r_c$. The cutoff at r_c is not entirely arbitrary, if it occurred at a radius less than r_c then this would essentially be the same as case A.

3.3.6 Summary of Equations

Combining equations (3.15) to (3.20) with equations (3.2), (3.6) and (3.14), I obtain:

$$\frac{1}{r^2}\frac{d}{dr}(r^2 n_e v) = 0, \tag{3.21}$$

$$n_e m_p v\frac{dv}{dr} = -2k\frac{d}{dr}(n_e T) - \frac{GMn_e m_p}{r^2} + \frac{n_e\sigma_T L}{12\pi r^2 c} + f_m n_e\left(\frac{r}{r_g}\right)^{-2}, \tag{3.22}$$

$$\frac{d}{dr}\left(\frac{1}{2}n_e m_p v^3 + 5n_e kTv\right) = -\frac{GMn_e m_p v}{r^2} + \frac{4n_e\sigma_T k}{m_e c^2}(T_C - T)\frac{L}{4\pi r^2} + f_\varepsilon n_e\left(\frac{r}{r_g}\right)^{-2}. \tag{3.23}$$

The velocity and the density are related by the mass outflow rate, from (3.3):

$$\dot{M} = 4\pi r^2 n_e m_p v. \tag{3.24}$$

These equations describe the model, and their solution will give velocity, temperature and density as functions of radius, given a suitable choice of the parameters M, L, T_C, $\dot{M}$, f_ε and f_m.

3.3.7 Manipulating the Equations

Using equation (3.24) to replace n_e by functions of v and r in equations (3.21), (3.22), and (3.23), I obtain two coupled ordinary differential equations for the velocity v and the adiabatic sound speed v_s defined

$$v_s^2 = \frac{5P}{3\rho} = \frac{10kT}{3m_p}. \tag{3.25}$$

These equations are:

$$\begin{aligned}(\mathcal{M}^2 - 1)\frac{1}{v}\frac{dv}{dr} = \frac{2}{r} - \frac{GM}{r^2 v_s^2} + \frac{5}{3m_p r^2 v_s^2}\left(\frac{\sigma_T L}{12\pi c} + f_m r_g^2\right) \\ -\frac{1}{3r^2 v}\left(\frac{\sigma_T L}{5\pi m_e c^2}\left(\frac{10kT_C}{3m_p v_s^2} - 1\right) + \frac{2f_\varepsilon r_g^2}{m_p v_s^2}\right),\end{aligned} \tag{3.26}$$

$$\begin{aligned}(1 - \mathcal{M}^2)\frac{1}{v_s}\frac{dv_s}{dr} = \frac{2\mathcal{M}^2}{3r} - \frac{GM}{3r^2 v_s^2} + \frac{5\mathcal{M}^2}{9m_p r^2 v_s^2}\left(\frac{\sigma_T L}{12\pi c} + f_m r_g^2\right) \\ + \left(1 - \frac{5\mathcal{M}^2}{3}\right)\frac{1}{3r^2 v}\left(\frac{\sigma_T L}{10\pi m_e c^2}\left(\frac{10kT_C}{3m_p v_s^2} - 1\right) + \frac{f_\varepsilon r_g^2}{m_p v_s^2}\right).\end{aligned} \tag{3.27}$$

Here $\mathcal{M}$ is the Mach number of the wind, $\mathcal{M} = \frac{v}{v_s}$. Note that the mass outflow rate, $\dot{M}$, does not appear in either of equations (3.26) or (3.27), since the term n_e appears in every term of equations (3.22) and (3.23); $\dot{M}$ is simply a scaling factor for n_e.

To simplify the solving of these equations it is convenient to scale the variables and parameters:

$$x = \frac{r}{r_g},\ u = \frac{v}{\beta c},\ u_s = \frac{v_s}{\beta c}. \tag{3.28}$$

Here β is the velocity, in units of the speed of light c, at a point where $v = v_s = v_c$, the transonic point. Also

$$\lambda = \frac{L}{L_{Edd}} = \frac{\sigma_T L}{4\pi G M m_p c}, \tag{3.29}$$

$$\theta = \frac{10kT_C}{3m_p c^2}, \tag{3.30}$$

$$\phi_\varepsilon = \frac{f_\varepsilon r_g}{m_p c^3}, \tag{3.31}$$

$$\phi_m = \frac{f_m r_g}{m_p c^2}. \tag{3.32}$$

Scaling (3.26) and (3.27) using the above equations produces

$$\begin{aligned}(\mathcal{M}^2 - 1)\frac{1}{u}\frac{du}{dx} = \frac{2}{x} - \frac{1}{2x^2\beta^2 u_s^2} + \frac{5}{3x^2\beta^2 u_s^2}\left(\frac{\lambda}{6} + \phi_m\right) \\ -\frac{2}{3x^2\beta u}\left(\frac{\lambda}{5\mu}\left(\frac{\theta}{\beta^2 u_s^2} - 1\right) + \frac{2\phi_\varepsilon}{\beta^2 u_s^2}\right),\end{aligned} \tag{3.33}$$

$$\begin{aligned}(1 - \mathcal{M}^2)\frac{1}{u_s}\frac{du_s}{dx} = \frac{2\mathcal{M}^2}{3x} - \frac{1}{6x^2\beta^2 u_s^2} + \frac{5\mathcal{M}^2}{9x^2\beta^2 u_s^2}\left(\frac{\lambda}{6} + \phi_m\right) \\ + \left(1 - \frac{5\mathcal{M}^2}{3}\right)\frac{1}{3x^2\beta u}\left(\frac{\lambda}{5\mu}\left(\frac{\theta}{\beta^2 u_s^2} - 1\right) + \frac{\phi_\varepsilon}{\beta^2 u_s^2}\right).\end{aligned} \tag{3.34}$$

Here $\mu = \frac{m_\varepsilon}{m_p}$, the ratio of the mass of the electron to the mass of the proton.

It is clear from these equations that the mass of the black hole effects only the radial scale of the system. This is only to be expected, both the Schwarzchild radius and the Eddington luminosity of a black hole are proportional to its mass, as is the critical mass outflow rate, such that the outflow is not supercritical.

In equation (3.33) the external forces acting on the gas particles are represented by the term

$$\frac{5}{3x^2\beta^2 u_s^2}\left(\frac{\lambda}{6} + \phi_m\right). \tag{3.35}$$

This implies that if the extra force due to $\dot{m}$ is equivalent to the radiation pressure force then $\phi_m = \frac{\lambda}{6}$.

Again, in equation (3.33) the terms from the equation of conservation of energy that represent the extra heating $\dot{\epsilon}$ and the transfer of energy between the gas and the radiation field appear as

$$\frac{2}{3x^2\beta u}\left(\frac{\lambda}{5\mu}\left(\frac{\theta}{\beta^2 u_s^2}-1\right)+\frac{\phi_\epsilon}{\beta^2 u_s^2}\right). \tag{3.36}$$

Here, if the energy gain in the gas due to the extra heating is equivalent to the energy gain due to Compton heating (ignoring inverse Compton cooling), then $\phi_\epsilon = \frac{\lambda\theta}{5\mu}$.

These two equivalences will be useful when I consider the ϕ_ϵ and ϕ_m parameter space.

3.4 The Transonic Point

In order to solve equations (3.33) and (3.34) a choice has to be made for the initial values of u, u_s and x. In principle I can choose any set of numbers and integrate from there, but I am looking for a particular kind of solution: i.e. where there is a radius such that the velocity is the same as the sound speed; it is sensible therefore to use $u = u_s = 1$ at $x = x_c$ for the initial conditions. At this point the denominator of $\frac{du}{dx}$ and $\frac{du_s}{dx}$, $(\mathcal{M}^2 - 1)$, is zero, implying that the transonic point is a critical point of the system and must be treated carefully to avoid complications occurring in the solution. So x_c is determined by the requirement that u and u_s pass smoothly (i.e with finite derivatives) through the sonic point.

Substituting $u = 1$, $u_s = 1$, and $x = x_c$ in either equations (3.33) and (3.34)

$$\frac{2}{x_c}-\frac{1}{2x_c^2\beta^2}+\frac{5}{3x_c^2\beta^2}\left(\frac{\lambda}{6}+\phi_m\right)-\frac{2}{3x_c^2\beta}\left(\left(\frac{\lambda\theta}{5\mu}+\phi_\epsilon\right)\frac{1}{\beta^2}-\frac{\lambda}{5\mu}\right)=0. \tag{3.37}$$

Rearranging

$$x_c=\left(\frac{\lambda\theta}{5\mu}+\phi_\epsilon\right)\frac{1}{3\beta^3}+\left(\frac{1}{4}-\frac{5}{6}\left(\frac{\lambda}{6}+\phi_m\right)\right)\frac{1}{\beta^2}-\frac{\lambda}{15\mu\beta}, \tag{3.38}$$

i.e. given a choice for the parameters λ, θ, ϕ_ϵ, ϕ_m and β there is only one point where $u = u_s$

The condition $u = u_s = 1$ at $x = x_c$ cannot be used as the initial condition, because at that point both equations (3.33) and (3.34) revert to $0 = 0$; i.e. $\frac{du}{dx} = \frac{0}{0}$ and $\frac{du_s}{dx} = \frac{0}{0}$ which gives no information about the system at values of x other than x_c.

Any function can be represented by an infinite Taylor series, expanded about a given point. If the region of that function is sufficiently small the Taylor series can be truncated to the first

few terms. In this situation, the region is so small that the series can be truncated to a linear equation. For example, writing $u(x)$ as a Taylor series expanded about the point x_c,

$$u(x) = u(x_c) + (x - x_c)\left.\frac{du}{dx}\right|_{x=x_c} + (x - x_c)^2\left.\frac{d^2u}{dx^2}\right|_{x=x_c} + \cdots. \tag{3.39}$$

If $(x - x_c)$ is sufficiently small

$$u(x) = u(x_c) + (x - x_c)\left.\frac{du}{dx}\right|_{x=x_c}. \tag{3.40}$$

Now $u(x_c) = 1$, and also writing $(x - x_c) = \delta x$ and $\left.\frac{du}{dx}\right|_{x-x_c} = u'$ gives

$$u(x) = 1 + u'\delta x. \tag{3.41}$$

Similarly, $u_s(x)$ can be expanded about x_c to give

$$u_s(x) = 1 + u_s'\delta x \tag{3.42}$$

Rearranging equations (3.33) and (3.34) I obtain

$$x^2\left(u^2 - u_s^2\right)\frac{du}{dx} = 2xuu_s^2 - \frac{u}{2\beta^2} + \frac{5u}{3\beta^2}\left(\frac{\lambda}{6} + \phi_m\right) - \frac{2}{3\beta}\left(\frac{\lambda}{5\mu}\left(\frac{\theta}{\beta^2} - u_s^2\right) + \frac{\phi_\varepsilon}{\beta^2}\right), \tag{3.43}$$

$$\begin{aligned} x^2\left(u_s^2 - u^2\right)uu_s\frac{du_s}{dx} &= \frac{2}{3}xu^3u_s^2 - \frac{uu_s^2}{6\beta^2} + \frac{5u^3}{9\beta^2}\left(\frac{\lambda}{6} + \phi_m\right) \\ &\quad + \left(u_s^2 - \frac{5}{3}u^2\right)\frac{1}{3\beta}\left(\frac{\lambda}{5\mu}\left(\frac{\theta}{\beta^2} - u_s^2\right) + \frac{\phi_\varepsilon}{\beta^2}\right). \end{aligned} \tag{3.44}$$

Substituting equations (3.41) and (3.42) and into equations (3.43) and (3.44), using $x = x_c + \delta x$ and ignoring second and higher powers of δx, gives:

$$\begin{aligned} &\left(x_c^2 + 2x_c\delta x\right)\left(\left(1 + 2u'\delta x\right) - \left(1 + 2u_s'\delta x\right)\right)u' = 2\left(x_c + \delta_x\right)\left(1 + u'\delta x\right)\left(1 + 2u_s'\delta x\right) \\ &-\frac{\left(1 + u'\delta x\right)}{2\beta^2} + \frac{5}{3}\frac{\left(1 + u'\delta x\right)}{\beta^2}\left(\frac{\lambda}{6} + \phi_m\right) - \frac{2}{3\beta}\left(\frac{\lambda}{5\mu}\left(\frac{\theta}{\beta^2} - \left(1 + 2u_s'\delta x\right)\right) + \frac{\phi_\varepsilon}{\beta^2}\right), \end{aligned} \tag{3.45}$$

$$\begin{aligned} &\left(x_c^2 + 2x_c\delta x\right)\left(\left(1 + 2u_s'\delta x\right) - \left(1 + 2u'\delta x\right)\right)\left(1 + u'\delta x\right)\left(1 + u_s'\delta x\right)u_s' \\ &= \frac{2}{3}\left(x_c + \delta_x\right)\left(1 + 3u'\delta x\right)\left(1 + 2u_s'\delta x\right) - \frac{\left(1 + u'\delta x\right)\left(1 + 2u_s'\delta x\right)}{6\beta^2} \\ &\qquad + \frac{5}{9}\frac{\left(1 + 3u'\delta x\right)}{\beta^2}\left(\frac{\lambda}{6} + \phi_m\right) \\ &+ \left(\left(1 + 2u_s'\delta x\right) - \frac{5}{3}\left(1 + 2u'\delta x\right)\right)\frac{1}{3\beta}\left(\frac{\lambda}{5\mu}\left(\frac{\theta}{\beta^2} - \left(1 + 2u_s'\delta x\right)\right) + \frac{\phi_\varepsilon}{\beta^2}\right). \end{aligned} \tag{3.46}$$

Each equation (3.45) and (3.46) can be written in the form $a_1 + a_2\delta x = 0$, which can only be true if $a_1 = 0$ and $a_2 = 0$, hence examining the coefficients of $(\delta x)^0$ and $(\delta x)^1$ will provide

useful information about the system of equations. Examining the the coefficients of $(\delta x)^0$ in either equation (3.45) or (3.46) is the same as setting $\delta x = 0$ and just gives the critical point condition, equation (3.38). However examining the coefficients of $(\delta x)^1$ yields two equations with two unknowns u' and u'_s:

$$2x_c^2\left(u'-u'_s\right)u' = 2\left(2x_c u'_s + x_c u' + 1\right) - \frac{u'}{2\beta^2} + \frac{5u'}{3\beta^2}\left(\frac{\lambda}{6}+\phi_m\right) + \frac{4\lambda u'_s}{15\mu\beta}, \tag{3.47}$$

$$\begin{aligned} 2x_c^2\left(u'_s-u'\right)u'_s &= \frac{2}{3}\left(2x_c u'_s + 3x_c u' + 1\right) - \frac{2u'_s+u'}{6\beta^2} + \frac{5u'}{3\beta^2}\left(\frac{\lambda}{6}+\phi_m\right) \\ &+\frac{4}{45}\frac{\lambda u'_s}{\mu\beta} + 2\left(u'_s - \frac{5}{3}u'\right)\frac{1}{3\beta}\left(\frac{\lambda}{5\mu}\left(\frac{\theta}{\beta^2}-1\right)+\frac{\phi_\varepsilon}{\beta^2}\right). \end{aligned} \tag{3.48}$$

Rearranging equation (3.47):

$$u'_s = \frac{u'^2 x_c^2 - u' x_c - 1 - \frac{5u'}{6\beta^2}\left(\frac{\lambda}{6}+\phi_m\right) + \frac{1}{4\beta^2}u'}{u' x_c^2 + 2x_c + \frac{2\lambda}{15\mu\beta}}. \tag{3.49}$$

Substituting this into equation (3.48) and rearranging, gives an equation of the form

$$a_3\left(\frac{u'}{6\beta^3}\right)^3 + a_2\left(\frac{u'}{6\beta^3}\right)^2 + a_1\left(\frac{u'}{6\beta^3}\right) + a_0 = 0, \tag{3.50}$$

where the coefficients a_0 to a_3 depend only upon the values of the parameters λ, θ, ϕ_ε, ϕ_m and β. This equation can be solved for u' numerically using a suitable method, from which the value of u' can be calculated using equation (3.49). There are three solutions for u' from that satisfy (3.50) of which two may be complex. The solutions of interest are where u' is real, where $u' > u'_s$ and $u' > 0$, i.e. a solution is required where the wind is subsonic for $x < x_c$, supersonic for $x > x_c$ and accelerating. In principle, there may be solutions of equation (3.50) where $u' > u'_s$ but the wind is decelerating, but these solutions are of no interest here.

3.5 The Optical Depth

To simplify the numerical method, I decided to calculate the optical depth in the wind from the point of view of an observer at the transonic point, r_c. The optical depth between a point at radius r, and the observer at r_c is:

$$\tau(r) = -\int_{r_c}^{r} \sigma_T n_e dr. \tag{3.51}$$

Here I have defined a convention such that if the point $r < r_c$, then the optical depth calculated is a positive quantity; while if $r > r_c$, then it is a negative quantity. Hence, the optical depth between a point at radius r, and an observer at radius r_{obs} is:

$$\tau_{obs}(r) = \tau(r) - \tau(r_{obs}). \tag{3.52}$$

The electron number density is related to the wind velocity by equation (3.24) which can be scaled using equations (3.28) to give:

$$\dot{M} = 4\pi r_g^2 m_p c n_e x^2 u \beta. \tag{3.53}$$

Rearranging this equation in terms of n_e, and substituting for τ from equations (3.28), equation (3.51) can be rewritten

$$\tau(x) = \frac{\dot{M}\sigma_T}{4\pi r_g m_p c \beta} \int_x^{x_c} \frac{dx}{x^2 u}, \tag{3.54}$$

$$\tau(x) = 4.506 \left(\frac{\dot{M}}{M_\odot \mathrm{yr}^{-1}} \right) \frac{1}{m_8 \beta} \int_x^{x_c} \frac{dx}{x^2 u}. \tag{3.55}$$

It is convenient to scale $\tau(x)$:

$$\tau^*(x) = m_8 \tau(x) \left(\frac{\dot{M}}{M_\odot \mathrm{yr}^{-1}} \right)^{-1}, \tag{3.56}$$

so that now

$$\tau^*(x) = \frac{4.506}{\beta} \int_x^{x_c} \frac{dx}{x^2 u}. \tag{3.57}$$

3.6 The Energy Injection

From equation (3.20) the extra heating per unit volume per unit time is

$$\dot{\varepsilon} = f_\varepsilon n_e \left(\frac{r}{r_g} \right)^{-2},$$

so the total energy injected into the whole wind per unit time is, for Case B:

$$E = \int_{r_{min}}^{\infty} 4\pi r^2 \dot{\varepsilon} dr = \int_{r_{min}}^{\infty} 4\pi r_g^2 f_\varepsilon n_e dr. \tag{3.58}$$

Now, consider the optical depth to Compton scattering between r_{min} and an observer at an infinite distance. This is

$$\tau_\infty = \int_{r_{min}}^{\infty} n_e \sigma_T dr, \tag{3.59}$$

or, referring back to equations (3.51) and (3.52)

$$\tau_\infty = \tau(r_{min}) - \tau(r \to \infty). \tag{3.60}$$

Therefore, if f_ε is a constant, equation (3.58) becomes

$$E = 4\pi r_g^2 f_\varepsilon \tau_\infty / \sigma_T. \tag{3.61}$$

From the scaling equation (3.31), $\phi_\varepsilon = \frac{f_\varepsilon r_g}{m_e c^2}$ and

$$E = \frac{4\pi r_g m_p c^3}{\sigma_T}\phi_\varepsilon \tau_\infty. \tag{3.62}$$

The Eddington limit for the luminosity of a massive object is $L_{Edd} = 4\pi GMm_p c/\sigma_T$ and the gravitational radius is $r_g = \frac{2GM}{c^2}$; this means that E can be scaled:

$$\frac{E}{L_{Edd}} = 2\phi_\varepsilon \tau_\infty. \tag{3.63}$$

A realistic order of magnitude limitation is that the wind should contain no more energy than an Eddington limited source can supply in all forms (whether it is radiation or high energy particles); thus the maximum value of ϕ_ε should be limited by $E < L_{Edd}$.

Considering case C, the extra heating stops once the wind reaches supersonic velocities so now

$$E = \int_{r_{min}}^{r_c} 4\pi r^2 \dot{\varepsilon} dr = 4\pi r_g^2 f_\varepsilon \tau(r_{min})/\sigma_T, \tag{3.64}$$

and the scaled energy input is

$$\frac{E}{L_{Edd}} = 2\phi_\varepsilon \tau(x_{min}). \tag{3.65}$$

3.7 The Parameter Space

The freedom to choose parameters is constrained by referring to observations of active galaxies. The Compton temperature, $T_C \sim 10^7$K, is obtained from the observed spectrum (Mathews and Ferland, 1987), this is equivalent to $\theta = 3.06 \times 10^{-6}$. I have chosen luminosities $L = L_{Edd}$ and $L = 0.1L_{Edd}$, equivalent to $\lambda = 1.0$ and $\lambda = 0.1$.

The temperature at the sonic point is $T(x_c) = 3.266 \times 10^{12}\beta^2$K, so a reasonable range is, say, $10^{-3} \leq \beta$. This still allows fairly cool winds with $T(x_c) \gtrsim 3 \times 10^6$K.

What sort of values is it sensible to choose for ϕ_ε and ϕ_m? Referring back to the discussion after equations (3.35) and (3.36) the energy injection is equivalent to the Compton heating when $\phi_\varepsilon = \frac{\lambda\theta}{5\mu}$ and the momentum injection is equivalent to the radiation pressure force when $\phi_m = \frac{\lambda}{6}$. Therefore choosing $\phi_\varepsilon > \frac{1}{10}\frac{\lambda\theta}{5\mu}$ and $\phi_m > \frac{1}{10}\frac{\lambda}{6}$ seems sensible. The method I adopted was to experiment with various values of ϕ_ε and ϕ_m, which indeed showed that as ϕ_ε or ϕ_m became smaller than these lower limits, there were no changes to the final solutions. Figures 3.1 to 3.4 show x_c is essentially unchanged for smaller values of ϕ_ε or ϕ_m.

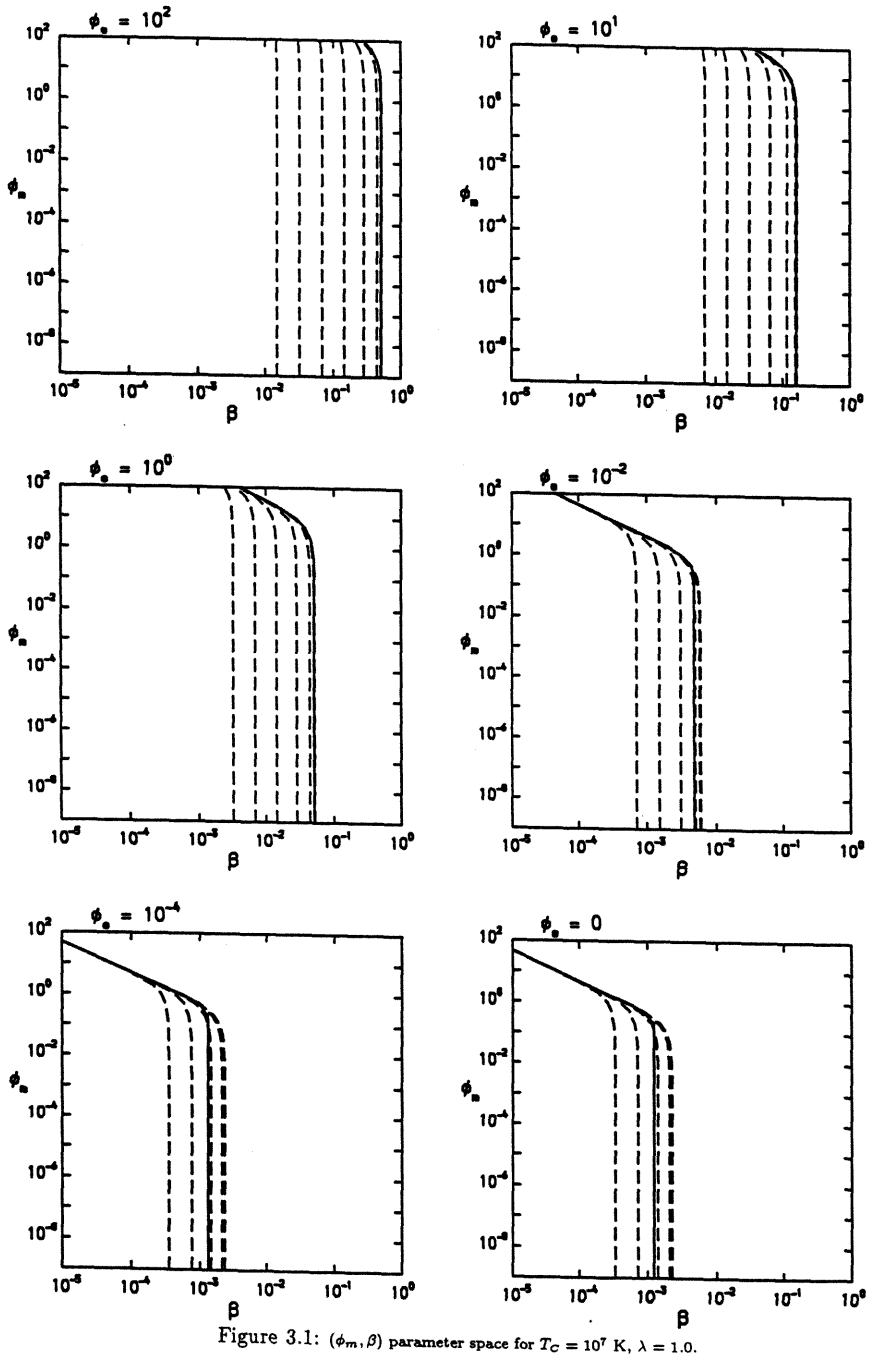

Figure 3.1: (ϕ_m, β) parameter space for $T_C = 10^7$ K, $\lambda = 1.0$.

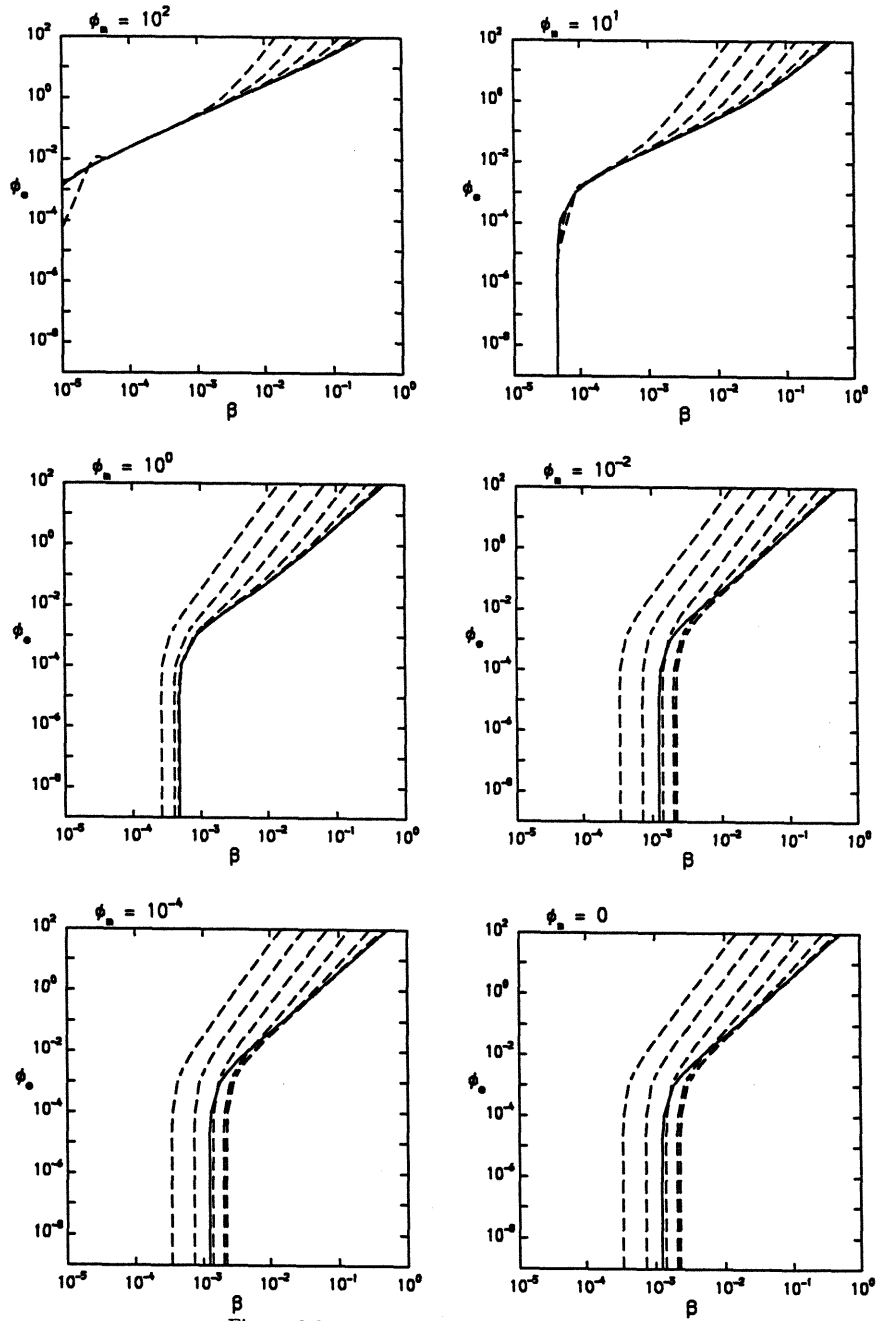

Figure 3.2: (ϕ_e, β) parameter space for $T_C = 10^7$ K, $\lambda = 1.0$.

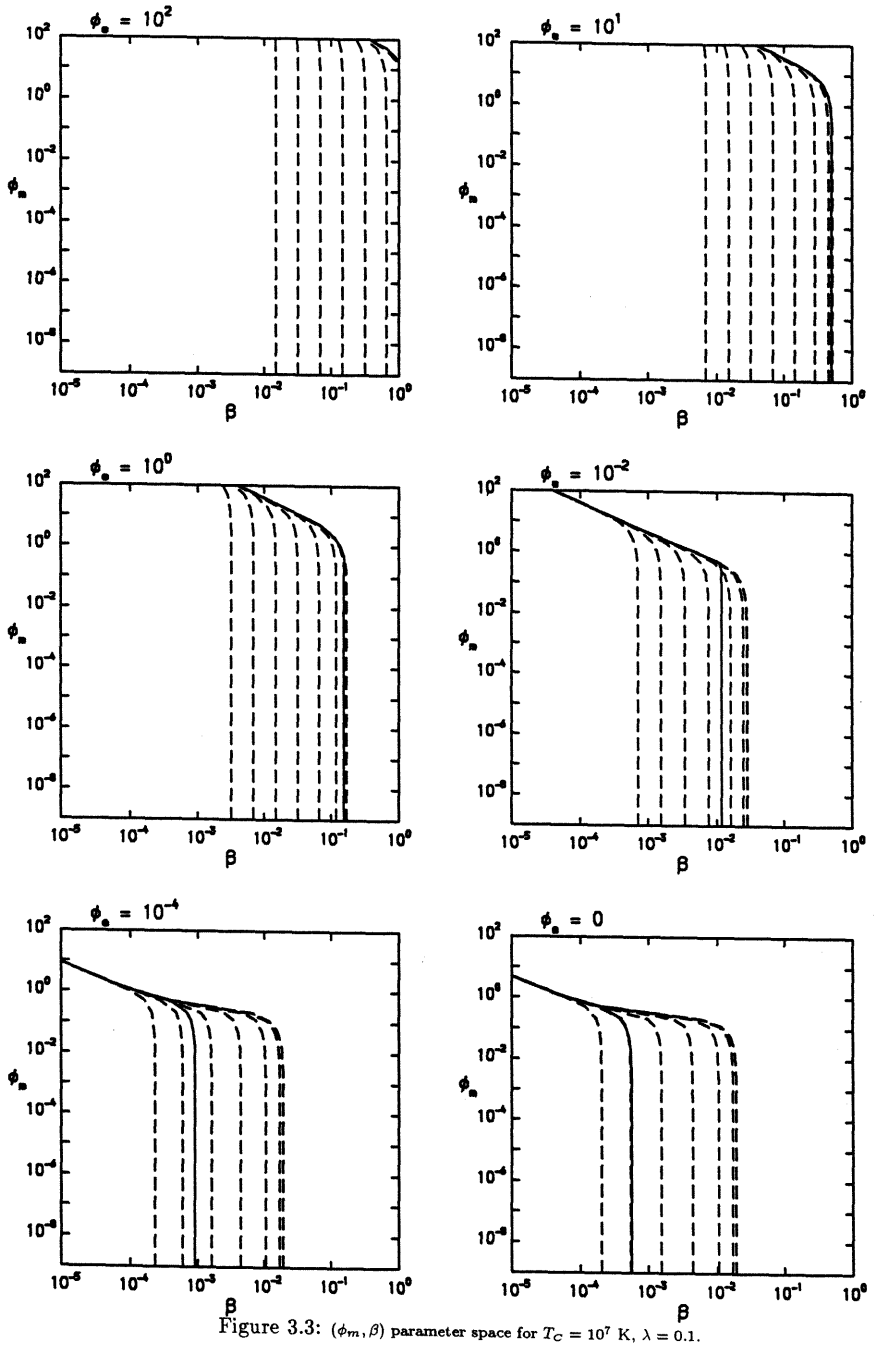

Figure 3.3: (ϕ_m, β) parameter space for $T_C = 10^7$ K, $\lambda = 0.1$.

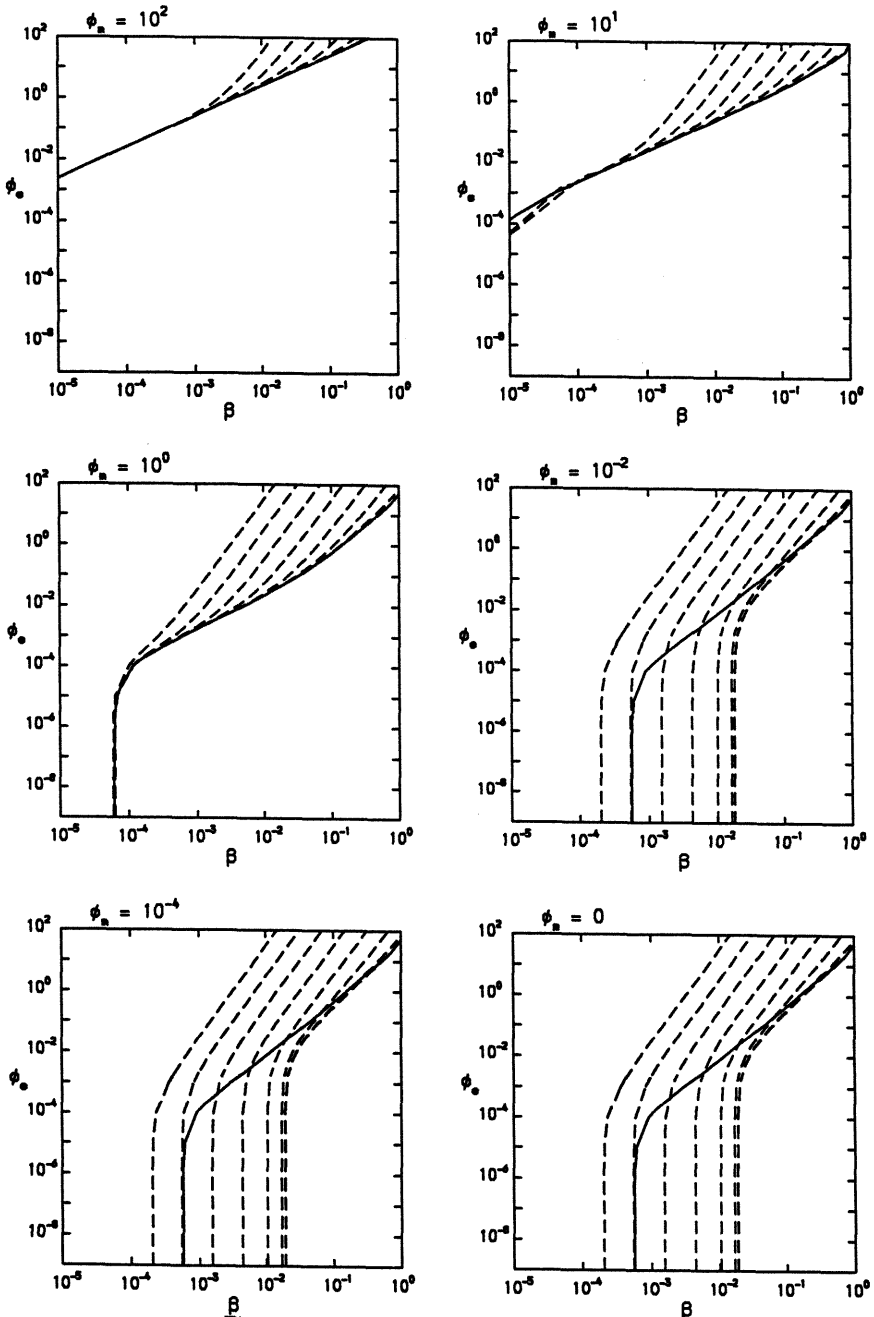

Figure 3.4: (ϕ_ϵ, β) parameter space for $T_C = 10^7$ K, $\lambda = 0.1$.

From the discussion after equation (3.63), the maximum value of ϕ_ε is set by the energy injection rate and the optical depth. If the source is Eddington limited and optical depth $\tau < 0.1$, say, then $\phi_\varepsilon < 0.1$. To allow for smaller optical depths I used the constraint $\phi_\varepsilon < 100$. The results will show that the solutions of interest have small values of ϕ_m, hence the upper limit of this parameter is not important; I used the constraint $\phi_m < 100$.

The $(\phi_\varepsilon, \phi_m, \beta)$ parameter space is further constrained by physical limitations, §3.4 states that only those solutions where the wind accelerates from a subsonic region to a supersonic region are of interest. If β is large, given ϕ_ε and ϕ_m, these conditions are not obeyed, reducing the useful range of β.

The sonic point, x_c, must occur within a range of radii that will produce interesting solutions. Clearly $x_c > x_g$ otherwise the sonic point is inside the black hole. The critical point condition, equation (3.38), shows that this tends to occur with large β. At the other extreme, small values of β result in critical radii so large that the supersonic region is well outside the volume of space of interest; hence I have chosen the constraint $x_c < 10^7$ (equivalent to $r_c < 10^{21} m_8 \mathrm{cm}$), with a corresponding minimum value for β, found by substituting $x_c = 10^7$ in equation (3.37) and solving for β numerically. This constaint is only necessary for large ϕ_ε, it turns out that when ϕ_ε is small $x_c < 10^7$ for all β such that $10^{-3} \leq \beta < 1$.

Figures 3.1 to 3.4 show the $(\phi_\varepsilon, \phi_m, \beta)$ parameter space for $T_C = 10^7 \mathrm{K}$, $\lambda = 1.0$ and $\lambda = 0.1$. The dashed lines represent contours of x_c in the parameter space, calculated from equation (3.38). In each graph, the left most dashed line (lowest β) represents the loci of points where $x_c = 10^7$. Moving to the right (β increasing), each dashed line represents the loci of points where $x_c = 10^6, 10^5, 10^4, 10^3, 10^2, 10$ and 1 respectively. The continuous line represents the maximum value of β such that the constraints of the previous paragraph are obeyed.

There is a particular region of the $(\phi_\varepsilon, \phi_m, \beta)$ parameter space which obeys all the above restrictions, but in practice when solving equations (3.33) and (3.34) does not produce useful results. After choosing values for ϕ_ε and ϕ_m, if β is large equation (3.37) indicates that x_c is small. The implication is that the gradient $u'(x_c)$ is very large, and also that $u'_s(x_c)$ is large. I have also found that $u'(x_c) \simeq u'_s(x_c)$. The large gradients mean that the functions $u(x)$ and $u_s(x)$ are rapidly changing and because the gradients are almost the same, any small error in a numerical calculation can drive the system away from the "correct" result. The practical effect here is to further reduce the maximum useful value that can be chosen for β, given a choice of ϕ_ε and ϕ_m.

3.8 The Numerical Method

To solve equations (3.33) and (3.34), I use the NAG Fortran Library routine D02EBF, which integrates stiff systems of first order ordinary differential equations using backward differentiation formulae. Having chosen values for the parameters λ, θ, ϕ_ε, ϕ_m and β, x_c is calculated from the critical point condition, equation (3.38). Next u' and u_s' are found by solving equation (3.50), and substituting the result into equation (3.49). Then setting $x = x_c - \delta x$, where $\delta x \lesssim 10^{-4} x_c$, the values of $u(x)$ and $u_s(x)$ are calculated using equations (3.41) and (3.42), the Taylor series truncated to a linear form. Using these values for x, u and u_s as the initial conditions, equations (3.33) and (3.34) are integrated until the point when $u \simeq 10^{-4}$ is reached, the integration proceeding in a negative x direction. I then define x_{min} as the value of x where $u \simeq 10^{-4}$.

In the analogous problem where the unknowns are functions of time, this would be equivalent to integrating backwards in time, where equations can become unstable, using backward differentiation formulae counteracts this effect.

After completing the inward integration, the values of $u(x)$ and $u_s(x)$ at $x = x_c + \delta x$ are calculated and these values used as the initial conditions for an integration that proceeds in the positive x direction, until $u(x)$ reaches its asymptotic value.

On completion of both integrations, numerical functions have been calculated for $u(x)$ and $u_s(x)$ for the region between x_{min} (where $u \simeq 10^{-4}$) and where u is approximately constant at large x. It is now possible to calculate the optical depth of the wind to Compton scattering, and also make some estimate of the total energy injected by the extra heating term $\dot{\varepsilon}$. The optical depth calculation is important: it is one of the major assumptions of the physical model that the wind is optically thin, so the solution must be consistent with that assumption. It is also important to know the energy budget required for a particular solution.

3.9 Results

The equations were solved with $T_C = 10^7$K, and $\lambda = 1.0$ and $\lambda = 0.1$. Values for ϕ_ε and ϕ_m were chosen from the set 10^2, 1, 10^{-2}, 10^{-4}, 10^{-6} and 0. Given values for T_C, λ, ϕ_ε, ϕ_m, there is a range of values that can be chosen for β, as discussed in §3.7. The equations were solved for $u(x)$, $u_s(x)$ and $\tau^*(x)$, using the methods described in §3.8, with three choices of β, one

Table 3.1: Values of parameters used in figures 3.9 and 3.16.

In each case $T_C = 10^7$.

(a) $\lambda = 1.0, \phi_m = 0$ for various ϕ_ϵ

(b) $\lambda = 1.0, \phi_\epsilon = 100$ for various ϕ_m

(c) $\lambda = 1.0, \phi_\epsilon = 1$ for various ϕ_m

(d) $\lambda = 0.1, \phi_m = 0$ for various ϕ_ϵ

(e) $\lambda = 0.1, \phi_\epsilon = 100$ for various ϕ_m

(f) $\lambda = 0.1, \phi_\epsilon = 1$ for various ϕ_m

each from the lower, middle and higher ends of this range of values. In addition, the functions $\beta(x_{min})$ and $\beta(x_c)$ were evaluated over this range of β.

Figures 3.5 to 3.8 show $\beta(x_{min})$ and $\beta(x_c)$ for various values of the other parameters. In figures 3.5 and 3.6 $\lambda = 1.0$, in figures 3.7 and 3.8 $\lambda = 0.1$. Figures 3.5 and 3.7 show how $\beta(x_{min})$ and $\beta(x_c)$ vary as ϕ_m decreases, with ϕ_ϵ set at the values 10^2 and 1. In each set of graphs, it is clear that the results are the same when $\phi_m = 10^{-2}$ and $\phi_m = 0$. Figures 3.6 and 3.8 show the results for different values of ϕ_ϵ with $\phi_m = 0$. With ϕ_ϵ decreasing, the functions $\beta(x_{min})$ and $\beta(x_c)$ remain the same when $\phi_\epsilon \lesssim 10^{-4}$. Thus for $\phi_\epsilon \lesssim 10^{-4}$ and $\phi_m \lesssim 10^{-2}$, $\beta(x_{min})$ and $\beta(x_c)$ are approximately the same as for $\phi_\epsilon = 0$ and $\phi_m = 0$.

Figure 3.9 shows x_c/x_{min} versus β for various ϕ_ϵ and ϕ_m. It is apparent that the subsonic region extends over a region no more than a few times r_{min} for values of ϕ_ϵ and ϕ_m that are significantly different from their lower limits.

In each case, whatever the choice of ϕ_ϵ, ϕ_m or β, the functional forms of $u(x)$, $u_s(x)$ and $\tau^*(x)$ shown in figures 3.10 to 3.15 are basically the same: the velocity rises rapidly to begin with and tends to a constant value at large x, the sound speed rises from a low value to a maximum near x_c and then falls. Choosing β essentially chooses the maximum temperature since $u_{s_{max}} \simeq \beta$.

3.9.1 Case A: No extra heat or force

In this case $\phi_\epsilon = \phi_m = 0$. Some results are given in figures 3.10 and 3.11, which show the functions $u(x)$, $u_s(x)$ and $\tau^*(x)$ for various values of λ and β. In figure 3.10 $\lambda = 1.0$ and $\beta = 4 \times 10^{-4}$, 1.2×10^{-3} and 1.24×10^{-3}. In figure 3.11 $\lambda = 0.1$ and $\beta = 2.5 \times 10^{-4}$, 3.5×10^{-4} and 5×10^{-4}. In addition, $\beta(x_{min})$ and $\beta(x_c)$ are represented in figures 3.6 and 3.8.

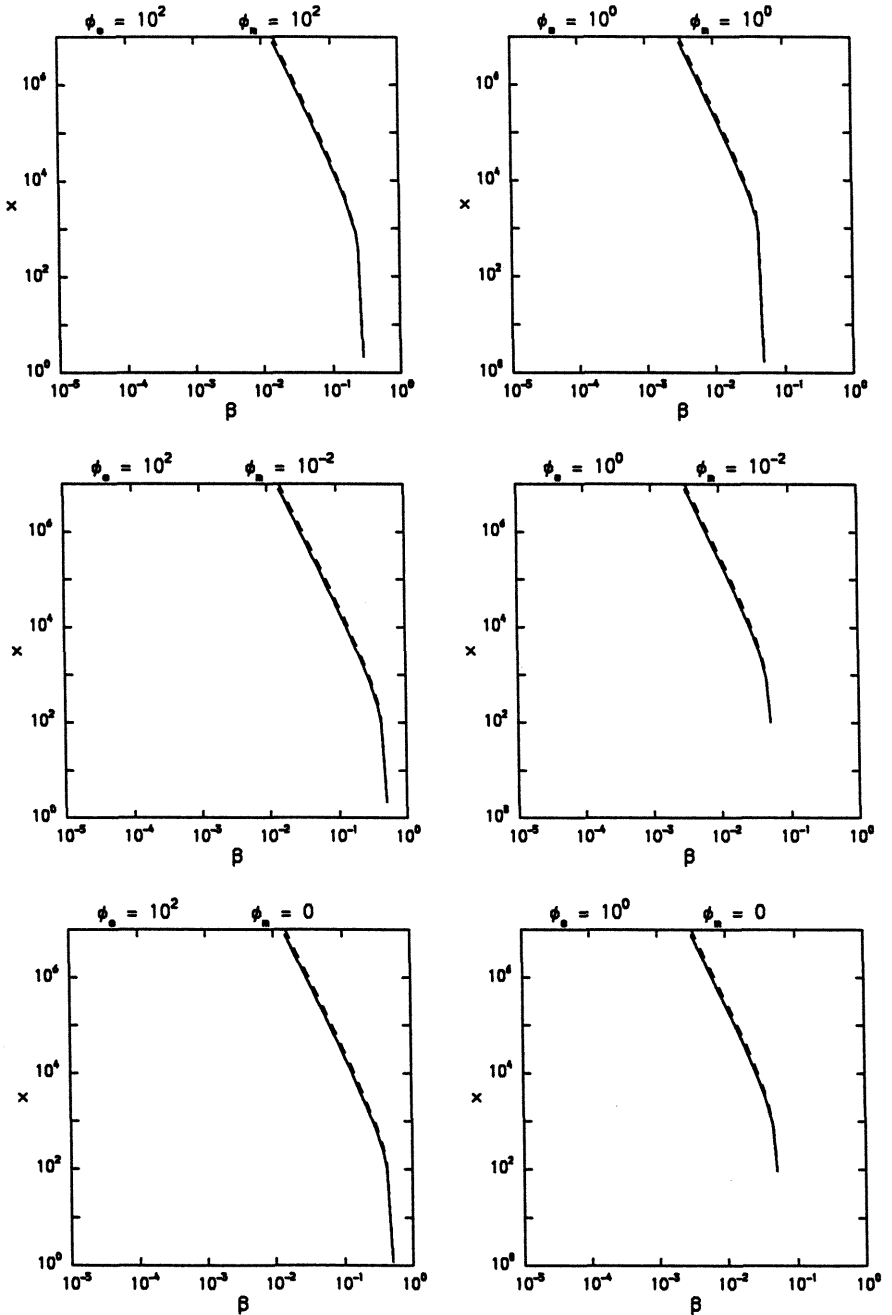

Figure 3.5: $\beta(x_{min})$, solid line, and $\beta(x_c)$, dashed line, varying as ϕ_m decreases, with ϕ_e set at 10^2 and 1; $\lambda = 1.0$.

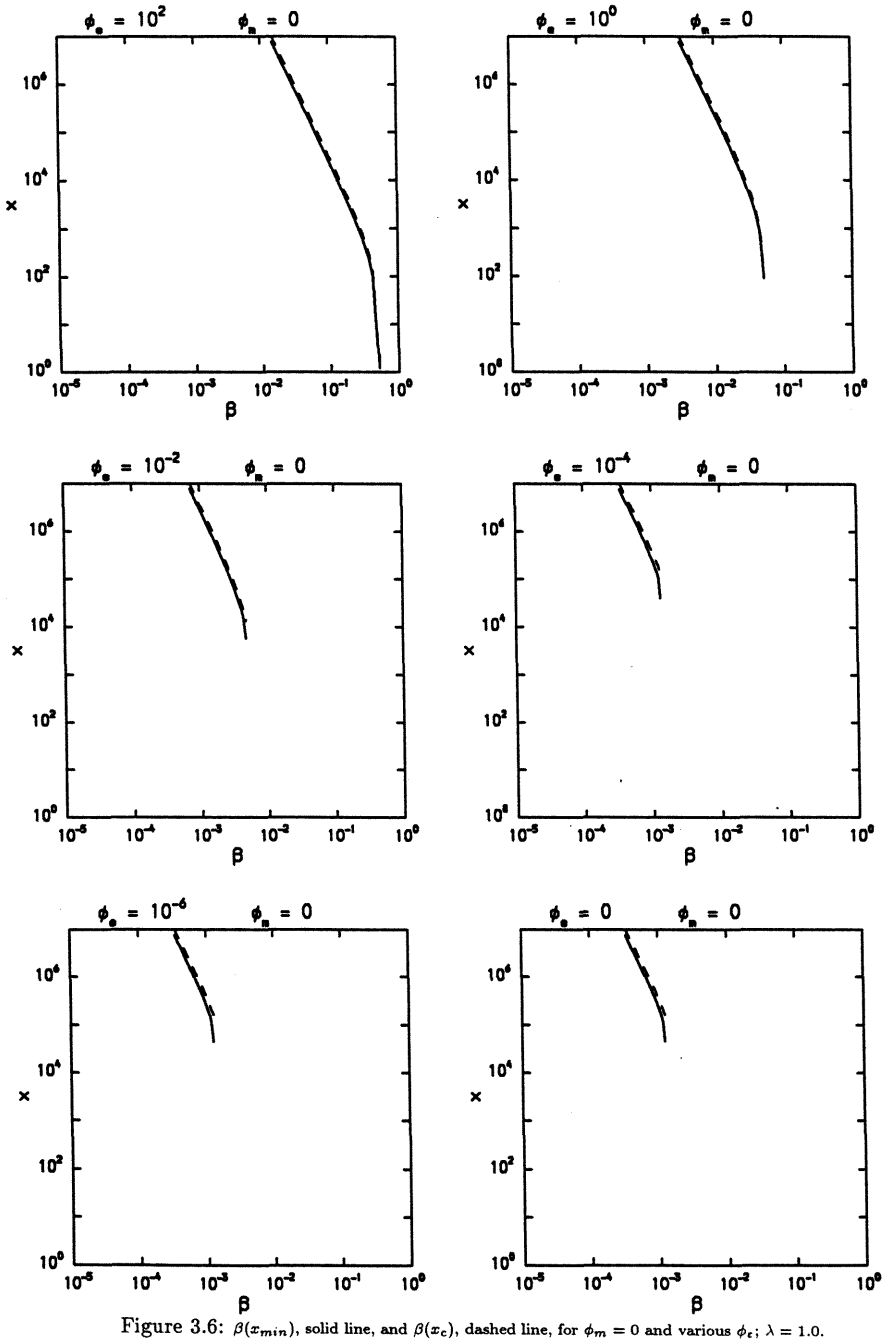

Figure 3.6: $\beta(x_{min})$, solid line, and $\beta(x_c)$, dashed line, for $\phi_m = 0$ and various ϕ_e; $\lambda = 1.0$.

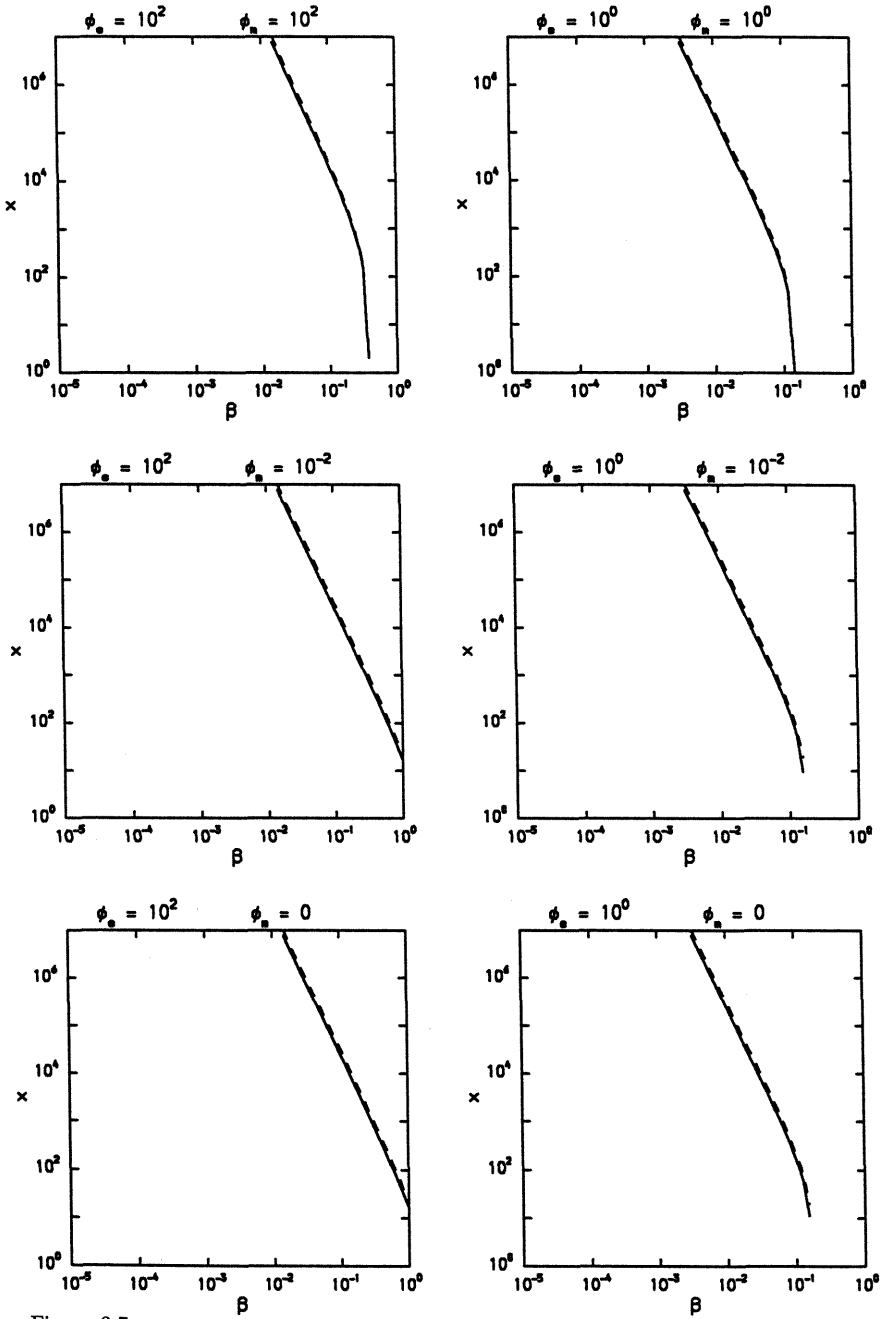

Figure 3.7: $\beta(x_{min})$, solid line, and $\beta(x_c)$, dashed line, varying as ϕ_m decreases, with ϕ_e set at 10^2 and 1; $\lambda = 0.1$.

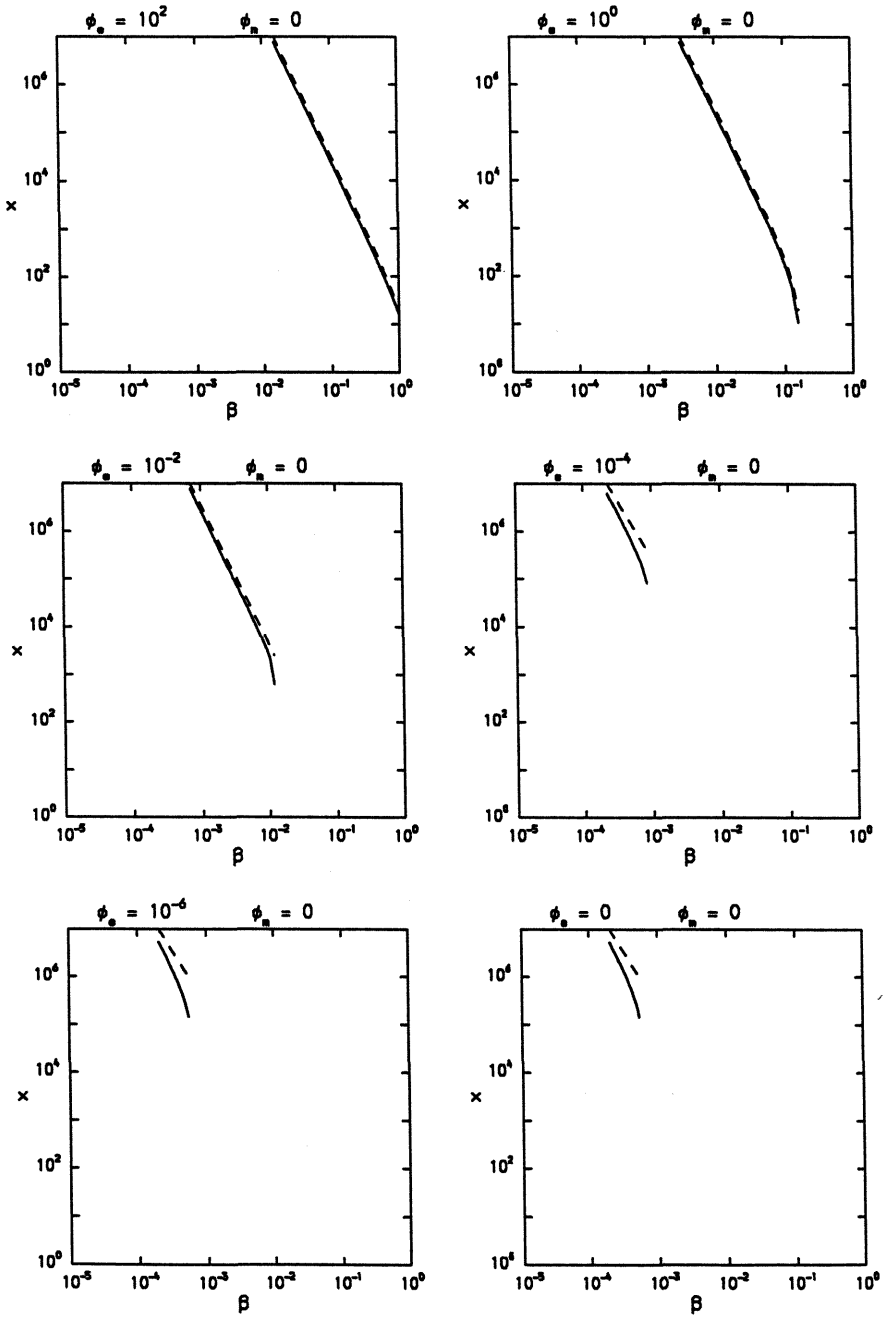

Figure 3.8: $\beta(x_{min})$, solid line, and $\beta(x_c)$, dashed line, for $\phi_m = 0$ and various ϕ_c; $\lambda = 0.1$.

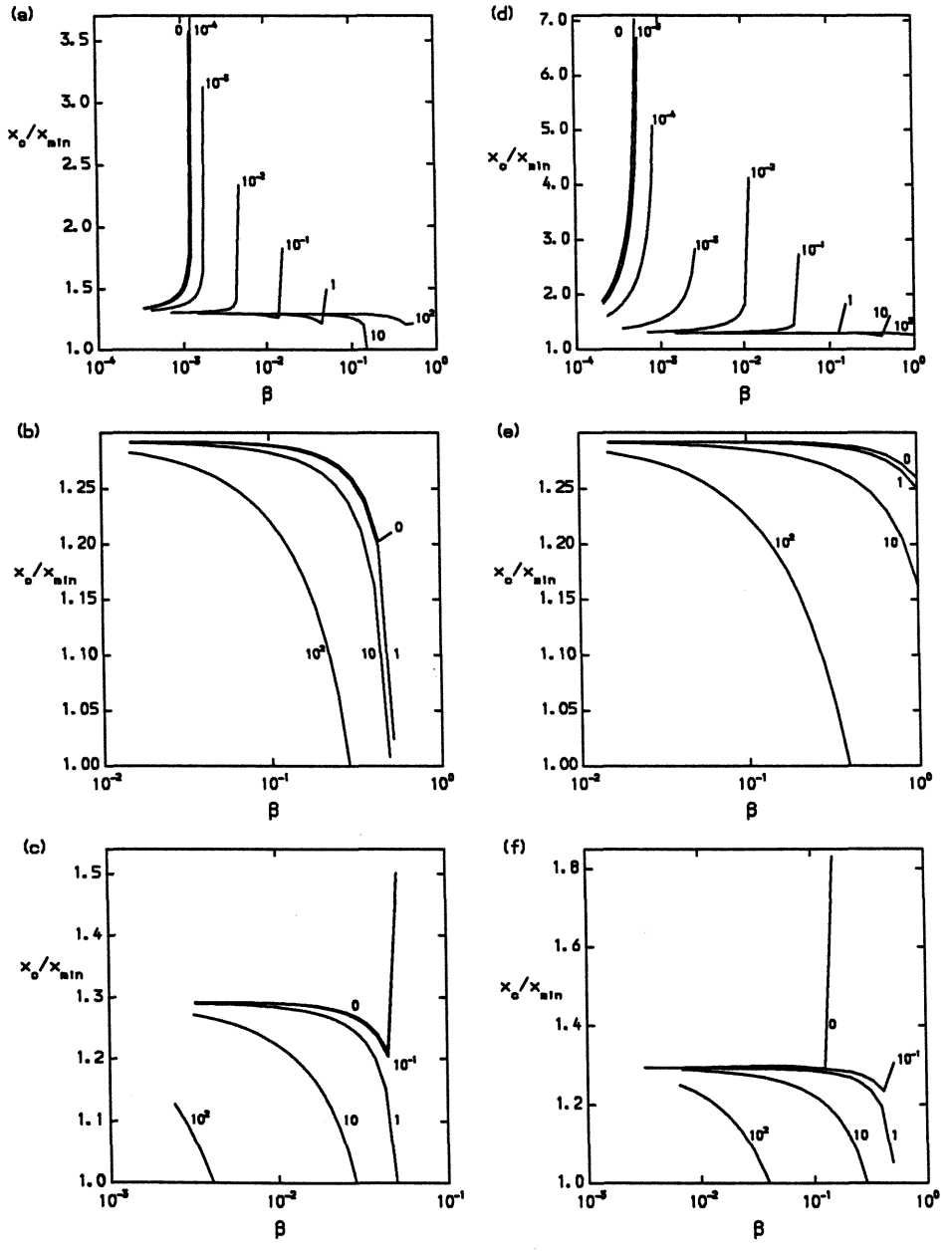

Figure 3.9: x_c/x_{min} against β for the values of ϕ_ϵ, ϕ_m and λ shown in table 3.1.

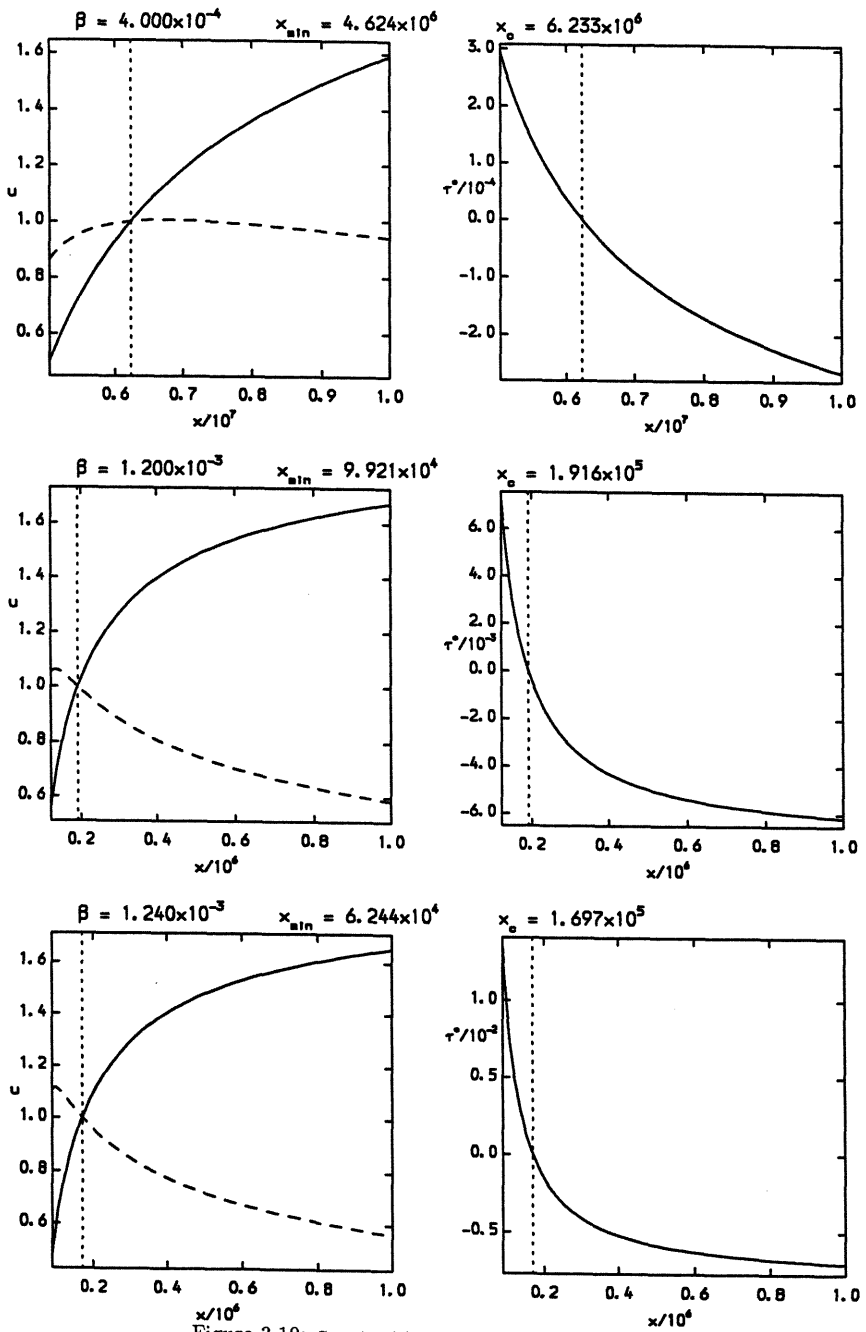

Figure 3.10: Case A. $u(x)$, $u_s(x)$ and $\tau^*(x)$ for various β; $\lambda = 1.0$.

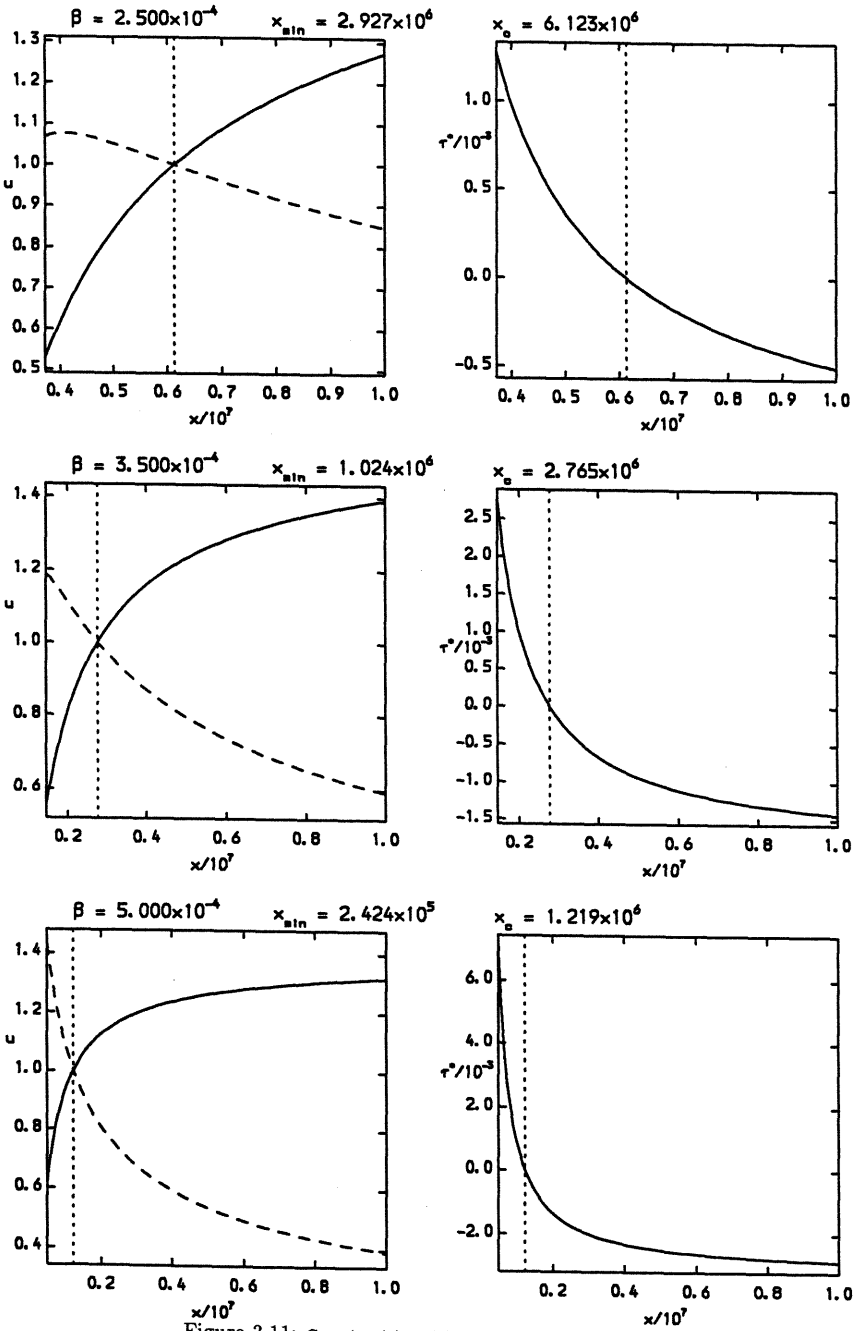

Figure 3.11: Case A. $u(x)$, $u_s(x)$ and $\tau^*(x)$ for various β; $\lambda = 0, 1$.

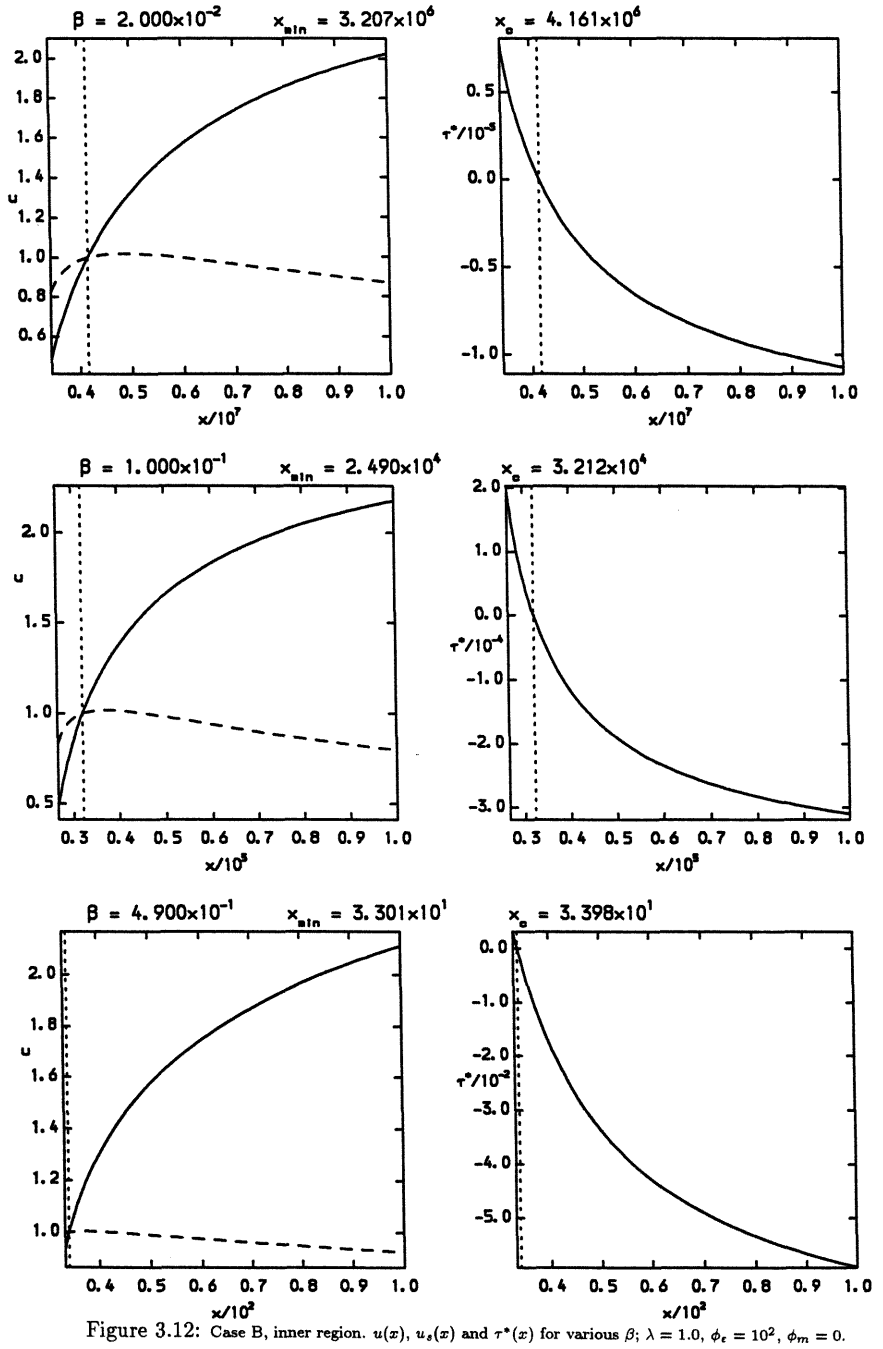

Figure 3.12: Case B, inner region. $u(x)$, $u_s(x)$ and $\tau^*(x)$ for various β; $\lambda = 1.0$, $\phi_r = 10^2$, $\phi_m = 0$.

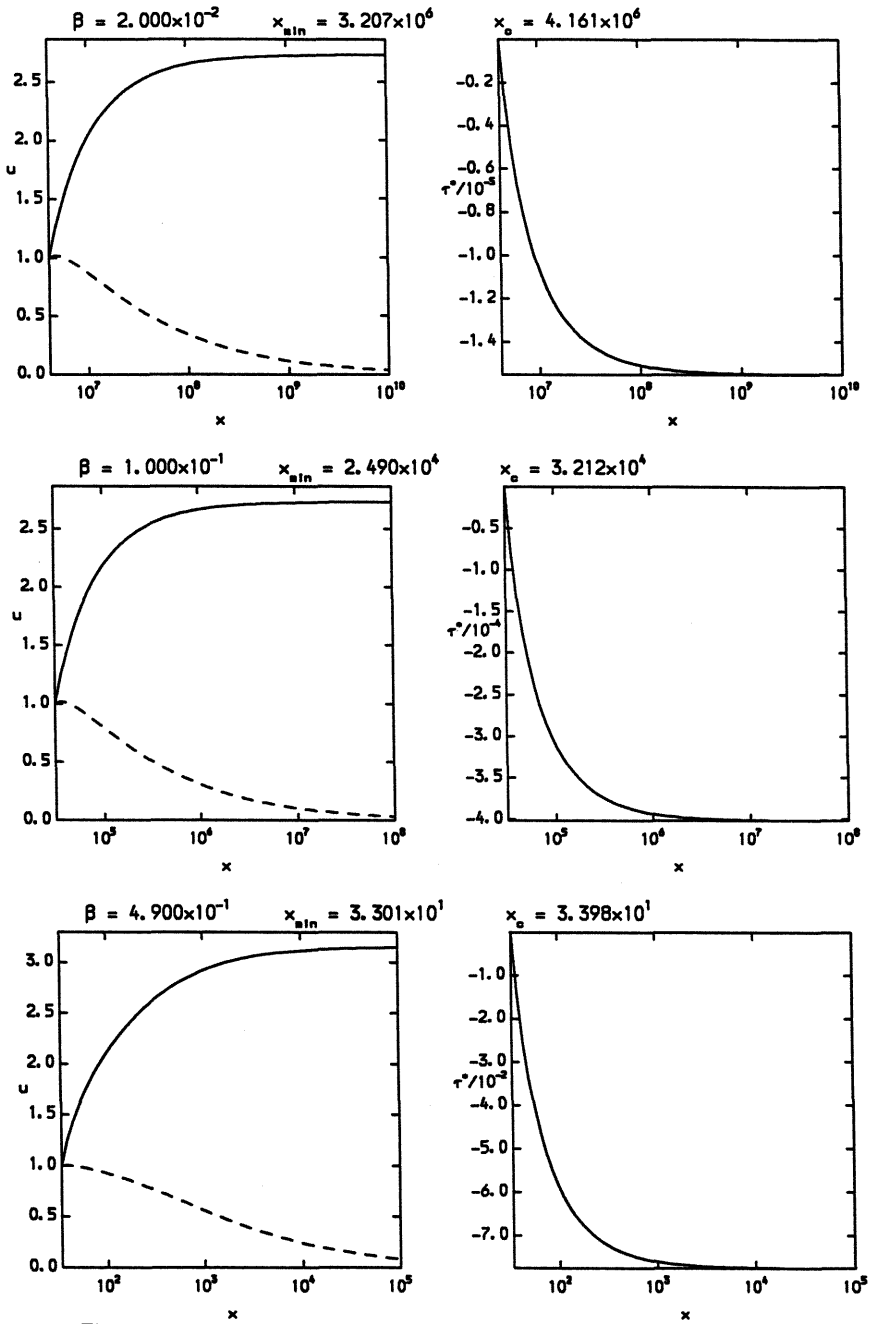

Figure 3.13: Case B, outer region. $u(x)$, $u_s(x)$ and $\tau^*(x)$ for various β; $\lambda = 1.0$, $\phi_\epsilon = 10^2$, $\phi_m = 0$.

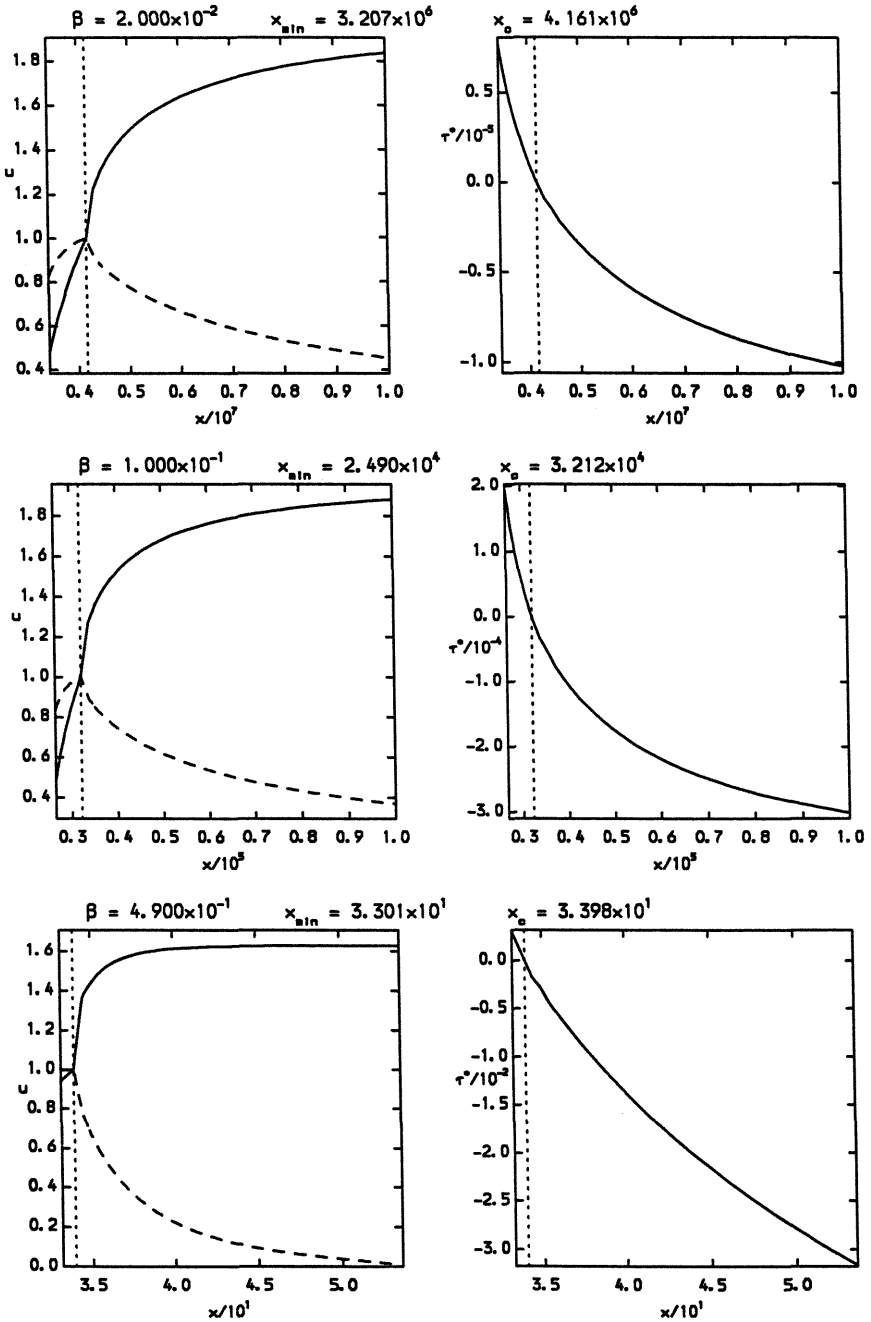

Figure 3.14: Case C, inner region. $u(x)$, $u_s(x)$ and $\tau^*(x)$ for various β; $\lambda = 1.0$, $\phi_c = 10^2$, $\phi_m = 0$.

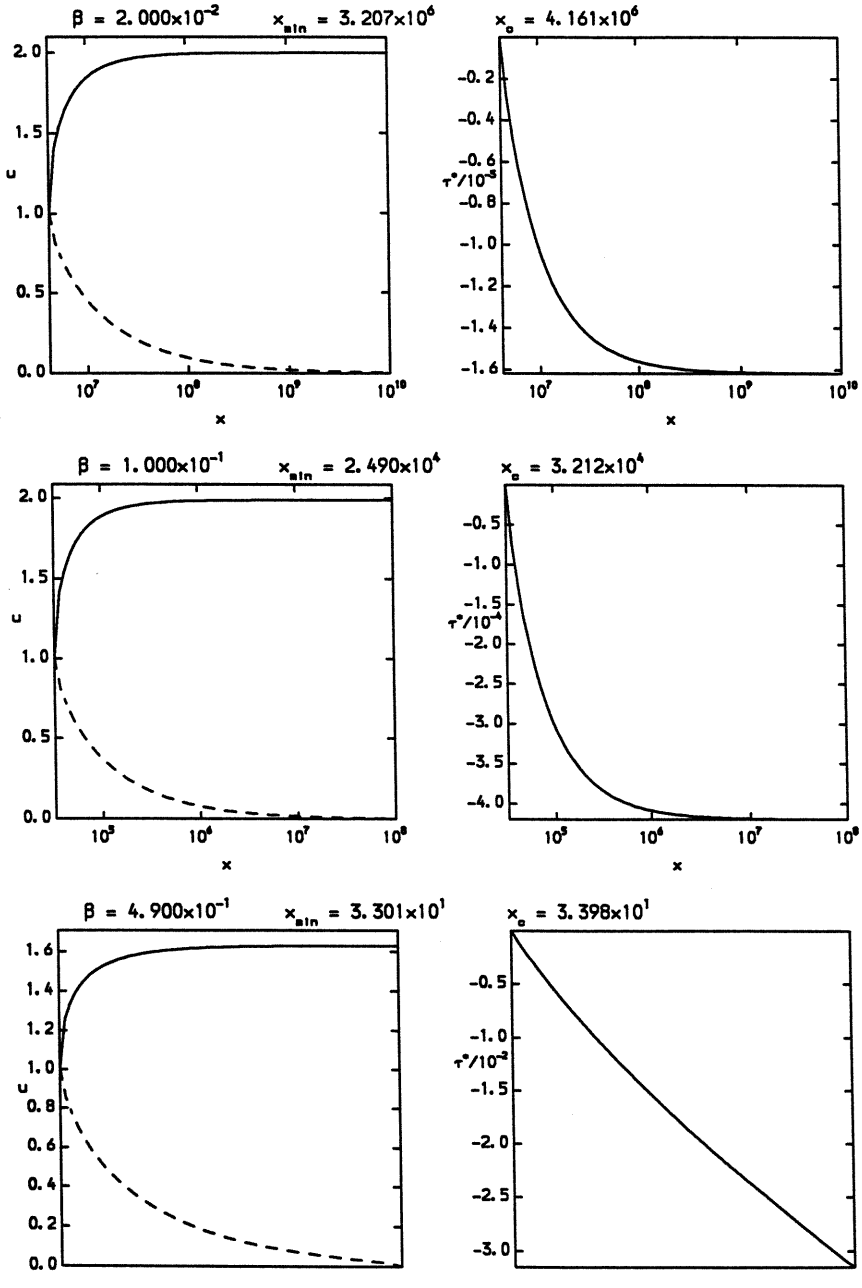

Figure 3.15: Case C, outer region. $u(x)$, $u_s(x)$ and $\tau^*(x)$ for various β; $\lambda = 1.0$, $\phi_\varepsilon = 10^2$, $\phi_m = 0$.

For $\lambda = 1.0$ I find that $\beta \lesssim 10^{-3}$ (equivalent to $T(x_c) = T_s \lesssim 3 \times 10^6$K), $x_c \gtrsim 10^5$ and $x_{min} \gtrsim 5 \times 10^4$. For $\lambda = 0.1$, $\beta \lesssim 5 \times 10^{-4}$ (equivalent to $T_s \lesssim 7 \times 10^5$K), $x_c \gtrsim 10^6$ and $x_{min} \gtrsim 10^5$. At the edge of the cloud $u_s \ll 1$ which implies that transonic solutions can only occur by heating a cold gas to a temperature T_s at x_c that is much less than T_C. There are *no* transonic solutions where $T(x_{min}) = 3.266 \times 10^{12} \beta^2 u_s(x_{min})^2$ is as high as T_C. Forcing the solution to be transonic gives the result that only low temperature winds can form, and these winds are some distance away from the central region.

I therefore recover the well known result that Compton processes alone cannot drive a wind from a gravitationally bound, stationary cloud of gas at the Compton temperature. If, instead of using $u(x_c) = u_s(x_c)$ as the initial conditions, I impose $u(x_{min}) \ll 1$ and $T(x_{min}) \simeq T_C$ at some $x = x_{min}$, the gas would remain subsonic. Alternatively the gas might remain optically thick to x-rays and perhaps be driven out. However, observations of timescales of x-ray variability require the gas to be optically thin except for a small central region.

Note that there is a solution of equations (3.33) and (3.34) such that $T = T_C$ (i.e. when $\theta = \beta^2 u_s^2$). For this to be true we find that the velocity must be zero ($u = 0$) and $\frac{du}{dx} = \frac{du_s}{dx} = 0$ for all x. This is equivalent to having a stationary cloud of gas at the Compton temperature of the radiation. Indeed in Cases B and C this is the solution for $x < x_{min}$ and then extra heating and force is added at x_{min}.

3.9.2 Case B: Injection for all $x > x_{min}$

Some results are given in figures 3.12 and 3.13, which show the functions $u(x)$, $u_s(x)$ and $\tau^*(x)$ for $\lambda = 1.0$ and $\beta = 0.02, 0.1$ and 0.49.

The winds produced are hotter and faster at much smaller radii ($x_{min} < 10^2$) than the Case A winds.

Each set of parameters produces a result that is one of two kinds:

1. $u(x)$ becomes unphysical by plummeting to zero and reaching a negative value at some $x_0 > x_c$.
2. $u_s(x)$ falls asymptotically to zero at large x.

The models where $\phi_m \gtrsim 10\phi_e$ and β is large tend to fall into the first group. For a given ϕ_e, as

ϕ_m increases the point x_0 falls closer to the value for x_c and eventually there is no region above the critical point where the sound speed is positive. The large value of ϕ_m implies that there is a large force on the gas making it expand and therefore cool: here the force is so great that the expansion and cooling occurs much more rapidly than the heating and so the temperature falls to zero. An alternative explanation is that the gas is being accelerated rapidly and therefore needs to acquire some kinetic energy, which must come from the internal (thermal) energy of the gas; the kinetic energy requirement is much greater than the amount of thermal energy available. Choosing a large β means that the wind must move more rapidly, expands more rapidly and therefore cools more rapidly.

The other kind of result where $u_s(x)$ falls asymptotically occurs when the heating is not dominated by the injection of momentum.

The conclusion to be drawn is this: driving a stationary gas to form a hot supersonic wind requires extra heating rather than acceleration. The wind becomes supersonic by expansion and the continual heating prevents the expansion cooling the wind too rapidly.

The Case B results provide part of the answer to why Compton processes alone cannot create hot supersonic winds at small radii: the radiation pressure accelerates the gas too rapidly for the heating to stop the wind cooling by expansion. Because the heating and radiation pressure are linked, increasing the luminosity cannot help. There is an additional effect: as the gas heats up towards T_C, the actual heating rate (proportional to $T_C - T$) falls, making the problem worse. But here, where the gas can be heated without increasing the force, the situation has improved. These results point towards the kind of process that is needed: an interaction where energy is gained by the gas but where there is only a small momentum exchange.

Therefore these results point to a model of the inner region as a stationary cloud of gas at the Compton temperature which is suddenly "kicked" at some radius by injecting heat and momentum. The solutions produced are all such that $u_s(x) < u_s(x_c)$ for all $x < x_c$. In this subsonic region the gas is heated rapidly, so $T(x_c) = T_s >> T_C$. This therefore means that the choice of β is limited so that $T_c = 3.266 \times 10^{12}\beta^2 \gg T_C$, otherwise the solutions do not represent the physical model. In Case A this situation is not possible: $u_s(x < x_c) < u_s(x_c)$, but $T_c < T_C$. Now choosing $\phi_\epsilon > \frac{\lambda\theta}{5\mu}$ ensures that $3.266 \times 10^{12}\beta^2 \gg T_C$. Ignoring cooling by expansion for the moment, it is clear that the gas temperature would reach equilibrium when

$$\left(\frac{\lambda\theta}{5\mu} + \phi_\epsilon\right)\frac{1}{\beta^2 u_s^2} - \frac{\lambda}{5\mu} = 0. \tag{3.66}$$

This is clearly much higher than T_C when $\phi_\epsilon \gg \frac{\lambda\theta}{5\mu}$. Of course this temperature is never reached in practise, because the wind is also cooling by expansion.

Figure 3.16 shows x_{cool} (the point at which the temperature has fallen by a factor 10 from its value at x_c, close to its maximum) as a multiple of x_c. This region extends over a factor greater that 10 in radius provided $\phi_\epsilon \gtrsim 10\phi_m$.

3.9.3 Case C: Injection for $x_{min} < x < x_c$

Some results are given in figures 3.14 and 3.15, which show the functions $u(x)$, $u_s(x)$ and $\tau^*(x)$ for $\lambda = 1.0$ and $\beta = 0.02, 0.1$ and 0.49.

Here the inner region is the same as for Case B. Also the criteria that $\phi_\epsilon > \frac{\lambda\theta}{5\mu}$ and $\phi_m \lesssim 10\phi_\epsilon$ are the same: so that a hot supersonic wind is produced at small radii.

Because all the injection is turned off at x_c the situation at $x > x_c$ is different. Now the wind is Compton driven, and is already supersonic. At these radii the Compton processes become less important and expansion is dominant: the wind coasts away with the temperature falling adiabatically. The cooling is more rapid than for Case B, so the hot region is much smaller. The cooling is not as catastrophic for large ϕ_m and large β as in Case B though there are still values for these parameters where u_s falls to zero.

The temperature falls by a factor 10 over a much smaller region than in Case B, this region extends over a factor of the order of x_c.

3.10 Implications for the two phase model of the BLR

The results of the gas dynamics show that an *extended* high temperature intercloud medium will only be possible if the non-radiative energy injection occurs throughout the broad line region, otherwise the wind cools to below the Compton temperature within a small fraction of r_c. Therefore the extra energy will be injected into the line emitting clouds and this will alter the conditions for two phase equilibrium.

The effects of the extra energy on the clouds was investigated as follows (Raine and O'Reilly, 1993). The photoionisation code "CLOUDY" (Ferland and Rees, 1990) was used to compute

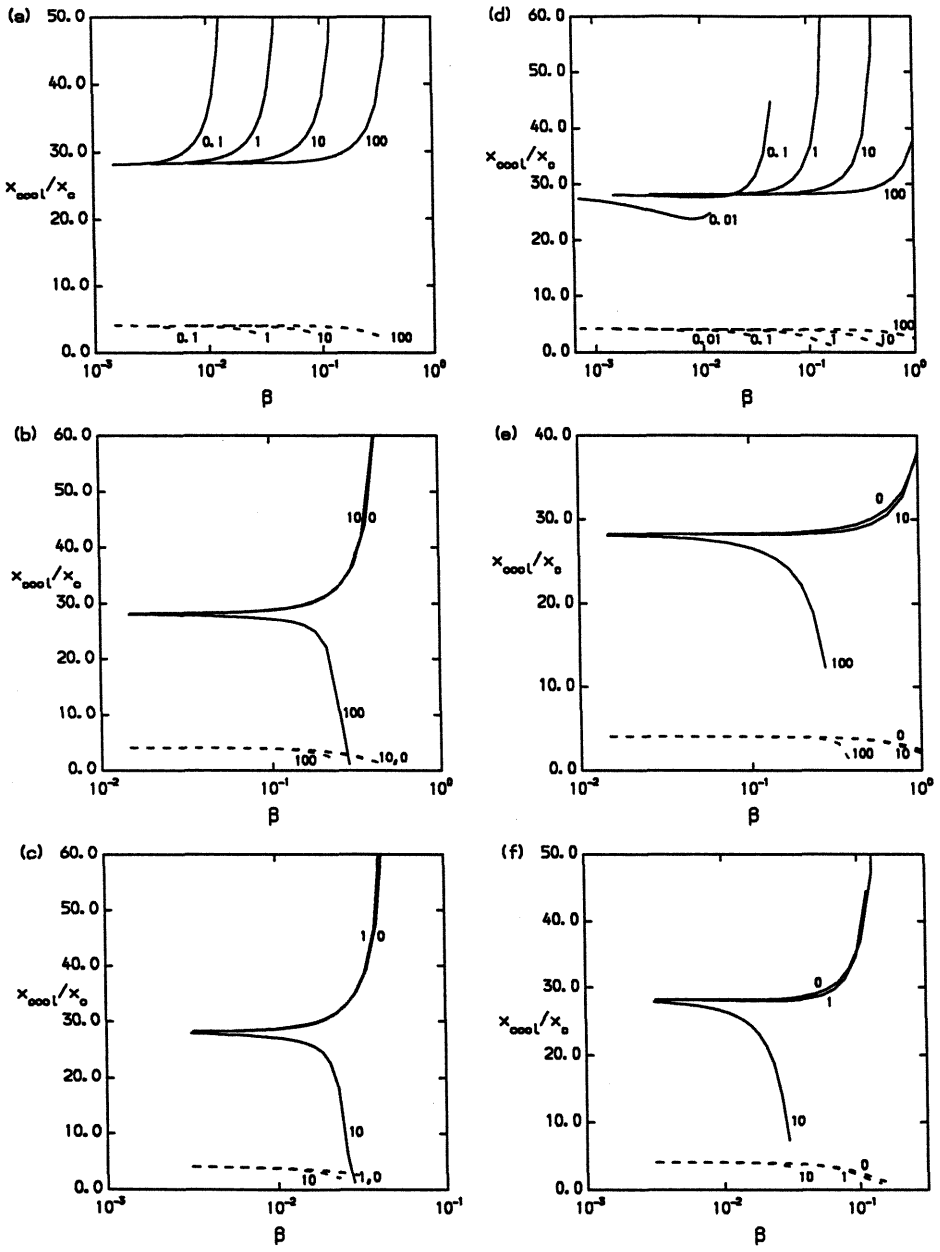

Figure 3.16: x_{cool}/x_c against β for the values of ϕ_ϵ, ϕ_m and λ shown in table 3.1. The solid lines show the results for Case B, the dashed lines show the results for Case C.

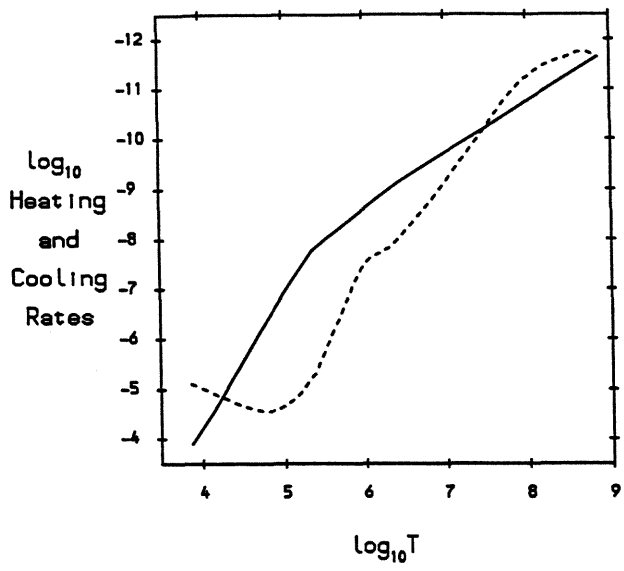

Figure 3.17: Heating rate (dashed line) and cooling rate (solid line) in units of ergs cm^{-3} s^{-1} plotted against temperature for gas with $n_eT = 5 \times 10^{13}$ cm^{-3}.

heating and cooling rates at the face of a plane parallel cloud for a range of densities including the extra energy injection. The average quasar spectrum was used (Mathews and Ferland, 1987), i.e. two phase equilibrium was not possible without this extra heating. Figure 3.17 shows the heating and cooling rates against temperature for a gas in a typical broad line environment at a distance of 10^{18} cm from an ionising source of radiation of 10^{45} ergs s^{-1}. The figure shows rates for gas at a given pressure, obtained by plotting data at constant n_eT, chosen for consistency with the pressure in broad line clouds. The parameter defining the additional energy injection, ϕ_ε, was taken as 100, implying that the non-radiative heating was around 20 times greater than the Compton heating in the low density phase. The figure shows that two stable phases may coexist: a cool phase with a temperature of order 10^4 K and a density of 5×10^9 cm^{-3} and a hot phase at around 10^9 K. I conclude that, in principle, the existence of a non-radiative energy injection in the broad line region allows existence of cool clouds in a hot outflow.

The additional heating must also be taken into account when computing line ratios. However, the actual effect of this addional heating on the line ratios is expected to be minimal. The

extra heating was chosen to dominate Compton heating in the intercloud medium by a factor 20, where it provides the main heating mechanism. In the clouds the main heating comes from photoionisation and neither Compton heating, nor the extra heating have a significant effect. This may be confirmed by direct computation of line ratios. Note, however, that only the direct heating effect of the non-radiative energy injection has been considered: any possible contribution to the ionisation balance has been neglected. The changes to the ionisation balance would depend on the precise nature and the spectrum of the injected energy.

3.11 Discussion

I have shown that spherical supersonic two phase outflow with the properties of the broad line region can exist around an AGN provided there is additional non-radiative heating that injects sufficient energy but not momentum. A thermally driven wind can be generated in this way if ϕ_m/ϕ_ε is constrained such that the dynamical timescale of the wind material is greater than the thermal timescale. This also avoids the problems of a cool wind and the associated but unobserved x-ray absorption. One way of satisfying this constraint is if the extra heating is due to relativistic electrons, possibly associated with leakage from the synchrotron emitting plasma.

Two problems remain. First, the full effects of the ionisation balance in the clouds and the consequences for the line ratios must be investigated. More important is the problem of cloud formation. It is unlikely that the modified heating function will alter the conclusions of Mathews and Doane (1990) who show that the growth time for thermal instabilities in the wind exceeds the crossing time of the broad line region. Thus, though clouds are stable, they cannot be formed in this model of the broad line region and therefore must be injected into the region in some way.

Chapter 4

Wind Generation by the Injection of $e^{\pm}$-Pairs into the Accretion Disc Corona - An Initial Investigation

4.1 Introduction

The accretion disc around a supermasive black hole is widely thought to be the source of the power-law X-ray spectra of active galaxies (Frank, King and Raine, 1992). Such a source cannot be modelled as a thin α-disk (Pringle, 1981) or one of its two temperature variants (Shapiro *et al.*, 1976, Rees *et al.*, 1982) because of the similarity of variability timescales in UV and X-rays. (In the standard disc the UV is produced at large radii with correspondingly longer viscous timescales.) This observation in fact suggests that the UV and X-ray regions are radially co-extensive and that the observed spectrum is providing information of the vertical structure of the disc.

On the other hand, progress has been made in emission models by concentrating on the interaction between radiation and matter under the *assumption* that the energy is injected in some form and without regard to the dynamics of the source material (Guilbert, *et al.*, 1983). A popular model is the $e^{\pm}$-cauldron (Bonometto and Rees, 1971, Guilbert *et al.*, 1983): observed energy fluxes and timescales suggest a production region in which the compactness parameter, $l = \sigma_T L/m_e c^3 R$ is large (> 30). Under these circumstances scattering of γ-rays on soft photons can produce $e^{\pm}$ pairs which annihilate to γ-rays. The whole process is kept going by injection

of pairs (or γ-rays) and a soft photon background. The emergent spectrum, partly reprocessed by reflection from a cold disc, can produce the observed X-ray spectra without violating the observational upper limits on the γ-ray background (Rothschild *et al.*, 1983). Nevertheless, this deduction from the 'observed' compactness to γ-γ scattering assumes spherical symmetry. For a disc geometry, with height H at radius R, the effective l is reduced by H/R and γ-γ scattering is not important.

An at first sight apparently unrelated point is that many quasar models assume a supersonic nuclear outflow. Such an outflow must be optically thin down to $< 10^{14}$ cm, so that electron scattering does not smear out the X-ray variability, and optically thick within the radius at which it attains the escape speed, so that it can contain a significant mass flux. These requirements are readily met if the outflow is from the surface of a disc.

In this chapter I attempt to build a highly simplified model in which these two aspects - the production of the power law X-ray spectrum and the supersonic outflow - are brought together. This should be viewed as an initial investigation of the possible behaviour rather than a finished picture. The model of the vertical structure (at fixed R) of the atmosphere of an accretion disc is described in the following sections. The basic ingredients are a soft photon flux from the geometrically thin optically thick 'filling' of the disc comptonised on $e^{\pm}$-pairs injected into the corona of the disc (by unspecified dissipative processes). The result is a supersonic outflow which is stable only for optical depths of order unity or less. This suggests that the soft photon input may be comptonised to a power law of roughly the right power law form (a slope around -1) (Hardt and Maraschi,1993). Thus the spectrum is driven by the *dynamics* of the model. However, in the simplified form presented here, I do not find any self-sustaining oscillations, so the time dependence is not satisfactory.

4.2 The Physical Model

Consider the inner region of an accretion disc (distance from the central black hole, $R < 10^2 R_g$, where R_g is the Schwarzchild radius). This disc may be some kind of thin disc, or a thick disc; later I shall assume that it is a thin alpha-disc. Above the body of the disc sits an optically thin corona of hot gas in pressure equilibrium with the cooler material below. For simplicity I shall assume a pure hydrogen plasma.

An ultra-violet black body spectrum shines through the corona, the precise mechanism or

location of the generation of this radiation need not be considered here. This spectrum would form the blue bump/soft X-ray excess observed in many sources.

Now, suppose high energy electron-positron pairs are injected into the corona. The mechanism for the production of these pairs is beyond the scope of this discussion, but might perhaps be due to some non-thermal heating processes in the atmosphere of the disc (for example instabilities or shocks), or may be a consequence of the fact that an optically thin corona cannot radiate all the energy generated locally, resulting in local heating and the production of pairs.

As a result of this injection the gas is heated, expands and accelerates away from the disc until the speed is such that the escape velocity is reached and a wind has formed. At large distances the wind will appear as a spherically symmetric outflow from the central region of the active nucleus.

The purpose of the subsequent work is to investigate the broad features of this model, not to produce detailed solutions. I shall examine the long term stability of the system and also the radiation spectrum that one would expect to observe.

The five most important energy exchange processes to consider, the only ones considered here, are:

1. Comptonisation of the UV photons by the electrons in the corona and also by the injected pairs.
2. Inverse Compton cooling of the electrons and positrons.
3. The exchange of energy between the gas and the injected particles.
4. Annihilation of pairs.
5. Creation of pairs.

Momentum is transferred to the gas by radiation pressure, gravity and pressure gradients.

In fact, further investigation will show that the further creation of pairs (beyond the initial input) is negligible, since not enough high energy photons are produced for the process to be important (section 4.9).

I neglect the radial dependence of the disc region under consideration. The region is therefore represented as an effectively one dimensional system: a column of gas with its base situated close to the body of the disc and with its top situated at the point where the gas escapes from the gravitational attraction of the central black hole. The height of the column is represented by the quantity z_{esc}, while the distance of the column from the central black hole is R. As long as $z_{esc} \ll R$ it is sufficient to consider the spatial part of the problem in this way.

I now assume that the total energy introduced into the column is that produced by the dissipation of gravitational energy from the matter accreting onto the central black hole; i.e. all the gravitational energy dissipated at a given radius goes into the atmosphere/corona/wind above the disc at that point.

Rather than representing the electron-positron and photon distributions as continuous functions of energy, these distributions have been split into several components. Consider the electrons and pairs first: the corona consists of a hot gas with the additional injection of high energy pairs. For simplicity I split the electrons and pairs into two separate components each represented entirely by a number density n_a and a temperature T_a. So at the base of the column ($z = z_0 \simeq 0$) the electrons are entirely represented by the coronal component, $n_{e_0} = n_e(z_0)$ and $T_{e_0} = T_e(z_0)$. Throughout the column, mono-energetic pairs are injected at a rate $\dot{n}_+$ with an energy $kT_{\pm_i}$. At any height z the electron and pair distributions are represented by a cool component 'e' with a density n_e and a temperature T_e, and also a hot component '$\pm$' with density $n_\pm$ and temperature $T_\pm$.

It is reasonable to assume that the particles in the cool component will have a thermal distribution; the energy density of a thermal distribution of particles is a simple function of the density and temperature, in this case $U_e = \frac{3}{2} n_e k T_e$. However, the hot component is made up of cooling mono-energetic pairs and some pairs are lost due to annihilation, so it is unlikely that the energy distribution will be anything like thermal. I write the energy density of the hot component as $U_\pm = n_\pm k T_\pm f(T_\pm)$ where this *defines* $T_\pm$, i.e. $T_\pm$ is the temperature the pairs would have if the energy were distributed according to a relativistic thermal distribution. I follow Fukue (1986) by adopting the equation of state derived from the relativistic Maxwell-Boltzmann distribution (Cox and Giuli 1968). For electrons of positrons the energy density function $f(T_\pm)$ is defined

$$f(T_\pm) = 3T + \frac{K_1(m_e c^2/kT\pm)}{K_2(m_e c^2/kT_\pm)}, \tag{4.1}$$

where the K_n's are the modified Bessel functions of second kind of order n. Below, I shall take $f(T_\pm) = 3$, the relativistic limit.

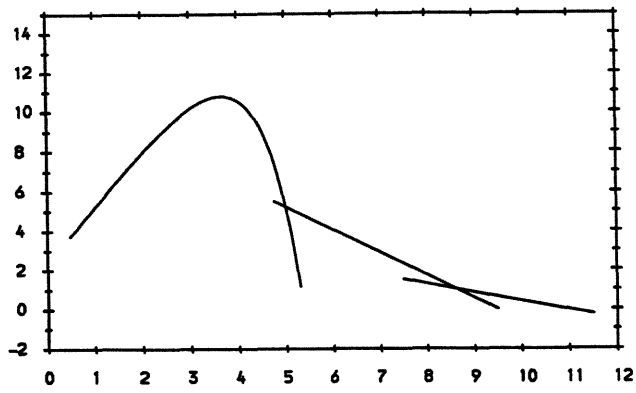

Figure 4.1: An illustration of the assumed output spectrum: a UV black body spectrum (the unprocessed part of the initial spectrum), a soft X-ray power law (from Comptonisation by the cool component) and a hard -ray/γ-ray power law (from Comptonisation by the hot component).

I now consider the radiation spectrum. I assume that the initial spectrum at $z = 0$ can be represented by a black body, with a temperature of $\sim 10^5$ K. The electron and pair distributions have been split into two components, both of which have a temperature hotter than this and so a proportion of UV photons are Comptonised by the hotter electrons. For the purposes of the model I have divided the spectrum into three energy bands: a low energy band where the spectrum is a UV black body, a soft X-ray band and a hard X-ray/γ-ray band. I assume that the spectrum in the two higher energy bands can each be described by a single power law, the index of which is dependant on the density and temperature of one component of the electrons, figure 4.1 illustrates these three spectral components.

4.3 The Basic Equations of the Model

The basic equations that define the model are derived by considering the conservation of matter, momentum and energy as the material flows through the column, using the equations of gas dynamics.

4.3.1 The Conservation of Mass Flux

The equation for the conservation of mass flow in the column is

$$\frac{\partial \rho}{\partial t} + \nabla.(\rho v) = S. \tag{4.2}$$

Here S is the sum of all sources and sinks of mass. Because I have divided the gas into two components it is better to write this conservation law as two equations:

$$\frac{\partial n_e}{\partial t} + \frac{\partial}{\partial z}(n_e v) = 0, \tag{4.3}$$

$$\frac{\partial n_\pm}{\partial t} + \frac{\partial}{\partial z}(n_\pm v) = S_\pm. \tag{4.4}$$

The 'e' population refers to the normal matter, fully ionized hydrogen; the '$\pm$' component refers to the injected matter, the electron positron pairs. The quantity $S_\pm(z,t)$ represents the injection of pairs and the annihilation of pairs, and can be written:

$$S_\pm(z,t) = 2\dot{n}_+ - \frac{1}{2}\sigma_a c n_\pm^2(z,t), \tag{4.5}$$

where $\dot{n}_+$ is the number of positrons injected per unit volume. Note that the number density of electrons *and* positrons in this population is $n_\pm(z,t)$, so the number density of electrons *or* positrons is $\frac{1}{2}n_\pm(z,t)$. Therefore the number of electrons and positrons annihilating per unit time is $2\sigma_a c n_+ n_- = \frac{1}{2}\sigma_a c n_\pm^2$ where σ_a is the annihilation cross section.

4.3.2 The Conservation of Momentum Flux

For momentum I consider the gas as a whole, so there is only the single equation:

$$\frac{\partial}{\partial t}(\rho v) + \frac{\partial}{\partial z}\left(\frac{\rho v^2}{2}\right) = -\frac{\partial p}{\partial z} - \rho g + n\sigma_T p_{rad}. \tag{4.6}$$

Here the mass density $\rho = \rho_e + \rho_\pm = m_p n_e + m_e n_\pm$; the number density $n = n_e + n_\pm$; p is the gas pressure, p_{rad} the radiation pressure and g is the acceleration due to gravity in the z direction.

4.3.3 The Conservation of Energy Flux for the Gas

Again, this is divided into two equations, one representing each component of the gas:

$$\frac{\partial}{\partial t}\left(\frac{\rho_e v^2}{2} + U_e\right) + \frac{\partial}{\partial z}\left(\frac{\rho_e v^3}{2} + U_e v + p_e v\right) = -\rho_e g v + \frac{4 n_e \sigma_T k}{m_e c}(T_C - T_e) U_{rad} \tag{4.7}$$
$$+\sigma_T c k (T_\pm - T_e) n_e n_\pm,$$

$$\frac{\partial}{\partial t}\left(\frac{\rho_{\pm}v^2}{2}+U_{\pm}\right)+\frac{\partial}{\partial z}\left(\frac{\rho_{\pm}v^3}{2}+U_{\pm}v+p_{\pm}v\right)=-\rho_{\pm}gv+\frac{4n_{\pm}\sigma_T k}{m_e c}\left(T_C-T_{\pm}\right)U_{rad} \quad (4.8)$$
$$-\sigma_T ck\left(T_{\pm}-T_e\right)n_e n_{\pm}+2\dot{n}_{+}kT_{\pm_i}-\frac{1}{2}\sigma_a cn_{\pm}^2 kT_{\pm}f\left(T_{\pm}\right),$$

where U_{rad} is the total radiation energy density, $U_{rad} = U_{UV} + U_x + U_\gamma$; T_C is the inverse Compton temperature of the radiation field (chapter 2, equation(2.11). The second term on the right hand side of each equation represents the exchange of energy between the electrons and the radiation. The third term is an estimate of the energy exchange between the two components of electrons due to collisions, based on the equation for two body relativistic collisions between protons and electrons (Stepney and Guilbert 1983). For simplicity I assume that the cross section for this process is a constant of the order of the Thomson cross section. This neglects a temperature dependant factor; I do not expect this to affect my results. The fourth term on the right hand side of (4.8) is the energy added by the injection of pairs at an energy $kT_{\pm_i}$. The fifth term is the energy lost due to pair annihilation.

4.3.4 The Flow of Radiation Energy

The flow of radiation energy is described by three equations, one for each energy band. Consider the equations for the soft X-ray, the hard X-ray/γ-ray and the UV components (energy densities U_x, U_γ and U_{UV}) respectively:

$$\frac{\partial U_x}{\partial t}+\frac{\partial}{\partial z}\left(U_x c\right)=\frac{4n_e\sigma_T k}{m_e c}\left(T_e-T_C\right)U_{rad}, \quad (4.9)$$

$$\frac{\partial U_\gamma}{\partial t}+\frac{\partial}{\partial z}\left(U_\gamma c\right)=\frac{4n_{\pm}\sigma_T k}{m_e c}\left(T_{\pm}-T_C\right)U_{rad}, \quad (4.10)$$

$$\frac{\partial U_{UV}}{\partial t}+\frac{\partial}{\partial z}\left(U_{UV} c\right)=\dot{U}_{UV_0}-\frac{4n_e\sigma_T k}{m_e c}\left(T_e-T_C\right)U_{rad}-\frac{4n_{\pm}\sigma_T k}{m_e c}\left(T_{\pm}-T_C\right)U_{rad}. \quad (4.11)$$

To compute the output spectrum I assume, for simplicity, that the spectrum within the soft X-ray band can be described by a power law and has been formed from UV photons interacting with the cooler of the two electron components, as if the hotter component were not actually present, though any particular photon will have interacted with electrons from both components. I also assume that the spectrum in the hard X-ray/γ-ray band can be described by a power law and has been formed from UV photons interacting with the electrons in the hotter component, as if the cooler component were not present. I estimate the index of this power law using the numerical results obtained by Katz (1976).

In principle, U_γ also contains a contribution from pair annihilation, but the amount of energy generated in this way is relatively small. The photons produced by annihilation are of very high energy: the Klein-Nishina effect reduces the cross section at higher energies, and so the photons are more likely to completely escape from the column, before interacting with any electrons.

4.4 Manipulation of the Equations

I now have a system of eight equations that represent the model (4.3, 4.4, 4.6, 4.7, 4.8, 4.9, 4.10, 4.11), with variables that are functions of height within the column and time. For the purposes of this work, I am interested in the time dependent behaviour and the observed features of the model. Since the emitted spectrum depends on interactions over the whole column, for simplicity I consider the various quantities averaged over height. Therefore, I replace the quantities $n_e(z,t)$, $n_\pm(z,t)$, etc., by $\bar{n}_e(t)$, $\bar{n}_\pm(t)$, etc. The resulting equations are not mathematically identical to the set from which they are obtained, since I am replacing averages of products by products of averages, but the broader features should remain. Thus from equation (4.3) I replace $\frac{\partial n_e}{\partial t}$ with $\frac{d\bar{n}_e}{dt}$ and $\frac{\partial}{\partial z}(n_e v)$ by $\frac{1}{z_{esc}}(\bar{n}_e v_{esc} - n_{e_0} v_0)$ where terms subscripted '0' are the original z dependent functions evaluated at $z = 0$. Barred quantities denote averages over z between $z = 0$ and $z = z_{esc}$ where, as stated above, z_{esc} is the height at which $v = v_{esc}$, the escape velocity, $v_{esc} = \sqrt{\frac{2GM}{R}}$. Equations (4.3) to (4.10) become, respectively:

$$\frac{d\bar{n}_e}{dt} = \frac{n_{e_0} v_0 - \bar{n}_e v_{esc}}{z_{esc}}, \tag{4.12}$$

$$\frac{d\bar{n}_\pm}{dt} = \frac{1}{z_{esc}}\left(2\dot{n}_+ - \frac{1}{2}\sigma_a c \bar{n}_\pm^2 - \bar{n}_\pm v_{esc}\right), \tag{4.13}$$

$$\frac{d}{dt}(\bar{\rho} v_{esc}) + \frac{1}{z_{esc}}\left(\frac{\bar{\rho} v_{esc}^2}{2} - \frac{\rho_0 v_0^2}{2}\right) = \frac{p_0 - \bar{p}}{z_{esc}} - \bar{\rho} g + \sigma_T \bar{n} \bar{p}_{rad}, \tag{4.14}$$

$$\frac{d}{dt}\left(\frac{\bar{\rho}_e v_{esc}^2}{2} + \overline{U}_e\right) + \frac{1}{z_{esc}}\left(\frac{\bar{\rho}_e v_{esc}^3}{2} + \overline{U}_e v_{esc} + \bar{p}_e v_{esc} - \frac{\rho_{e_0} v_0^3}{2} - U_{e_0} v_0 - p_{e_0} v_0\right) = \tag{4.15}$$
$$-\bar{\rho}_e g v_{esc} + \frac{4\bar{n}_e \sigma_T k}{m_e c}\left(\overline{T}_C - \overline{T}_e\right)\overline{U}_{rad} + \sigma_T c k \left(\overline{T}_\pm - \overline{T}_e\right)\bar{n}_e \bar{n}_\pm,$$

$$\frac{d}{dt}\left(\frac{\bar{\rho}_\pm v_{esc}^2}{2} + \overline{U}_\pm\right) + \frac{1}{z_{esc}}\left(\frac{\bar{\rho}_\pm v_{esc}^3}{2} + \overline{U}_\pm v_{esc} + \bar{p}_\pm v_{esc}\right) = \tag{4.16}$$
$$-\bar{\rho}_\pm g v_{esc} + 2\dot{n}_+ k T_{\pm_i} - \frac{\sigma_a c \bar{n}_\pm^2}{2} k \overline{T}_\pm f\left(\overline{T}_\pm\right)$$
$$+\frac{4\bar{n}_\pm \sigma_T k}{m_e c}\left(\overline{T}_C - \overline{T}_\pm\right)\overline{U}_{rad} - \sigma_T c k \left(\overline{T}_\pm - \overline{T}_e\right)\bar{n}_e \bar{n}_\pm,$$

$$\frac{d\overline{U}_x}{dt} = \frac{4\bar{n}_e\sigma_T k}{m_e c}\left(\overline{T}_e - \overline{T}_C\right)\overline{U}_{rad} - \frac{\overline{U}_x c}{z_{esc}}, \tag{4.17}$$

$$\frac{d\overline{U}_\gamma}{dt} = \frac{4\bar{n}_\pm\sigma_T k}{m_e c}\left(\overline{T}_\pm - \overline{T}_C\right)\overline{U}_{rad} - \frac{\overline{U}_\gamma c}{z_{esc}}, \tag{4.18}$$

$$\frac{d\overline{U}_{UV}}{dt} = \dot{U}_{UV_0} - \frac{4\sigma_T k}{m_e c}\left[n_e\left(\overline{T}_e - \overline{T}_C\right) + n_\pm\left(\overline{T}_\pm - \overline{T}_C\right)\right]\overline{U}_{rad} - \frac{\overline{U}_{UV}c}{z_{esc}}. \tag{4.19}$$

Here $\overline{U}_e = \frac{3}{2}\bar{n}_e k\overline{T}_e$ and $\overline{U}_\pm = \bar{n}_\pm k\overline{T}_\pm f(\overline{T}_\pm)$ and also $z = z_{esc}$.

I evaluate z_{esc} using (4.14):

$$z_{esc} = \frac{\left(\bar{n}_e + \mu\bar{n}_\pm\right)v_{esc}^2 + n_{e_0}v_0^2 - 2n_{e_0}v_{esc}v_0 + \frac{2k}{m_p}\left(n_{e_0}T_{e_0} - \bar{n}_e\overline{T}_e - \bar{n}_\pm\overline{T}_\pm\right)}{2\left[g\left(\bar{n}_e + \mu\bar{n}_\pm\right) - \left(\bar{n}_e + \bar{n}_\pm\right)\overline{U}_{rad}\frac{\sigma_T}{3m_p} - \frac{1}{2}\sigma_a c\bar{n}_\pm^2\mu v_{esc} + 2\dot{n}_+\mu v_{esc}\right]}, \tag{4.20}$$

where $\mu = m_e/m_p$. Hence equations (4.15) and (4.16) can be manipulated to give:

$$\begin{aligned} 3z_{esc}\frac{\bar{n}_e k}{m_p}\frac{d\overline{T}_e}{dt} &= n_{e_0}v_0^3 - n_{e_0}v_0v_{esc}^2 + \frac{5k}{m_p}T_{e_0}n_{e_0}v_0 \\ &\quad -\frac{3k}{m_p}\overline{T}_e n_{e_0}v_0 - \frac{2k}{m_p}\overline{T}_e\bar{n}_e v_{esc} - 2g\bar{n}_e v_{esc}z_{esc} \\ &\quad -2\bar{n}_e z_{esc}\frac{4\sigma_T k}{m_e m_p c}\left(\overline{T}_e - \overline{T}_C\right)\overline{U}_{rad} \\ &\quad +2\bar{n}_e\bar{n}_\pm\left(\overline{T}_\pm - \overline{T}_e\right)\frac{\sigma_T kc}{m_e}z_{esc}, \end{aligned} \tag{4.21}$$

$$\begin{aligned} 6z_{esc}\frac{\bar{n}_\pm k}{m_p}\frac{dT_\pm}{dt} &= \frac{1}{2}\sigma_a c\bar{n}_\pm^2 z_{esc}v_{esc}^2\mu - 2\dot{n}_+ z_{esc}v_{esc}^2\mu \\ &\quad -\frac{2k}{m_p}\left(\overline{T}_\pm v_{esc}\bar{n}_\pm - 6\dot{n}_+T_{\pm_i}z_{esc} + 6\dot{n}_+\overline{T}_\pm z_{esc}\right) - 2z_{esc}\mu g v_{esc}\bar{n}_\pm \\ &\quad -2\bar{n}_\pm z_{esc}\frac{4\sigma_T k}{m_e m_p c}\left(\overline{T}_\pm - \overline{T}_C\right)\overline{U}_{rad} - 2\bar{n}_e\bar{n}_\pm\left(\overline{T}_\pm - \overline{T}_e\right)\frac{\sigma_T kc}{m_e}z_{esc}. \end{aligned} \tag{4.22}$$

Energy is introduced into the column of gas in four forms: ultra-violet radiation, injection of high energy pairs, and the thermal and kinetic energy of the ionised hydrogen entering the column through its base. The total energy flux into the column is:

$$F_{TOT} = F_{UV_0} + n_{e_0}v_0kT_{e_0} + \frac{1}{2}n_{e_0}v_0^3m_p + 2\dot{n}_+kT_{\pm_i}z_{esc}. \tag{4.23}$$

The flux of UV radiation into the column is

$$F_{UV_0} = \dot{U}_{UV_0}z_{esc}. \tag{4.24}$$

Rearranging equation (4.23) gives

$$\dot{U}_{UV} = \frac{1}{z_{esc}}\left(F_{TOT} - n_{e_0}v_0kT_{e_0} - \frac{1}{2}n_{e_0}v_0^3m_p - 2\dot{n}_+kT_{\pm_i}z_{esc}\right). \tag{4.25}$$

Now equation (4.23) becomes:

$$\frac{d\overline{U}_{UV}}{dt} = \frac{1}{z_{esc}}\left(F_{TOT} - n_{e_0}v_0 kT_{e_0} - \frac{1}{2}n_{e_0}v_0^3 m_p - \overline{U}_{UV}c\right) - 2\dot{n}_+ kT_{\pm_i} \\ -\frac{4\sigma_T k}{m_e c}\left[\bar{n}_e\left(\overline{T}_e - \overline{T}_C\right) + \bar{n}_\pm\left(\overline{T}_\pm - \overline{T}_C\right)\right]\overline{U}_{rad}. \tag{4.26}$$

I now have a set of seven ordinary differential equations describing the functions $\bar{n}_e(t)$, $\bar{n}_\pm(t)$, $\overline{T}_e(t)$, $\overline{T}_\pm(t)$, $\overline{U}_x(t)$, $\overline{U}_\gamma(t)$ and $\overline{U}_{UV}$. There are also seven free parameters: v_0, v_{esc}, n_{e_0}, T_{e_0}, $\dot{n}_+$, $T_{\pm_i}$ and F_{TOT}. It is a fairly trivial matter to integrate the equations using a numerical method from some arbitrary starting point, but what should the starting point be? With a seven dimensional vector for the starting point and an additional seven numbers to chose, the topography of the solution will be incredibly complicated. To examine the broader features of the model, this system of equations needs to be simplified, I define a set of dimensionless quantities and rewrite equations (4.12), (4.13), (4.17) to (4.22) and (4.26).

I first define the following variables:

$$\begin{aligned} y_1(x) &= \frac{\bar{n}_e(t)}{n_{e_0}}, \\ y_2(x) &= \frac{\bar{n}_\pm(t)}{n_{e_0}}, \\ y_3(x) &= \frac{\overline{T}_e(t)}{T_{e_0}}, \\ y_4(x) &= \frac{\overline{T}_\pm(t)}{T_{e_0}}, \\ y_5(x) &= \frac{\overline{U}_x(t)}{kT_{e_0}n_{e_0}}, \\ y_6(x) &= \frac{\overline{U}_\gamma(t)}{kT_{e_0}n_{e_0}}, \\ y_7(x) &= \frac{\overline{U}_{UV}(t)}{kT_{e_0}n_{e_0}}, \\ x &= \sigma_T n_{e_0} v_{esc} t. \end{aligned} \tag{4.27}$$

I also define the following constants:

$$\begin{aligned} \varepsilon &= \frac{F_{TOT}}{n_{e_0}kT_{e_0}v} \simeq 10\left(\frac{n_{e_0}}{10^{10}\ \mathrm{cm}^{-3}}\right)^{-1}\left(\frac{T_{e_0}}{10^8\ \mathrm{K}}\right)^{-1}\left(\frac{R}{10^2 R_g}\right)^{-\frac{5}{2}}\left(\frac{M}{10^8 M_\odot}\right), \\ \lambda_1 &= \frac{kT_{e_0}}{m_p v_{esc}^2} \simeq 10^{-3}\left(\frac{T_{e_0}}{10^8\ \mathrm{K}}\right)\left(\frac{R}{10^2 R_g}\right), \\ \lambda_2 &= \frac{g}{\sigma_T n_{e_0} v_{esc}^2} \simeq 2.5\times 10^{-3}\left(\frac{n_{e_0}}{10^{10}\ \mathrm{cm}^{-3}}\right)^{-1}\left(\frac{M}{10^8 M_\odot}\right)^{-1}, \\ \lambda_3 &= \frac{v_0}{v_{esc}} \simeq 3\times 10^{-2}\left(\frac{v_0}{10^8\ \mathrm{cm\,s}^{-1}}\right)\left(\frac{R}{10^2 R_g}\right)^{\frac{1}{2}}, \end{aligned}$$

$$
\begin{aligned}
\lambda_4 &= \frac{\overline{T}_{IC}}{T_{e_0}} \simeq 10^{-3}\left(\frac{\overline{T}_C}{10^5\ \mathrm{K}}\right)\left(\frac{T_{e_0}}{10^8\ \mathrm{K}}\right)^{-1}, \qquad (4.28)\\
\lambda_5 &= \frac{T_{\pm_i}}{T_{e_0}} \simeq 10^2\left(\frac{T_{\pm_i}}{10^{10}\ \mathrm{K}}\right)\left(\frac{T_{e_0}}{10^8\ \mathrm{K}}\right)^{-1},\\
\beta &= \frac{v_{esc}}{c} \simeq 0.1\left(\frac{R}{10^2 R_g}\right)^{-\frac{1}{2}},\\
\zeta &= \sigma_T n_{e_0} z_{esc} \simeq 6\times 10^{-3}\left(\frac{n_{e_0}}{10^{10}\ \mathrm{cm}^{-3}}\right)\left(\frac{z_{esc}}{10^{12}\ \mathrm{cm}}\right),\\
q &= \frac{2\dot{n}_+}{\sigma_T n_{e_0}^2 v_{esc}} \simeq \left(\frac{\dot{n}_+}{10^5\ \mathrm{cm}^{-3}\mathrm{s}^{-1}}\right)\left(\frac{n_{e_0}}{10^{10}\ \mathrm{cm}^{-3}}\right)^{-2}\left(\frac{R}{10^2 R_g}\right)^{\frac{1}{2}}.
\end{aligned}
$$

The estimated value of the constant ε comes from considering the likely value of F_{TOT}. A typical luminosity for an AGN is $\sim 10^{46}\ \mathrm{erg\,s^{-1}}$ for a cental black hole has a mass $\sim 10^8 M_\odot$. The flux F of radiation at a distance R from a source of luminosity L is

$$F = \frac{L}{4\pi R^2}. \qquad (4.29)$$

Writing the luminosity as

$$L = 10^{46}\left(\frac{M}{10^8 M\odot}\right)\ \mathrm{erg\,s^{-}1}, \qquad (4.30)$$

and R in units of R_g, the total flux of energy into the column is

$$F_{TOT} \simeq 10^{11}\left(\frac{R}{10^2 R_g}\right)^{-2}\left(\frac{M}{10^8 M\odot}\right). \qquad (4.31)$$

The escape velocity $v_{esc} = \sqrt{\frac{2GM}{R}}$ and the Schwarzchild radius $R_g = \frac{2GM}{c^2}$, so I write

$$\frac{v_{esc}}{c} = \sqrt{\frac{R_g}{R}}. \qquad (4.32)$$

To estimate a value for λ_2 consider the acceleration due to gravity in the z direction, g:

$$g \simeq \frac{GM}{R^2}\left(\frac{z_{esc}}{R}\right) = \frac{R_g c}{2R^2}\left(\frac{z_{esc}}{R}\right). \qquad (4.33)$$

To estimate $(\frac{z_{esc}}{R})$ I assume that the disc is an α-disc. The height H of an α-disc at a radius R is given by (Frank, King and Raine, 1992)

$$\frac{H}{R} \simeq 2.3\times 10^{-3}\alpha^{-\frac{1}{10}}\left(\frac{\dot{M}}{10^{20}\ \mathrm{g\,s^{-1}}}\right)^{\frac{3}{20}}\left(\frac{M}{10^8 M_\odot}\right)^{-\frac{3}{8}}\left(\frac{R}{10^{15}\ \mathrm{cm}}\right)^{\frac{1}{8}}. \qquad (4.34)$$

Assumming $z_{esc} \ll R$, I also assume that $\frac{z_{esc}}{R} \simeq \frac{H}{R}$, and so $(\frac{z_{esc}}{R}) \sim 10^{-3}$.

The equations (4.12), (4.13) and (4.17) to (4.22) become:

$$\frac{dy_1}{dx} = \frac{\lambda_3 - y_1}{\zeta}, \tag{4.35}$$

$$\frac{dy_2}{dx} = q - \frac{y_2}{\zeta} - \frac{y_2^2}{2\beta}\left(\frac{\sigma_a}{\sigma_T}\right), \tag{4.36}$$

$$\zeta = \frac{\mu y_2 + \lambda_3^2 - 2\lambda_3 + y_1 + 2\lambda_1(1 - y_1 y_3 + y_2 y_4)}{2\lambda_2(y_1 + \mu y_2) - \frac{2}{3}\lambda_1(y_1 + y_2)(y_7 + y_5 + y_6) - \left(\frac{\sigma_a}{\sigma_T}\right)\frac{\mu}{\beta}y_2^2 + \mu q}, \tag{4.37}$$

$$\frac{dy_3}{dx} = \frac{\lambda_3^2(\lambda_3 - \lambda_1)}{3\zeta\lambda_1 y_1} + \frac{5\lambda_3(1 - y_3)}{3\zeta y_1} - \frac{2\lambda_2\lambda_3}{3\lambda_1 y_1} - \frac{8\beta\lambda_1\lambda_3}{3\mu y_1}(y_7 + y_5 + y_6) + \frac{2y_2\lambda_3(y_4 - y_3)}{3\mu\beta y_1}, \tag{4.38}$$

$$\frac{dy_4}{dx} = \left(\frac{\sigma_a}{\sigma_T}\right)\frac{\mu y_2}{4\beta\lambda_1} - \frac{y_4}{\zeta} + \frac{q}{y_2}\left(3\lambda_5 - 3y_4 - \frac{\mu}{2\lambda_1}\right) - \frac{\mu\lambda_2}{\lambda_1} - \frac{4\beta\lambda_1}{\mu}(y_4 - \lambda_4)(y_7 + y_5 + y_6) - \frac{y_1}{\mu\beta}(y_4 - y_3), \tag{4.39}$$

$$\frac{dy_5}{dx} = \frac{4\beta\lambda_1 y_1}{\mu}(y_3 - \lambda_4)(y_7 + y_5 + y_6) - \frac{y_5}{\zeta\beta}, \tag{4.40}$$

$$\frac{dy_6}{dx} = \frac{4\beta\lambda_1 y_2}{\mu}(y_4 - \lambda_4)(y_7 + y_5 + y_6) - \frac{y_6}{\zeta\beta}, \tag{4.41}$$

$$\frac{dy_7}{dx} = \frac{1}{\zeta}\left[\varepsilon - \lambda_3\left(1 + \frac{\lambda_3^2}{2\lambda_1}\right) - \frac{y_7}{\beta}\right] - q\lambda_5 - \frac{4\lambda_1\beta}{\mu}\left[y_1(y_3 - \lambda_4) + y_2(y_4 - \lambda_4)\right](y_7 + y_5 + y_6). \tag{4.42}$$

Reduction of the Equations to Show the Important Terms

I now examine the equations to determine the important terms. Equation (4.35) clearly shows that as $x \to \infty$, $y_1 \to \lambda_3$. Examining the estimate of the value of λ_3 shows that $y_1 \ll 1$. Equation (4.36) shows that for estimated values of the constants ζ, q and β (with $\sigma_a = \sigma_T$) as $x \to \infty$, y_2 must have a value of the order of unity. So it is valid to assume that $y_1 \ll y_2$.

Examination of equation (4.38), with suitable values for the constants, tends to show that y_3 will increase and decrease with y_4, but with y_3 always less then y_4.

Looking at equation (4.40) in the steady state

$$y_1 y_3(y_7 + y_5 + y_6) = \frac{5y_5}{\zeta}, \tag{4.43}$$

assuming that $\frac{\beta\lambda_1}{\mu} \simeq 1$ and $\beta \simeq \frac{1}{5}$. Also $y_4 \gg \lambda_4$. Rearranging to isolate y_5:

$$\frac{y_5}{y_7 + y_6} = \frac{1}{\frac{5}{\zeta y_1 y_3} - 1}. \tag{4.44}$$

Now $y_1 = \lambda_3 \ll 1$, $\zeta \sim 1$ and $y_3 \sim 1$: this is because ζ is a measure of optical depth, which is likely to be near unity. Also y_3 will tend towards unity (or less) because of the balance

between the electrons cooling due to Compton processes and the transfer of energy from the hotter pairs. This implies $y_5 \ll y_7 + y_6$, i.e. the soft X-ray component is unimportant when compared with the hard X-ray/γ-ray component.

As expected, the important features are due to the injection of hot pairs and the presence of the cooler matter is relatively unimportant. Now consider equation (4.37). Ignoring the smaller terms

$$\zeta = \frac{2\lambda_1 (1 - y_2 y_4) + \mu y_2 - \lambda_3}{\mu q - \frac{2}{3}\lambda_1 y_2 (y_7 + y_6)}. \tag{4.45}$$

In the numerator of (4.45) there is a positive term, μy_2, and a negative term, $2\lambda_1(1 - y_2 y_4) - \lambda_3$, (negative since $y_2 \sim 1$ and $y_4 \gg 1$). In the denominator there is a positive term, μq, and a negative term, $\frac{2}{3}\lambda_1 y_2 (y_7 + y_6)$. Each of these terms is of similar order of magnitude, so I could write ζ as

$$\zeta = \frac{y_2}{q} \text{ or } \zeta = \frac{3y_4}{y_7 + y_6}. \tag{4.46}$$

Choosing $\zeta = \frac{y_2}{q}$ and substituting into equation (4.36) gives the equation

$$\frac{dy_2}{dx} = -\frac{y_2^2}{2\beta}\left(\frac{\sigma_a}{\sigma_T}\right), \tag{4.47}$$

i.e. $y_2 \to 0$ as $x \to \infty$. This removes what must be an important term: the pair injection rate q; in fact equation (4.47) represents the decay of an initial population of pairs by annihilation. The pair injection is the whole basis of the model, so using equation (4.47) reduces (4.36) to an inappropriate form. Hence I have chosen the second approximation in equation (4.46):

$$\zeta = \frac{3y_4}{y_7 + y_6}. \tag{4.48}$$

I shall briefly investigate the validity of this assumption in section 4.10.

From the estimated typical values for the constants (equation (4.28)), it is clear that:

$$\lambda_3 \left(1 + \frac{\lambda_3^2}{2\lambda_1}\right) \ll \varepsilon - \frac{y_7}{\beta}. \tag{4.49}$$

where I assume that F_{TOT} is due to dissipation of gravitational energy in a thin α-disc:

$$F_{TOT} = \frac{3GM\dot{M}}{8\pi R^3}. \tag{4.50}$$

Using the assumptions $y_1 \ll y_2$; $y_3 \ll y_4$; $y_5 \ll y_7 + y_6$ and equation (4.49) the system is reduced to four equations, with four functions of time, representing the pair density, the pair

temperature, the hard X-ray/γ-ray energy density and the UV energy density:

$$\frac{dy_2}{dx} = q - \frac{y_2}{\zeta} - \frac{y_2^2}{2\beta}, \tag{4.51}$$

$$\frac{dy_4}{dx} = \frac{3q}{y_2}(\lambda_5 - y_4) - 4y_4(y_7 + y_6), \tag{4.52}$$

$$\frac{dy_6}{dx} = 4y_2y_4(y_7 + y_6) - \frac{y_6}{\zeta\beta}, \frac{dy_7}{dx} = \frac{\varepsilon}{\zeta} - \frac{y_7}{\zeta\beta} - q\lambda_5 - 4y_2y_4(y_7 + y_6) \tag{4.53}$$

and ζ is defined by equation (4.48). Equation (4.52) comes from (4.39): the first two terms on the right hand side of (4.39) are of the same magnitude and will therefore tend to cancel one another out. The gravity term (λ_2) is small since $z_{esc} \ll R$, as is the recoil term $\frac{y_1}{\mu\beta}(y_4 - y_3)$ when compared to the other terms in the equation (the main result of the recoil term is so that y_3 tracks the value of y_4, so I assume that equation (4.38) is unimportant).

The very complicated system of equations (4.35) to (4.41) has now been reduced to the four equations:

$$\begin{aligned}
\frac{dy_2}{dx} &= q - \frac{y_2(y_7 + y_6)}{3y_4} - \frac{y_2^2}{2\beta}, \\
\frac{dy_4}{dx} &= \frac{3q}{y_2}(\lambda_5 - y_4) - 4y_4(y_7 + y_6), \\
\frac{dy_6}{dx} &= 4y_2y_4(y_7 + y_6) - \frac{y_6(y_7 + y_6)}{3y_4\beta}, \\
\frac{dy_7}{dx} &= \frac{y_7 + y_6}{3y_4}\left(\varepsilon - \frac{y_7}{\beta}\right) - q\lambda_5 - 4y_2y_4(y_7 + y_6),
\end{aligned} \tag{4.54}$$

with four free parameters: q, the pair injection rate; β, the escape velocity in units of the speed of light; λ_5, the ratio of the pair injection temperature to the electron temperature at $z = 0$; and ε, which is the ratio of the total available energy to the thermal energy of the electrons at $z = 0$.

4.5 The Effect of the Medium on the Rate of Injection

I now consider ways in which the pair injection may be modulated by the conditions in the gas. I assume that the pair injection rate depends on the local pressure in the column. There are many ways in which q can depend on the gas pressure or the radiation pressure, but I have chosen three. Firstly, I look at a system where the injection rate is constant; secondly, I assume that the injection rate is proportional to the gas pressure; finally I assume that the injection rate is proportional to the local radiation pressure; i.e. there are three systems:

I $q = Q_I$ = constant.

II $q = Q_{II} y_2 y_4$.

III $q = Q_{III} y_6$.

System I

Examination of the equations (4.54) suggests the following substitutions: $y_2 = u\sqrt{Q_I}$, $y_4 = v$, $y_6 = w\sqrt{Q_I}$, $y_7 = p\sqrt{Q_I}$, $\varepsilon = E\sqrt{Q_I}$ and $x = \frac{t}{\sqrt{Q_I}}$ (where p, u, v, w, and t are dimensionless quantities representing the mean pair density, temperature, the photon energy density and time, respectively, and are not in any way related to p, v and t used earlier).

With these substitutions equations (4.54) become:

$$\begin{aligned}
\frac{du}{dt} &= 1 - \frac{u(p+w)}{3v} - \frac{u^2}{2\beta}, \\
\frac{dv}{dt} &= \frac{3(\lambda_5 - v)}{u} - 4v(p+w), \\
\frac{dw}{dt} &= 4uv(p+w) - \frac{w}{3v\beta}(p+w), \\
\frac{dp}{dt} &= \frac{p+w}{3v}\left(E - \frac{p}{\beta}\right) - \lambda_5 - 4uv(p+w).
\end{aligned} \tag{4.55}$$

System II

Replacing q and substituting $y_2 = uQ_{II}$, $y_4 = v$, $y_6 = wQ_{II}$, $y_7 = pQ_{II}$, $\varepsilon = EQ_{II}$ and $x = \frac{t}{Q_{II}}$ I find that equations (4.54) become

$$\begin{aligned}
\frac{du}{dt} &= uv - \frac{u(p+w)}{3v} - \frac{u^2}{2\beta}, \\
\frac{dv}{dt} &= 3v(\lambda_5 - v) - 4v(p+w), \\
\frac{dw}{dt} &= 4uv(p+w) - \frac{w}{3v\beta}(p+w), \\
\frac{dp}{dt} &= \frac{p+w}{3v}\left(E - \frac{p}{\beta}\right) - uv\lambda_5 - 4uv(p+w).
\end{aligned} \tag{4.56}$$

System III

Replacing q and substituting $y_2 = uQ_{III}$, $y_4 = v$, $y_6 = wQ_{III}$, $y_7 = pQ_{III}$, $\varepsilon = EQ_{III}$ and $x = \frac{t}{Q_{III}}$ I find that equations (4.54) become

$$\frac{du}{dt} = w - \frac{u(p+w)}{3v} - \frac{u^2}{2\beta},$$

$$\begin{aligned}
\frac{dv}{dt} &= \frac{3w(\lambda_5 - v)}{u} - 4v(p+w), \\
\frac{dw}{dt} &= 4uv(p+w) - \frac{w}{3v\beta}(p+w), \\
\frac{dp}{dt} &= \frac{p+w}{3v}\left(E - \frac{p}{\beta}\right) - w\lambda_5 - 4uv(p+w).
\end{aligned} \tag{4.57}$$

Q_I, Q_{II} and Q_{III} are simply scale factors in the problem, the equations show that λ_5 is an important actor, i.e. the relative energy of the injected pairs to the electrons at $z = 0$.

4.6 The Steady State Solutions

The solutions are found for each system by employing a suitable numerical method.

System I

The solutions of equations (4.55) in the steady state $\frac{du}{dt} = \frac{dv}{dt} = \frac{dw}{dt} = \frac{dp}{dt} = 0$, v is given by:

$$\left(\frac{\lambda_5 - v}{4uv^2}\right)\left[E - \frac{3(\lambda_5 - v)}{4\beta uv}\right] - \lambda_5 = 0, \tag{4.58}$$

where

$$u^2 = 2\beta - \frac{\beta(\lambda_5 - v)}{2v^2}, \tag{4.59}$$

and then:

$$w = 12\beta uv^2, \tag{4.60}$$

$$p = \frac{3(\lambda_5 - v)}{4uv} - w. \tag{4.61}$$

Equations (4.58) and (4.59) are solved together using a simple bisection method from Numerical Recipes (Press *et al.*, 1985). to find all the positive real values of u and v that satisfy both equations. Then values for w and p are found using equations (4.60) and (4.61). These solutions are found subject to the constraint that w and p must have positive real values. Any solutions that have negative or non-real values for w or p are to be ignored since they represent physical quantities. Solutions that disobey this constraint are outside the bounds imposed by the approximations used to obtain the equations.

System II

The solutions of equations (4.56); v is given by:

$$v^3 + \left(\frac{1}{4} + \frac{3}{32\beta^2\lambda_5}\right)v^2 + \left(\frac{E}{8\beta\lambda_5} - \frac{\lambda_5}{4} - \frac{3}{16\beta^2}\right)v + \frac{3\lambda_5}{32\beta^2} - \frac{E}{8\beta} = 0, \tag{4.62}$$

and also:

$$u = \left(\frac{4v^2 + v - \lambda_5}{2v}\right)\beta, \tag{4.63}$$

$$w = 12\beta u v^2, \tag{4.64}$$

$$p = \frac{3}{4}(\lambda_5 - v) - w. \tag{4.65}$$

Equation (4.62) is solved for v using the POLYROOT method from Numerical Recipes (Press *et al.*, 1985) to find the positive real roots. The equations (4.63), (4.64) and (4.65) are used to find u, w and p, again with the constraint that the values are all real and positive.

System III

The solutions of equations (4.57); v is given by:

$$v^4 + \left(\frac{1}{4} + \frac{3}{32\beta^2\lambda_5}\right)v^3 + \left(\frac{3}{16\beta^2} + \frac{\lambda_5}{4}\right)v^2 + \left(\frac{E}{96\beta^2\lambda_5} + \frac{3\lambda_5}{32\beta^2}\right)v - \frac{E}{96\beta^2} = 0, \tag{4.66}$$

and then:

$$u = 6\beta^2\left(4v^2 + v - \lambda_5\right), \tag{4.67}$$

$$w = 12\beta u v^2, \tag{4.68}$$

$$p = 9\beta v(\lambda_5 - v) - w. \tag{4.69}$$

Equation (4.66) is also solved for v using the POLYROOT method to find the positive real roots. Then equations (4.67), (4.68) and (4.69) are used to find u, w and p. Again u, w and p must all have real positive values.

There is only a small range of the (E, β, λ_5) parameter space for which valid solutions exist for system III and checks for stability of these solutions (section 4.7) show that none of these solutions are stable.

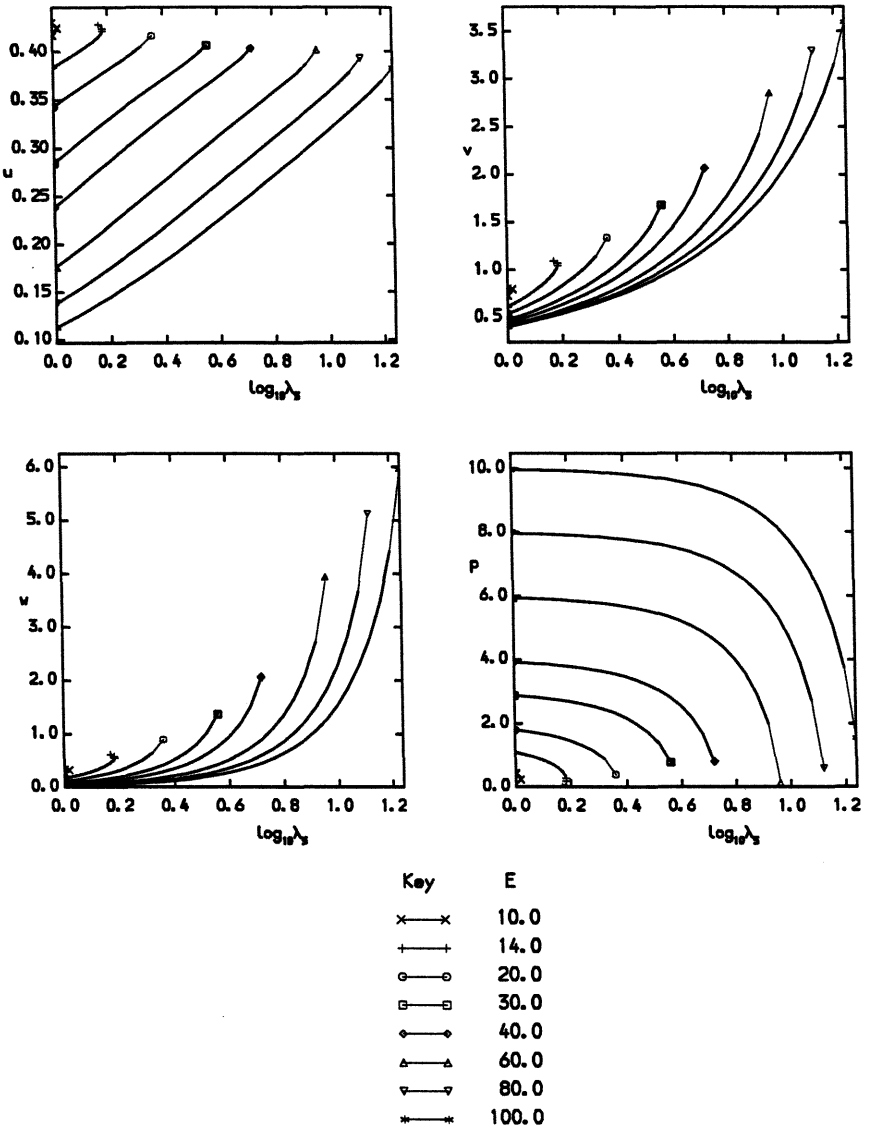

Figure 4.2: System I steady state solutions for various E when $\beta = 0.1$, showing u, v, w and p. The bold lines show stable solutions (section 4.7), the faint lines show unstable solutions

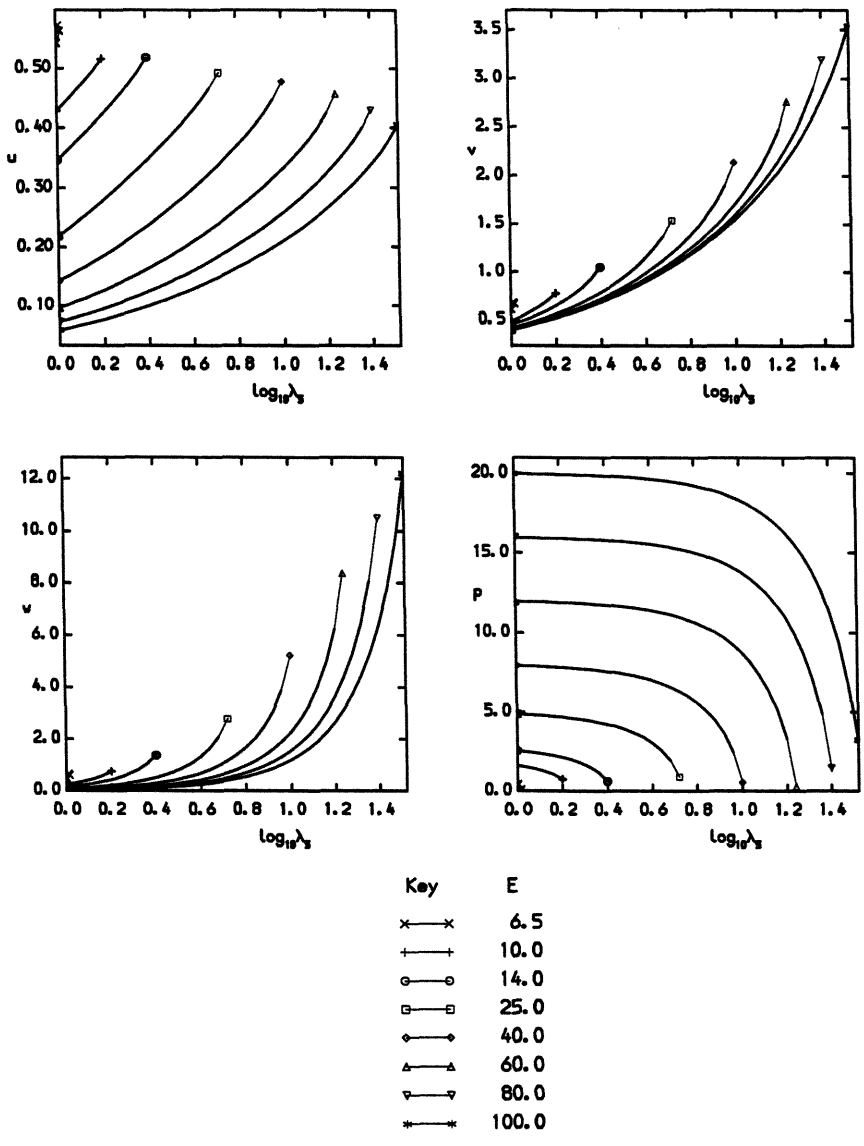

Figure 4.3: System I steady state solutions for various E when $\beta = 0.2$, showing u, v, w and p. The bold lines show stable solutions (section 4.7), the faint lines show unstable solutions

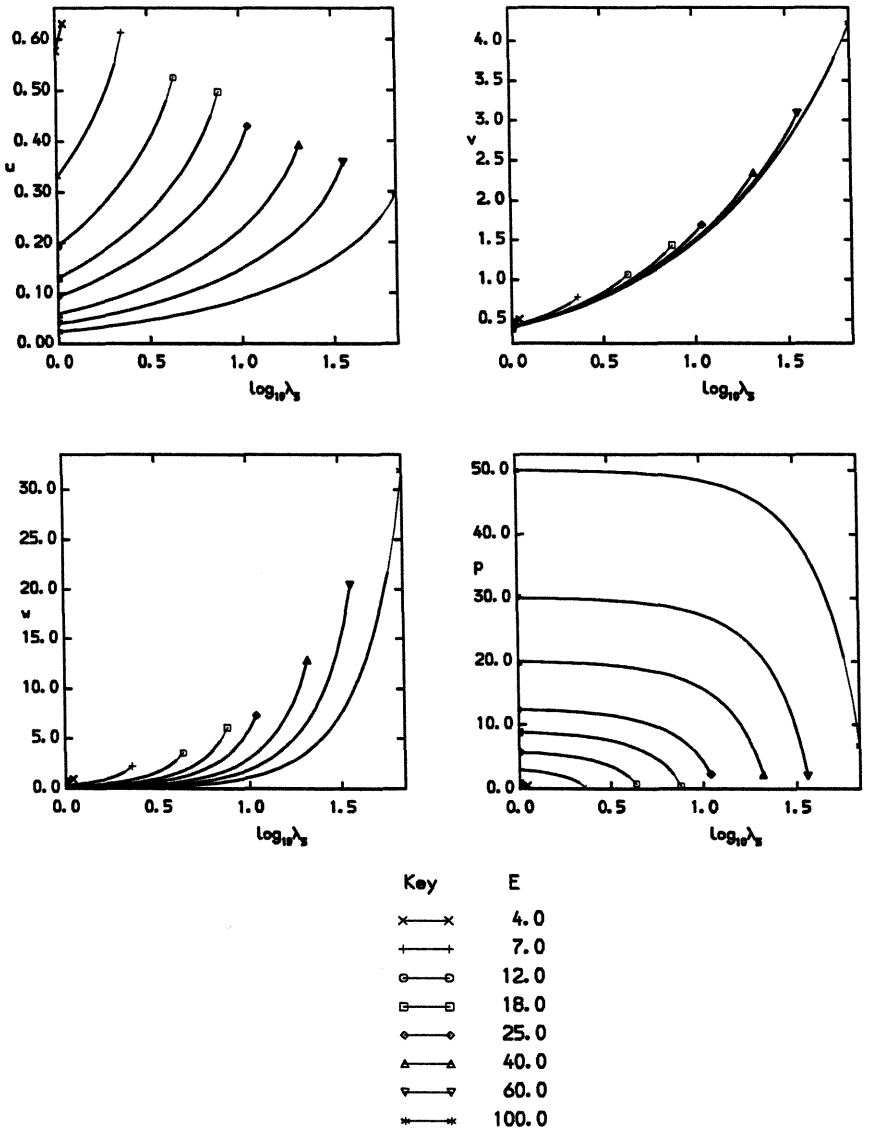

Figure 4.4: System I steady state solutions for various E when $\beta = 0.5$, showing u, v, w and p. The bold lines show stable solutions (section 4.7), the faint lines show unstable solutions

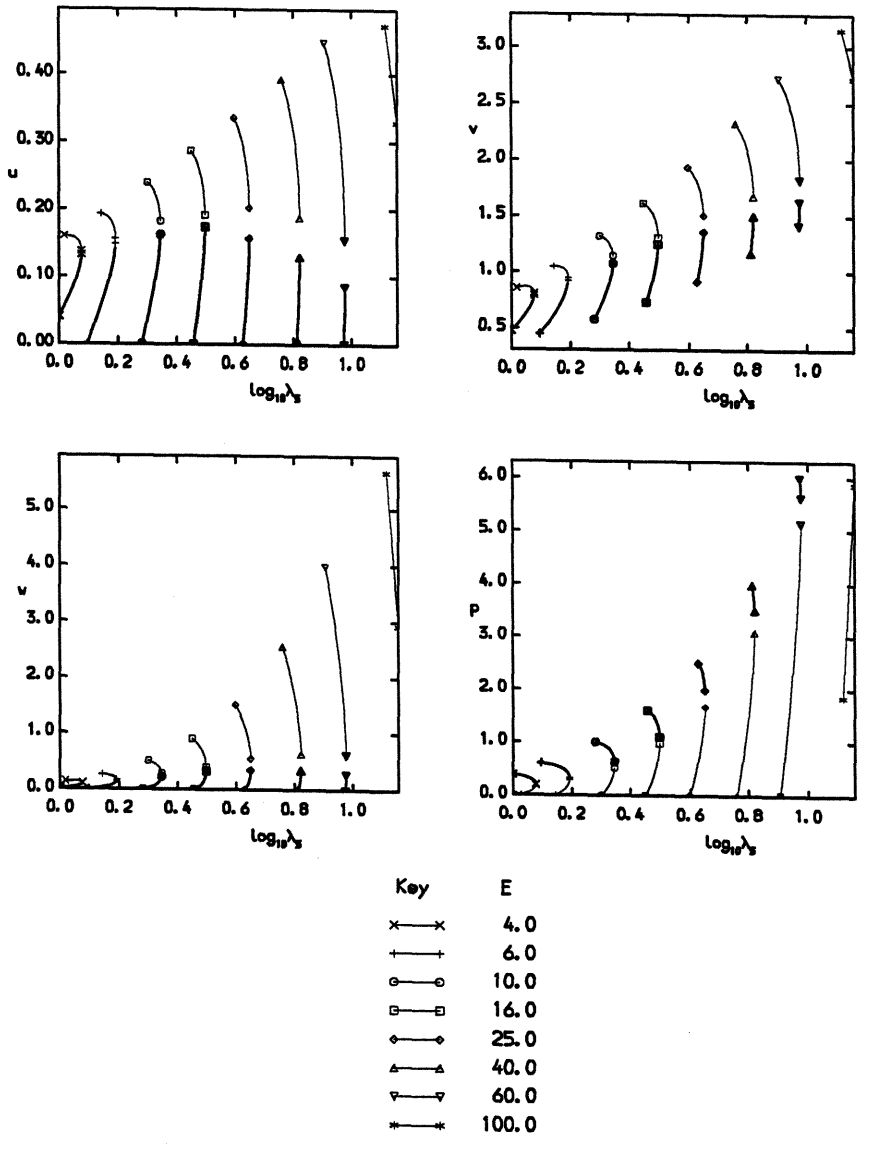

Figure 4.5: System II steady state solutions for various E when $\beta = 0.1$, showing u, v, w and p. The bold lines show stable solutions (section 4.7), the faint lines show unstable solutions

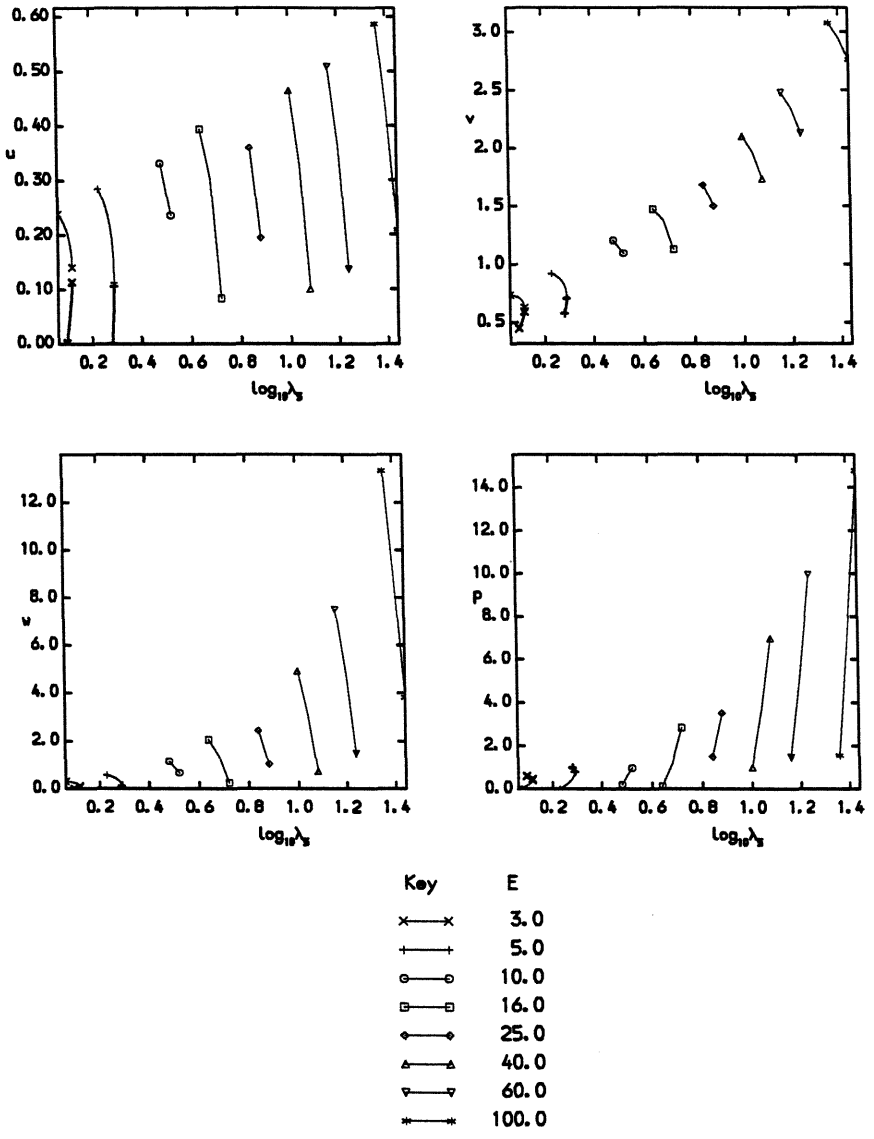

Figure 4.6: System II steady state solutions for various E when $\beta = 0.2$, showing u, v, w and p. The bold lines show stable solutions (section 4.7), the faint lines show unstable solutions

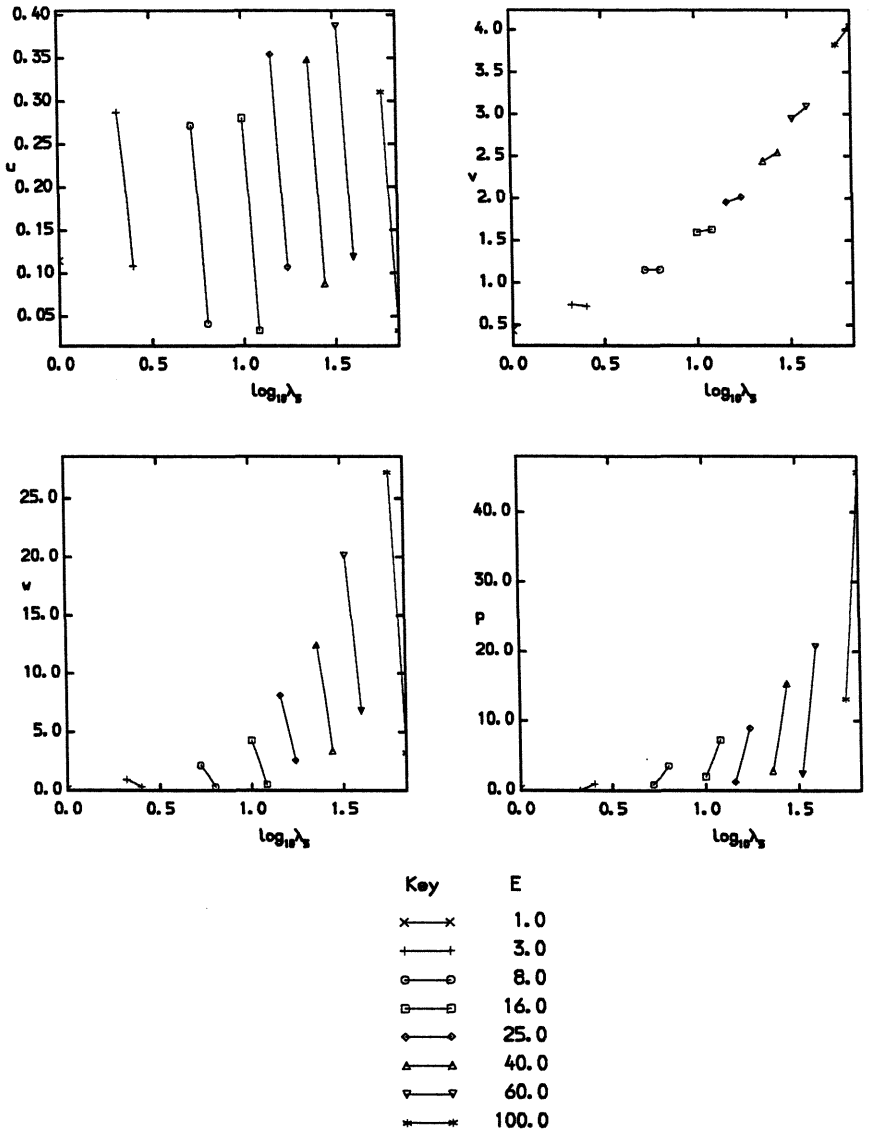

Figure 4.7: System II steady state solutions for various E when $\beta = 0.5$, showing u, v, w and p. The bold lines show stable solutions (section 4.7), the faint lines show unstable solutions

4.6.1 Results

The values chosen for the parameters were $\beta = 0.1$, 0.2 and 0.5 (corresponding to $R/R_g = 100$, 25 and 4) and $1.0 \leq E \leq 100.0$.

The steady state solutions for systems I and II are illustrated in figures 4.2 to 4.7. There is a large range of λ_5 and E where two steady state solutions exist, though as E increases, the range of λ_5 where this is so decreases. For large values of E there is only one solution.

Having two solutions existing for a given set of parameters could lead to an interesting situation: do the solutions co-exist as some kind of multiple state system, or does the system flip between the two in some way? However, the first thing to do is check whether any solutions are stable to small perturbations.

4.7 The Stability of the Steady State Solutions

The stability of the solutions given by equations (4.58) to (4.61), (4.62) to (4.65) and (4.66) to (4.69) can be determined by a linear stability analysis. In general form, equations (4.55), (4.56) and (4.57) can be written as

$$\frac{dx_i}{dt} = F_i(\boldsymbol{x}) \tag{4.70}$$

where i can have values from 1 to 4. Linearizing the equations (4.70) about the critical point (x_1, x_2, x_3, x_4) yields:

$$\frac{d}{dt}\begin{pmatrix} \delta x_1 \\ \delta x_2 \\ \delta x_3 \\ \delta x_4 \end{pmatrix} = \begin{pmatrix} \frac{\partial F_1}{\partial x_1} & \frac{\partial F_1}{\partial x_2} & \frac{\partial F_1}{\partial x_3} & \frac{\partial F_1}{\partial x_4} \\ \frac{\partial F_2}{\partial x_1} & \frac{\partial F_2}{\partial x_2} & \frac{\partial F_2}{\partial x_3} & \frac{\partial F_2}{\partial x_4} \\ \frac{\partial F_3}{\partial x_1} & \frac{\partial F_3}{\partial x_2} & \frac{\partial F_3}{\partial x_3} & \frac{\partial F_3}{\partial x_4} \\ \frac{\partial F_4}{\partial x_1} & \frac{\partial F_4}{\partial x_2} & \frac{\partial F_4}{\partial x_3} & \frac{\partial F_4}{\partial x_4} \end{pmatrix} \begin{pmatrix} \delta x_1 \\ \delta x_2 \\ \delta x_3 \\ \delta x_4 \end{pmatrix} \tag{4.71}$$

where all the $\frac{\partial F_i}{\partial x_j}$ are evaluated at the critical point. I shall write (4.71) as

$$\frac{d}{dt}\delta\boldsymbol{x} = \nabla\boldsymbol{F}\,\delta\boldsymbol{x}. \tag{4.72}$$

Now, solve for $\delta\boldsymbol{x}$ by substituting

$$\delta\boldsymbol{x} = \boldsymbol{C}e^{\kappa t}, \tag{4.73}$$

and then

$$(\nabla\boldsymbol{F} - \kappa\boldsymbol{I})\,\delta\boldsymbol{x} = 0, \tag{4.74}$$

i.e. κ is an eigenvalue of $\nabla \boldsymbol{F}$, which can be found numerically; there will be four such eigenvalues since this is a four dimensional system. The critical point is stable if and only if all four eigenvalues are negative, if any one is positive then the critical point will be locally unstable to any small fluctuations.

To evaluate the eigenvalues κ first all the $\frac{\partial F_i}{\partial x_j}$ are calculated at the critical point under investigation. These values are entered into the matrix $\nabla \boldsymbol{F}$ and the eigenvalues of the matrix found using routine F02AGF from the NAG software library.

For System III, none of the values (E, β, λ_5) chosen produced stable solutions. For Systems I and II, for a given choice of E and β there were always values of λ_5 that produced a single stable solution. There was never more than one stable solution. In figures 4.2 to 4.7, the stable solutions are shown as bold lines, while the unstable solutions are shown as faint lines.

The graphs for System I show that λ_5 can have a maximum value of ~ 50, with a minimum of 1. The graphs for System II show that for a given choice for (E, β) there is only a small range of λ_5 that produce a stable solution, and the values of λ_5 range betweed 1 and 10 depending on β and E. Note that there are no stable solutions for System II when $\beta = 0.5$.

The implication is that the energy of the injected pairs must not be that much higher than the initial energy of the electrons at the base of the column. There may be a stable situation at larger values of λ_5, but the approximations made to produce equations (4.54) are such that these values do not produce physically sensible results. However, note that for System I, as λ_5 increases, the solutions are at first stable, then unstable and then physically unsuitable. This suggests that there *may* be no stable solutions at larger λ_5, though of course there is no proof for this statement.

4.8 Observable Implications: The Optical Depth to Compton Scattering

As stated earlier, I have assumed that the hard X-ray/γ-ray band of the spectrum can be represented by a power law, calculated from the quantities $n_\pm$ and $T_\pm$. Observations of AGN spectra show that the spectrum in this energy band is generally a power law with energy index $\simeq 0.9$ (Shastri *et al.*, 1993).

The optical depth to Compton scattering due to the pairs is

$$\tau = \int_0^{z_{esc}} n_{\pm}(z)\,\sigma_T dz \simeq \bar{n}_{\pm}\sigma_T z_{esc}. \tag{4.75}$$

Using the substitutions as before, equations (4.27 and 4.28)

$$\tau = y_2\zeta. \tag{4.76}$$

Now, using equation (4.48) to substitute for ζ yields

$$\tau = \frac{3y_2y_4}{\lambda + y_6}. \tag{4.77}$$

The substitutions used to produce the equations (4.55), (4.56) and (4.57), for either of the Systems I, II and III, give

$$\tau = \frac{3uv}{p+w}, \tag{4.78}$$

i.e. the optical depth to Compton scattering is independant of the number of pairs being injected, under these approximations.

The optical depth in terms of physical quantities is found by substituting for y_2, y_4, y_6 and y_7 in equation (4.77) using the changes of variable equations (4.27):

$$\tau = \frac{3n_{\pm}kT_{\pm}}{U_{UV} + U_{\gamma}}. \tag{4.79}$$

This is the same as

$$\tau = \frac{\text{energy density in pairs}}{\text{energy density in radiation}},$$

i.e.τ^{-1} is an 'ionisation parameter'.

The optical depths for various λ_5 and E are shown in figures 4.8 to 4.13, in all cases $\tau < 1$.

I assume that the spectrum in the hard X-ray/γ-ray band is a power law, and I use the results obtained by Katz (1975) to estimate the index. Katz defined a critical radius,

$$R_c = \frac{\pi}{2}\left(\frac{m_e c^2}{3kT}\right)^{\frac{1}{2}}, \tag{4.80}$$

where the distance R is measured in units of the photon mean free path to spontaneous Thomson scattering. A numerical method was then used to deduce the emergent spectrum from a cloud of radius R and a table of R/R_c against α, the power law index was produced, see table 4.1. Katz assumed the photons were scattered by hot but nonrelativistic electrons, so using those results here gives only an approximate idea of the power law index.

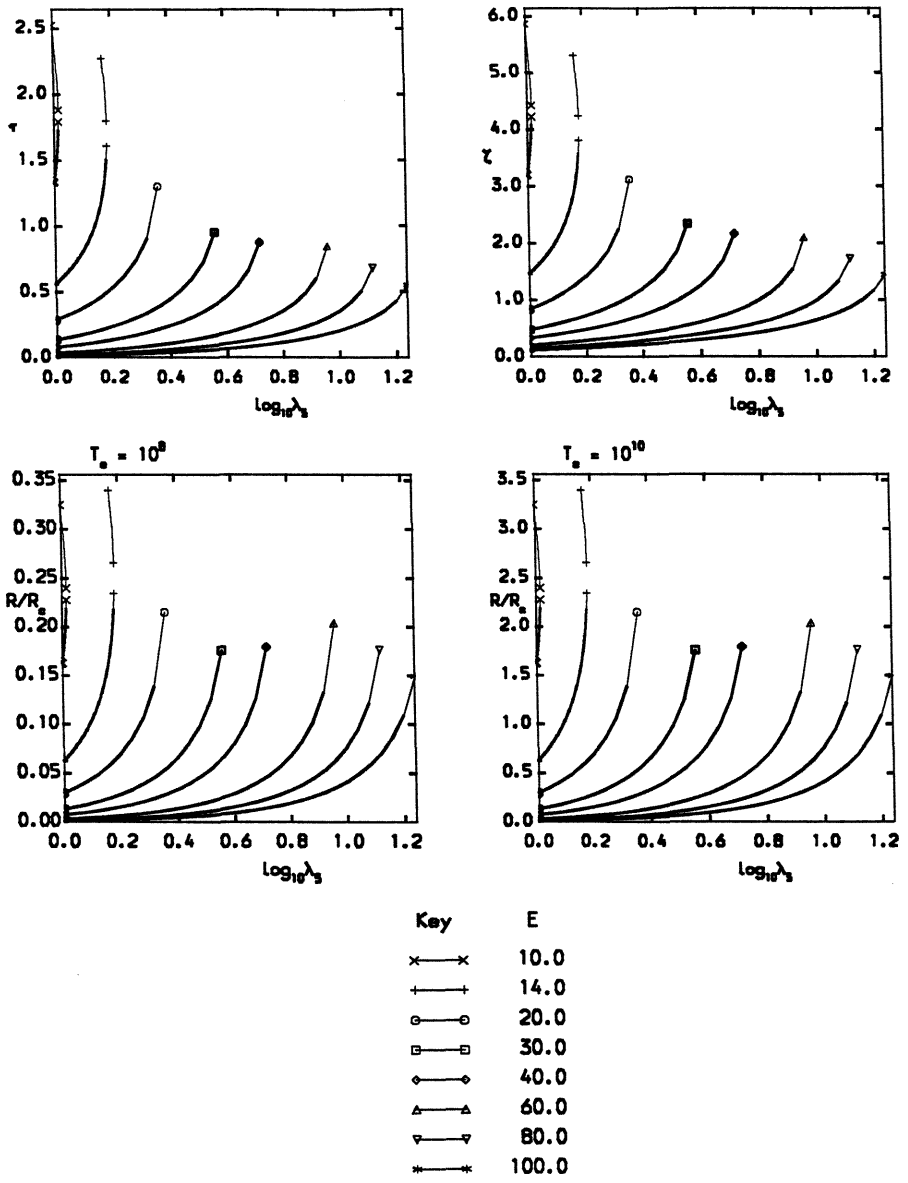

Figure 4.8: System I steady state solutions for various E when $\beta = 0.1$, showing optical depth τ, column dimensionless height ζ and the Katz (R/R_c) ratio for $T_{e_0} = 10^8$ and 10^{10}. The bold lines show stable solutions (section 4.7), the faint lines show unstable solutions

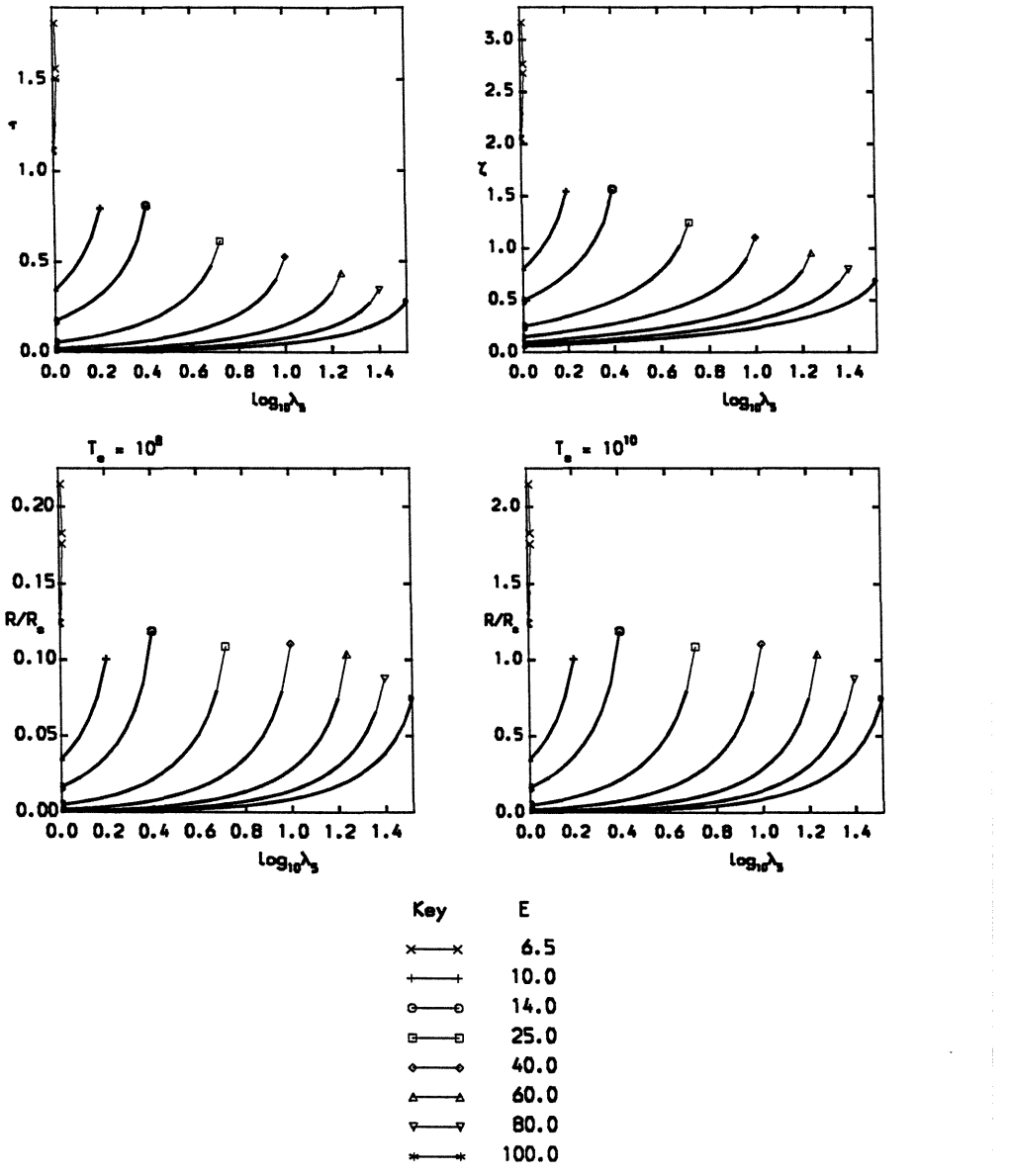

Figure 4.9: System I steady state solutions for various E when $\beta = 0.2$, showing optical depth τ, column dimensionless height ζ and the Katz (R/R_c) ratio for $T_{e_0} = 10^8$ and 10^{10}. The bold lines show stable solutions (section 4.7), the faint lines show unstable solutions

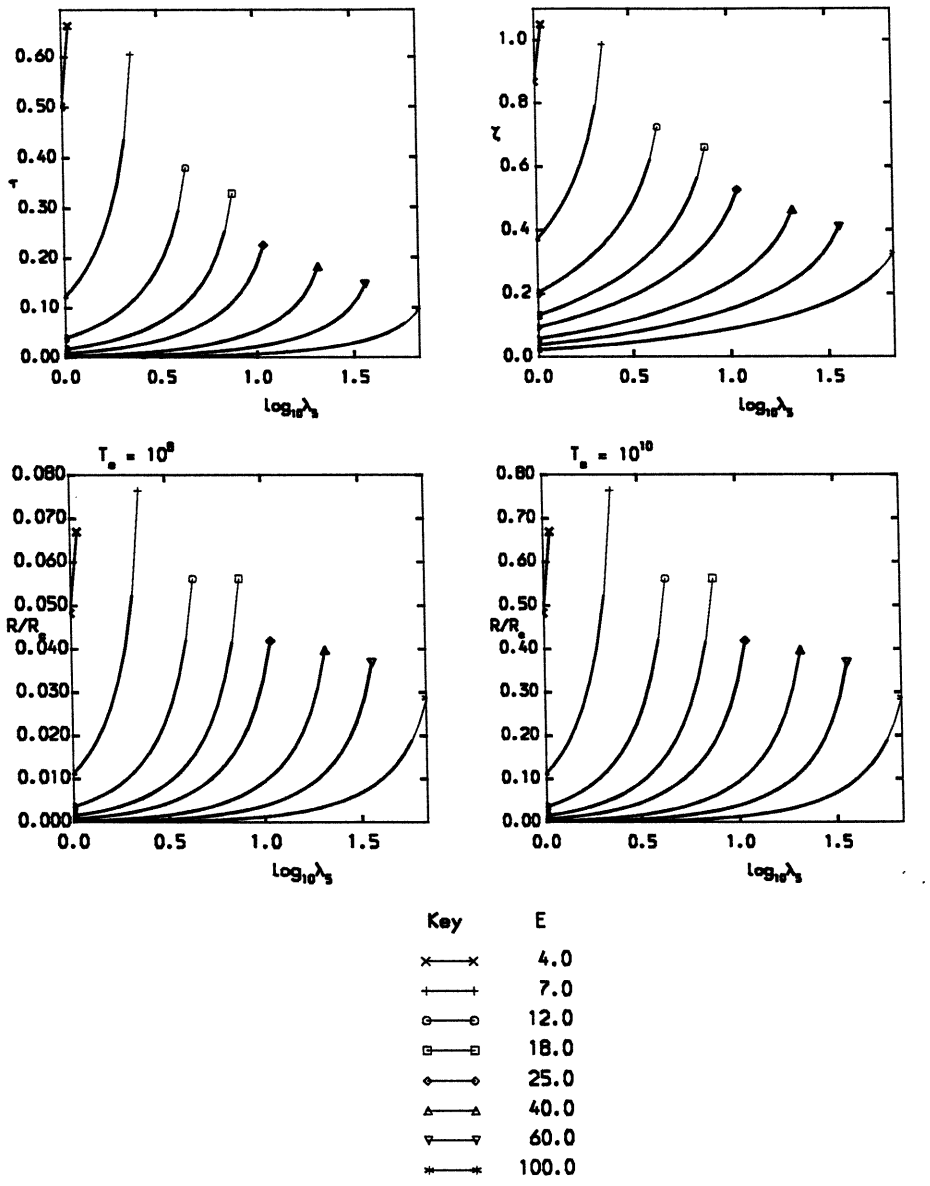

Figure 4.10: System I steady state solutions for various E when $\beta = 0.5$, showing optical depth τ, column dimensionless height ζ and the Katz (R/R_c) ratio for $T_{e_0} = 10^8$ and 10^{10}. The bold lines show stable solutions (section 4.7), the faint lines show unstable solutions

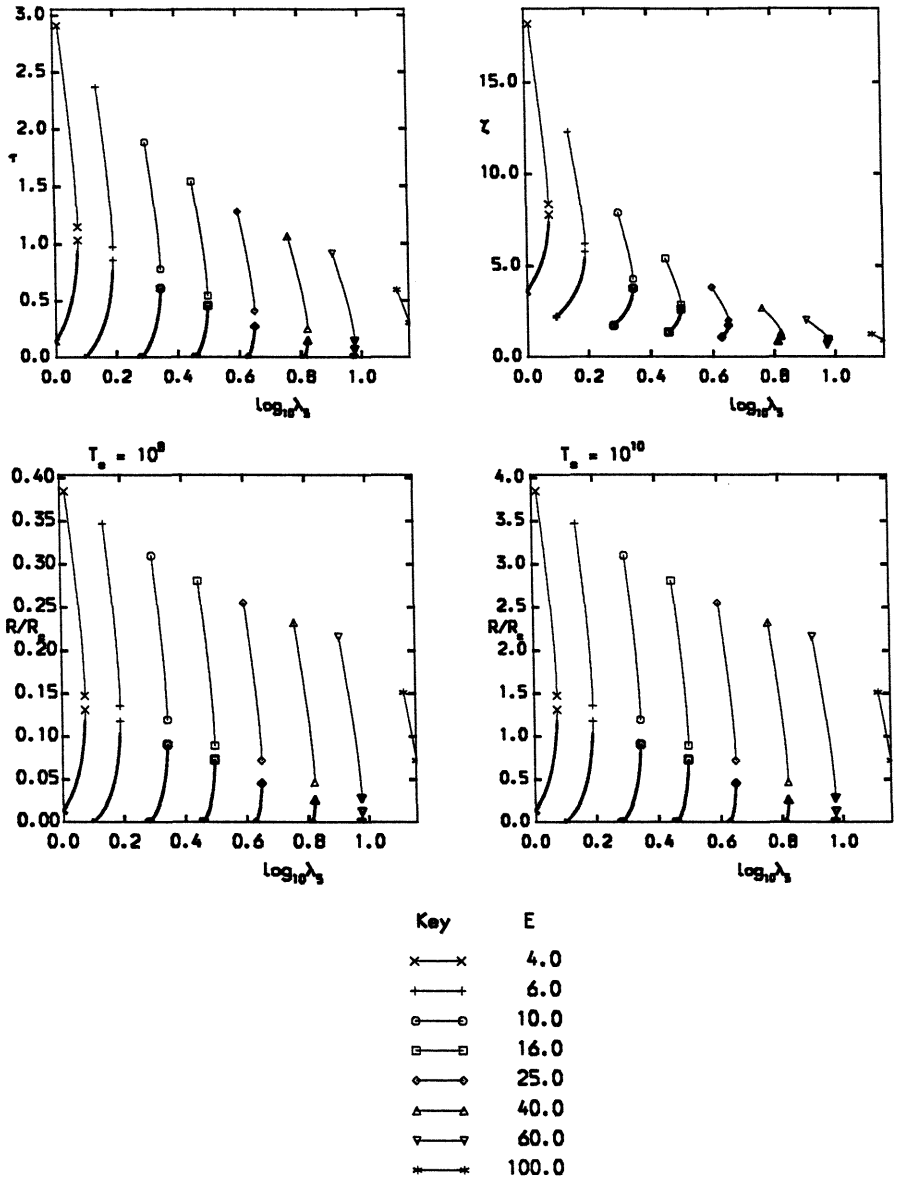

Figure 4.11: System II steady state solutions for various E when $\beta = 0.1$, showing optical depth τ, column dimensionless height ζ and the Katz (R/R_c) ratio for $T_{e_0} = 10^8$ and 10^{10}. The bold lines show stable solutions (section 4.7), the faint lines show unstable solutions

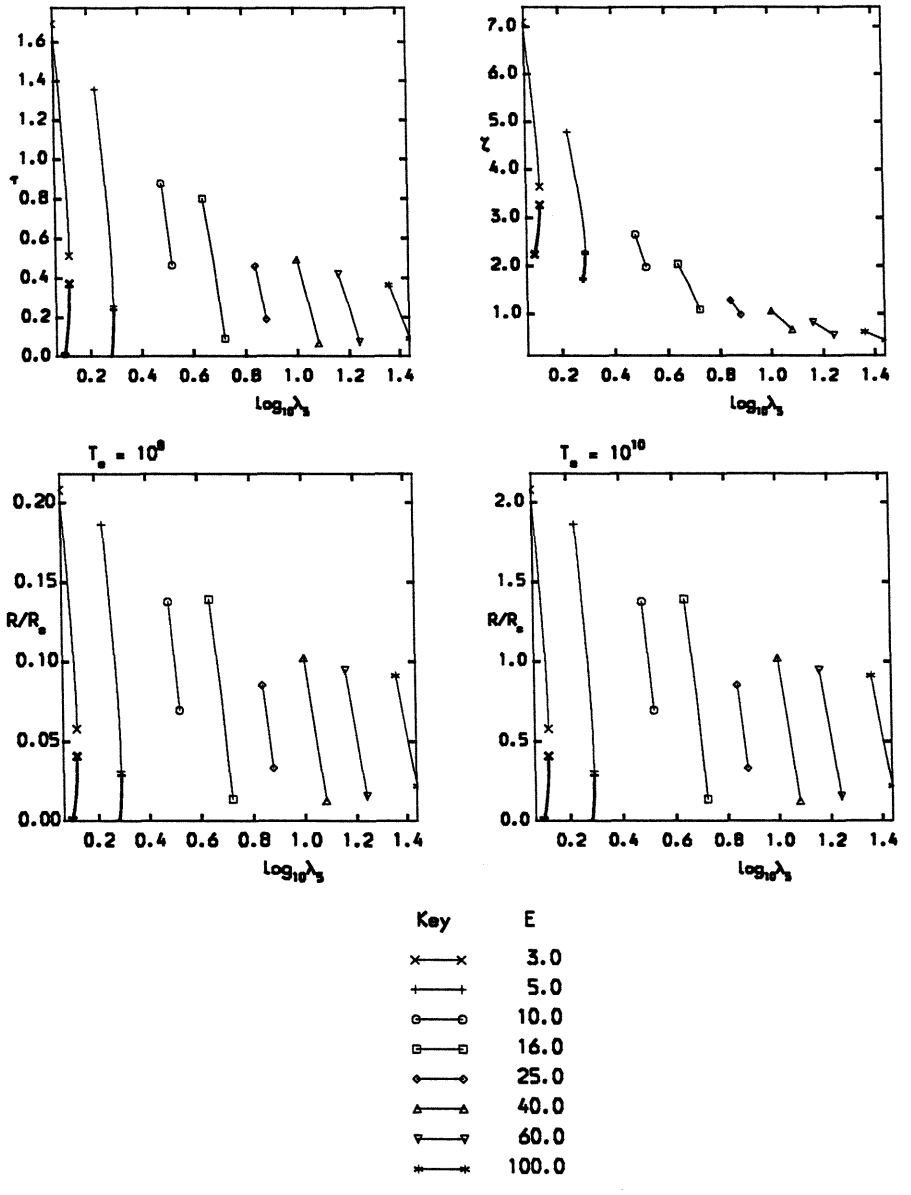

Figure 4.12: System II steady state solutions for various E when $\beta = 0.2$, showing optical depth τ, column dimensionless height ζ and the Katz (R/R_c) ratio for $T_{e_0} = 10^8$ and 10^{10}. The bold lines show stable solutions (section 4.7), the faint lines show unstable solutions

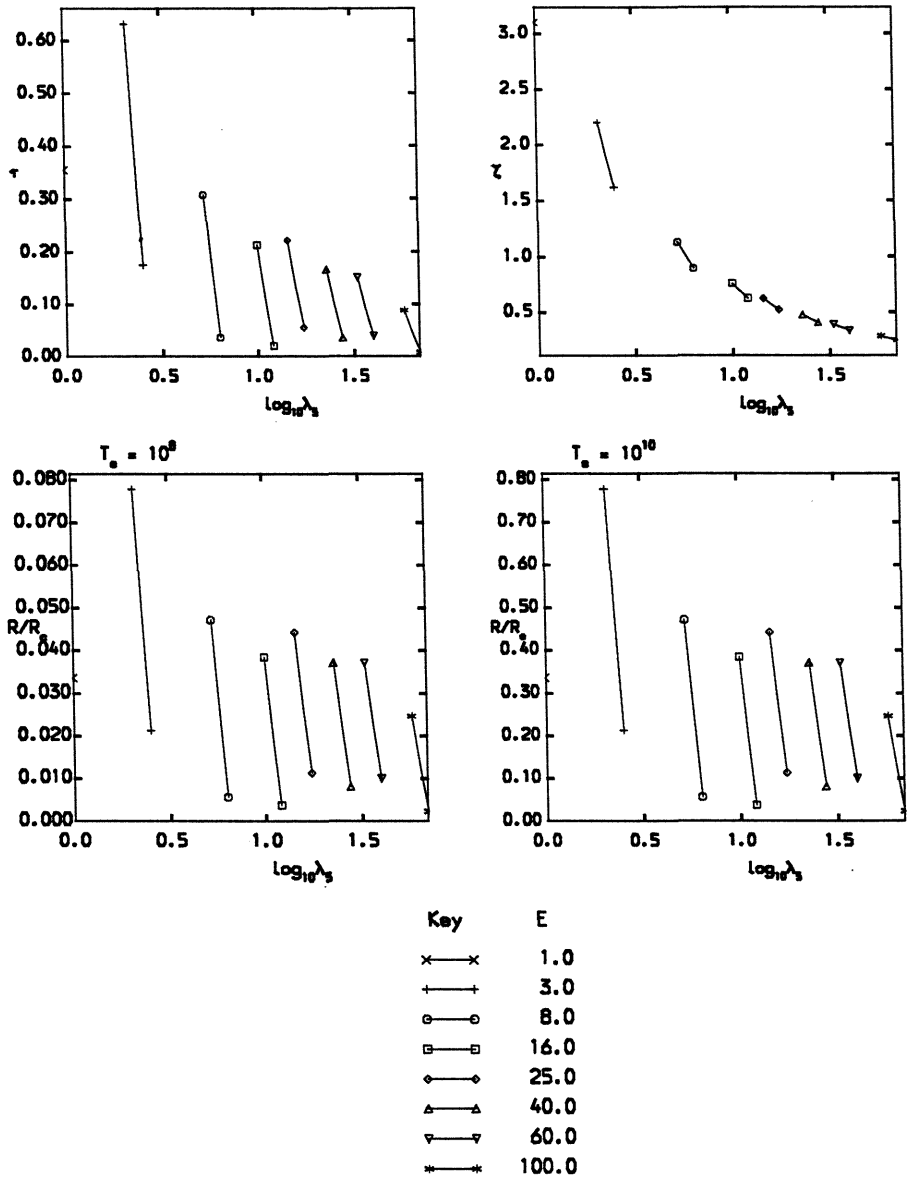

Figure 4.13: System II steady state solutions for various E when $\beta = 0.5$, showing optical depth τ, column dimensionless height ζ and the Katz (R/R_c) ratio for $T_{e_0} = 10^8$ and 10^{10}. The bold lines show stable solutions (section 4.7), the faint lines show unstable solutions

Table 4.1: Variation of power law index α with the Comptonisation factor R/R_c, reproduced from Katz (1975).

R/R_c	0.3	0.4	0.5	0.6	0.7	0.8	0.9	1.0	1.3	1.6	2.0
α	4.1	2.9	2.2	1.7	1.3	1.1	0.9	0.8	0.5	~ 0.3	~ 0.1

In terms of my units, the column height in units of the photon mean free path is

$$R = \bar{n}_{\pm}\sigma_T z_{esc} = \tau \tag{4.81}$$

and

$$R_c = \frac{\pi}{2}\left(\frac{m_e c^2}{3k\overline{T}_{\pm}}\right)^{\frac{1}{2}} = \frac{\pi}{2}\left(\frac{m_e c^2}{3kT_{e_0} y_4}\right)^{\frac{1}{2}} \tag{4.82}$$

So, to estimate the index of the power law, I evaluate

$$\left(\frac{R}{R_c}\right) = \frac{2\tau}{\pi}\left(\frac{3kT_{e_0} y_4}{m_e c^2}\right)^{\frac{1}{2}} \tag{4.83}$$

Figures 4.8 to 4.13 show, in addition to τ and ζ, R/R_c for $T_{e_0} = 10^8$ K and 10^{10} K. If $T_{e_0} = 10^8$ then $R/R_c < 0.2$ and from table 4.1 it is clear that the spectral index $\alpha > 4.1$ and very little spectral evolution has occurred. However, if $T_{e_0} = 10^{10}$ K then $R/R_c \sim 1$ which corresponds to $\alpha \sim 1$, i.e close to the observed value. More detailed consideration of the model will be required to establish whether this can lead to detailed agreement with observation.

4.9 $e^{\pm}$-Pair Creation by γ-γ Interactions

Pairs are only created by γ-γ interactions if the compactness parameter (Guilbert, Fabian and Rees, 1983) l is large. In a spherical cloud, the compactness parameter is defined as

$$l = \frac{\sigma_T L}{m_e c^3 R} \tag{4.84}$$

where R is the radius of the cloud. Here, the depth of the region is z_{esc} and the luminosity $L \sim \overline{U}_{\gamma} c R$, where R is taken as the width of the column. I make the following changes of variable from equations (4.27), (4.28) and (4.32):

$$\begin{aligned} y_6(x) &= \frac{\overline{U}_{\gamma}(t)}{kT_{e_0} n_{e_0}}, \\ \zeta &= \sigma_T n_{e_0} z_{esc}, \\ \beta &= \sqrt{\frac{R_g}{R}}, \end{aligned} \tag{4.85}$$

Table 4.2: Range of $\dot{n}_+/l$ for system I

β	$\dot{n}_+/l$ (cm^{-3} s^{-1})
0.1	10^{17} to 7×10^{17}
0.2	2×10^{18} to 3×10^{18}
0.5	4×10^{17} to 2×10^{19}

to give

$$l = \frac{{\sigma_T}^2 k R_g n_{e_0}^2 T_{e_0}}{m_e c^2} \frac{y_6}{\zeta \beta^2}. \tag{4.86}$$

Writing

$$\mathcal{L} = \frac{{\sigma_T}^2 k R_g n_{e_0}^2 T_{e_0}}{m_e c^2} = 2.2 \times 10^{-45} n_{e_0}^2 T_{e_0} \tag{4.87}$$

and using equation (4.48) to represent ζ in terms of other variables, the compactness parameter may be evaluated as

$$l = \mathcal{L} Q_I \frac{w(p+w)}{3v\beta^2} \tag{4.88}$$

for system I, or

$$l = \mathcal{L} Q_{II}^2 \frac{w(p+w)}{3v\beta^2} \tag{4.89}$$

for system II.

In order to estimate the compactness I write equation (4.88) in terms of physical values using

$$Q_I = \frac{2\dot{n}_+}{\sigma_T n_{e_0}^2 v_{esc}} \tag{4.90}$$

from equation (4.28) to obtain

$$l = 2.2 \times 10^{-31} T_{e_0} \dot{n}_+ \frac{w(p+w)}{3v\beta^3}. \tag{4.91}$$

Assuming $T_{e_0} = 10^{10}$ and taking values for v, w and p from figures 4.2, 4.3 and 4.4 I find $\dot{n}_+/l > 10^{17}$ cm^{-3} s^{-1}, table 4.2 shows more detailed results.

Similarly, for system II, I rewrite equation (4.89) to get

$$l = 2.2 \times 10^{-17} \frac{T_{e_0} \dot{n}_+^2}{n_{e_0}^2} \frac{w(p+w)}{3v\beta^3}, \tag{4.92}$$

and assuming $T_{e_0} = 10^{10}$ and taking values for v, w and p from figures 4.5, 4.6 and 4.7 I find $\dot{n}_+/\sqrt{l} > 10 n_{e_0}$ s^{-1}, table 4.3 shows more detailed results.

I conclude that the rate of production of pairs by γ-γ interactions is negligible for both systems I and II, when compared to the rate of injection of pairs.

Table 4.3: Range of $\dot{n}_+/\sqrt{l}$ for system II

β	$\dot{n}_+/\sqrt{l}$ (s^{-1})		
0.1	$18n_{e_0}$	to	$48n_{e_0}$
0.2	$175n_{e_0}$	to	$675n_{e_0}$

Table 4.4: Estimated values of compactness, l

System	T_{e_0}	β	n_{e_0}	Q	w	ζ	l
I	10^8	0.1	10^{13}	100	2	1	4×10^{-8}
	10^8	0.2	10^{13}	10	10	0.5	4×10^{-8}
	10^8	0.5	10^{13}	10	15	0.3	1×10^{-8}
II	10^8	0.2	10^{13}	4	10^{-2}	2	1×10^{-11}

To estimate the value of the compactness parameter, I go back to equation (4.86) and use the transformations $y_6 = w\sqrt{Q_I}$ and $y_6 = Q_{II}$ for systems I and II respectively:

$$l = 2.2 \times 10^{-45} n_{e_0}^2 T_{e_0} \frac{w\sqrt{Q_I}}{\zeta\beta^2}, \tag{4.93}$$

$$l = 2.2 \times 10^{-45} n_{e_0}^2 T_{e_0} \frac{wQ_{II}}{\zeta\beta^2}. \tag{4.94}$$

Examination of figures 4.8 to 4.13 indicates that $0.1 < \zeta < 10$. In equation (4.28) I estimated $\zeta \simeq 6 \times 10^{-3} \left(\frac{n_{e_0}}{10^{10}\ \mathrm{cm}^{-3}}\right) \left(\frac{z_{esc}}{10^{12}\ \mathrm{cm}}\right)$. This implies that $10^{11}\ \mathrm{cm}^{-3} < n_{e_0} < 10^{13}\ \mathrm{cm}^{-3}$ if I assume that $z_{esc} = 10^{12}$ cm; taking values for w and ζ from figures 4.2 to 4.13 and evaluating the compactness from equation (4.93) or (4.94) as appropriate indicates that the compactness $l \ll 1$ and so the production of pairs by γ-γ interactions is negligible. Estimates of compactness are summarised in table 4.4.

4.10 Discussion

The results of the stability analysis in section 4.7 imply that the injection energy of the pairs is not much higher than the energy of the electrons at the base of the column. Because $\lambda_5 \sim 10$ or less, the pair injection temperature $T_{\pm_i} \sim 10T_{e_0}$, i.e. if $T_{e_0} = 10^8$ K then the characteristic temperature of the injected pairs $T_{\pm_i} \sim 10^9$ K. The stable solutions at these values of λ_5 and E have $\overline{T}_\pm \sim T_{e_0}$ ($y_4 = v \sim 1$) so the pairs cool to the initial electron temperature and the energy lost by the pairs fuels the acceleration of the wind. I have, however, constrained the solution such that the wind velocity must reach the escape velocity, the results clearly show

that under this constraint a solution is possible but there is no obvious physical process driving the wind (since the material is optically thin). If, however, $T_{e_0} \sim 10^{10}$ K, the pair injection temperature $T_{\pm_i} \sim 10^{11}$ K or more and the average column temperature $\overline{T}_{\pm} \sim 10^{11}$ K; now the optical depth $\tau > 1$ and the UV spectrum is comptonised to a power law with index ~ 1.

The major flaw in this model is the way in which I arrive at the approximation for ζ (equations (4.45) to (4.48)), for example there may be solutions where the denominator of equation (4.45) is close to zero. To check this approximation I first rewrite equation (4.45) in terms of u, v, w, p and $q = Q_I$ for system I, using ζ_* to avoid confusion with ζ calculated earlier:

$$\zeta_* = \frac{2\lambda_1 \left(1 - uv\sqrt{Q_I}\right) + \mu u\sqrt{Q_I} - \lambda_3}{Q_I \left(\mu - \frac{2}{3}\lambda_1 u\,(p+w)\right)}, \tag{4.95}$$

and $q = Q_{II} y_2 y_4$ for system II:

$$\zeta_* = \frac{2\lambda_1 \left(1 - uvQ_{II}\right) + \mu u Q_{II} - \lambda_3}{Q_{II}^2 \left(\mu uv - \frac{2}{3}\lambda_1 u\,(p+w)\right)}. \tag{4.96}$$

From equation (4.28) I assume $\lambda_1 = 10^{-9} T_{e_0} \beta^2$ and $\lambda_3 = 0.3\,\beta$. For various values of Q_I and Q_{II} I can evaluate ζ_* using u, v, w and p previously calculated. I find that when $T_{e_0} = 10^{10}$ K there are no cases where $\zeta_* \sim \zeta$. For system I when $T_{e_0} = 10^8$ K, there are a small number of cases where $\zeta_* \sim \zeta$: when λ_5 has the largest values possible such that the solutions are stable and when $\beta = 0.1$, $Q_I \sim 100$ and $E > 25$; $\beta = 0.2$, $Q_I \sim 100$ and $E > 35$; or $\beta = 0.5$, $Q_I \sim 10$ and $E > 20$; for a given set of (β, Q_I, E) the functional form of $\zeta_*(\lambda_5)$ is different from the form of $\zeta(\lambda_5)$. For system II when $T_{e_0} = 10^8$ K, the only cases where $\zeta_* \sim \zeta$ is when $\beta = 0.2$ and $Q_{II} \sim 4$, for any E, and the functional forms of $\zeta_*(\lambda_5)$ and $\zeta(\lambda_5)$ are the same.

It is clear that the only conditions when equation (4.48) is a good approximation for equation (4.45) is when $T_{e_0} = 10^8$ K using system II when $\beta = 0.2$ and $Q_{II} \sim 4$, plus a few system I cases. Essentially, this approximation restricts the range of physical parameters that may be investigated. Should this work be continued, the next step must be to calculate the solutions using equation (4.45) to evaluate ζ.

Bibliography

Bassani, L., Dean, A.J., Di Cocco, G., Perotti, F., 1985, *Active Galactic Nucleii*, ed. J.E. Dyson, Manchester University Press.

Becker, P.A., and Begelman, M.C., 1986a, *Astrophys. J.*, **310**, 534.

Becker, P.A., and Begelman, M.C., 1986b, *Astrophys. J.*, **310**, 552.

Begelman, M.C., 1978, *Astron. Astrophys.*, **70**, 583.

Blandford, R.D., and Payne, D.G., 1981, *Mon. Not. R. Astr. Soc.*, **194**, 1033.

Bonometto, S., and Rees, M.J., 1971, *Mon. Not. R. Astr. Soc.*, **152**, 21.

Cassidy, I., and Raine, D.J., 1993, *Mon. Not. R. Astr. Soc.*, **260**, 385.

Cox, J.P., and Giuli, R.T., 1968, *Principles of Stellar Structure, Vol. 2* (Gordon and Breach, New York), chp. 24.

Done, C., and Fabian, A.C., 1989, *Mon. Not. R. Astr. Soc.*, **240**, 81.

Drew, J.E., and Boksenberg, A., 1984, *Mon. Not. R. Astr. Soc.*, **211**, 813.

Dyson, J.E. and Perry, J.J., 1987, *Emission Lines in Active Nucleii*, ed. by Gondhalekar, P.M., RAL-87-109, Rutherford Appleton laboratory, p.132.

Fabian, A.C., Guilbert, P.W., Arnaud, K.A., Shafer, R.A., Tennant, A.F., Ward, M.J., 1986, *Mon. Not. R. Astr. Soc.*, **218**, 457.

Ferland, G.J. and Rees, M.J., 1990, *Astrophys. J.*, **332**, 141.

Flammang, R.A., *Mon. Not. R. Astr. Soc.*, **199**, 833.

Frank, King and Raine, 1992, *Accretion Power in Astrophysics*, Cambridge University Press.

Fukue, J., 1986, *Publ. Astron. Soc. Japan*, **38**, 167.

Garbow, B.S., Hillstrom, K.E., and More, J.J., March 1980, *Minpack Project*, Argonne National Laboratory.

Guilbert, P.W., 1981, *Mon. Not. R. Astr. Soc.*, **197**, 451.

Guilbert, P.W., Fabian, A.C. and Rees, M.J., 1983, *Mon. Not. R. Astr. Soc.*, **205**, 593.

Haardt F., and Maraschi, L., 1993, *Astrophys. J.*, **413**, 507.

Katz, J.I., 1976, *Astrophys. J.*, **206**, 910.

Kompaneets, A.S., 1957, *Soviet Phys. - JETP*, 4, 730.

Krolik, J.H., Kallman, T.R., Fabian, A.C., Rees, M.J., 1985, *Astrophys. J.*, **295**, 104.

Krolik, J.H., McKee, C.F., Tarter, C.B., 1981 *Astrophys. J.* **249**, 422.

Lightman, A.P., 1982, *Astrophys. J.*, **253**, 842.

Mathews, W.G. and Doane, J.S. 1990, *Astrophys. J.*, **352**, 423.

Mathews, W.G. and Ferland, G.F., 1987, *Astrophys. J.* **323**, 456.

Meier, D.L., 1982a, *Astrophys. J.*, **256**, 681.

Meier, D.L., 1982b, *Astrophys. J.*, **256**, 693.

Meier, D.L., 1982c, *Astrophys. J.*, **256**, 706.

Michel, F.C., 1972, *Astrophys. Space Sci.*, **15**, 153.

Numerical Algorithms Group Ltd., NAG Fortran Library, Mark 14.

Perry, J.J., and Dyson, J.E., 1985, *Mon. Not. R. Astr. Soc.*, **213**, 665.

Press, W.H., Flannery, B.P., Teukolsky, S.A., Vetterling, W.T., 1985, *Numerical Recipes: The Art of Scientific Computing*, Cambridge University Press, 1985.

Pringle, J.E., 1981, *Ann. Rev. Astron. Astrophys.*, **19**, 137 .

Raine, D.J., and O'Reilly, M.D., 1993, *Astro. Lett. and Communications*, **28**, 331.

Rees, M.J., Begelman, M.C., Blandford, R.D., Phinney, E.S., 1982, *Nature*, **295**, 17.

Ross, R.R., 1979, *Astrophys. J.*, **233**, 334.

Rothschild, R.E., Mushotzky, R.F.,Baity, W.A., Gruler, D.E., Matteson, J.L. and Peterson, L.E., 1983, *Astrophys. J.* **269**, 423.

Rybicki, G.B., and Lightman, A.P., 1979, *Radiative Processes in Astrophysics* (New York: Wiley).

Shapiro, S.I., Lightman, A.P., and Eardley, D., 1976, *Astrophys. J.*, **204**, 187.

Shastri, P., Wilkes, B.J., Elvis, M., McDowell, J., 1993, *Astrophys. J.*, **410**, 29.

Smith, M.D., and Raine, D.J., 1988, *Mon. Not. R. Astr. Soc.*, **234**, 297.

Stepney, S., and Guilbert, P.W., 1983, *Mon. Not. R. Astr. Soc.*, **204**, 1269.

Sunyaev, R.A., and Titarchuk, L.A., 1980, *Astron. Astrophys.*, **86**, 121.

Turner, T.J., and Pounds, K.A., 1989, *Mon. Not. R. Astr. Soc.*, **240**, 833.

Yaqoob 1990, *Ph.D. Thesis.*